ABSTRACT

Title of Document: CONVECTION AND FLOW BOILING IN MICROGAPS AND POROUS FOAM COOLERS

Dae Whan Kim, Doctor of Philosophy, 2007

Directed By: Professor Avram Bar-Cohen
Professor Bongtae Han
Department of Mechanical Engineering

An open and foam-filled microgap cooler, providing direct liquid cooling for a simulated electronic/photonic component and which eliminates the problematic thermal resistance of the commonly-used thermal interface material (TIM), is examined. The single phase heat transfer and pressure drop results of water are used to validate a detailed numerical model and, together with the convective FC-72 data, establish a baseline for microgap cooler performance. The two-phase heat transfer characteristics of FC-72 are examined at various microgap dimensions, heat fluxes, and mass fluxes and the results are projected onto a flow regime map. Infrared (IR) thermography is used to explore the two-phase characteristic of FC-72 inside the channel instantaneously. Also the single and two-phase heat transfer and pressure drop of porous metal foam which can enhance the cooling capability of low conductive fluid are studied and compared with the performance of the open channel microgap cooler in terms of volumetric heat transfer rate and required pumping power.

The single-phase experimental results were in good agreement (within 10% error) with classical correlation of single-phase heat transfer coefficient and pressure drop in micro single gap channel with heat transfer coefficients as high as 23 kW/m^2-K at 260 μm gap with water and 5 kW/m^2-K at 110 μm gap with FC-72. Annular flow was found to dominate the two-phase behavior in the open channel yielding FC-72 heat transfer coefficients as high as 10 kW/m^2-K at 110 μm gap channel.

The single-phase pressure drop and heat transfer coefficient experimental results are compared with existing correlations and achieved 10 kW/m^2-K of heat transfer coefficient at 95% porosity and 20PPI with water and 2.85 kW/m^2-K with FC-72 at the same configuration. For the two-phase flow boiling, it is found that large pore size provides better cooling capability.

CONVECTION AND FLOW BOILING IN MICROGAPS AND POROUS FOAM COOLERS

By

Dae Whan Kim

Dissertation submitted to the Faculty of the Graduate School of the
University of Maryland, College Park, in partial fulfillment
of the requirements for the degree of
Doctor of Philosophy
2007

Advisory Committee:
Professor Avram Bar-Cohen, Chair
Professor Bongtae Han, Co-Chair
Associate Professor Jungho Kim
Assistant Professor Bao Yang
Professor Mario Dagenais

Dedication

To my wife, So Young Ra

and my daughters, Hajung Kim

and Hayoon Kim

Acknowledgements

I would like to thank my advisor, Professor Avram Bar-Cohen for helpful advices, and encouragements for the research work**.** He gave me the greatest opportunity to begin my Ph.D. study in thermal management of electronic device. I would like to gratefully acknowledge my co-advisor Professor Bongtae Han for significant supports, helpful advices and encouragement for the research work during the study. Without their assistances for guiding the research directions, this dissertation could not be accomplished. I would like to thank my committee members, Professor Jungho Kim, Professor Bao Yang and Professor Mario Dagenais for good comments and advice. I also like to thank Dr. Serguei Dissiatoun for his assistance in the research work. I thank Kyoung Joon Kim, Peng Wang, Raj Bahadur, Chris Bachmann, Jeff Khan, Viatcheslav Litvinovitch, Emil Rahim, Josh Gess and Juan Cevallos for their friendship during the Ph.D study.

I really want to thank my wife, So Young Ra and my daughters, Hajung Kim and Hayoon Kim for their continuous support, understanding and trust. I would like to thank my mom, Shin Soon Kang, my parents in law, Ja Young Yoon, Byung Jik Ra, my brother, Seong Wook Kim, my sister, Soo Kyoung Kim, my brother in law, Bo Sun Hong and my sister in law, Mi Kyoung Jang for their sincere support and encouragement.

I also thank to Samsung electronics for support during the Ph. D. study.

Table of Contents

List of Tables

List of Figures

Chapter 1

Introduction

The emergence of high intensity LEDs (Light Emitting Diodes) in the 1990's transformed the LEDs with white light and monochromatic colors into a fascinating light source. This evolution was possible due to improvements in the LED package design and changes in the materials used.

The simple indicator LED uses an epoxy dome lens as illustrated in Figure 1.1. The luminous efficacy of this type is limited to 0.15 lm/W. The high intensity LED packaging is illustrated in Figure 1.2. Two significant advancements were made in the high intensity LED packaging design; they were a new lens system and a metal slug. First the epoxy dome lens, which can cause bond wire breakage due to the high coefficient of thermal expansion at the glass transition temperature, was changed to a plastic lens, and the gap between the LED die and the plastic lens was filled with a silicone encapsulant. This new lens system enhanced the light extraction efficiency significantly. Secondly a metal slug was directly attached to the LED to provide very low thermal resistance. From this evolution, the thermal resistance of the LED package was dramatically reduced from more than 200 K/W to 13 K/W [1].

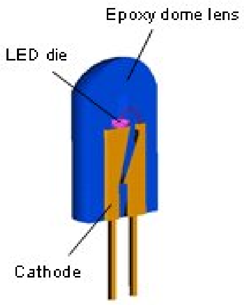

Figure 1.1 Conventional 5 mm LED package

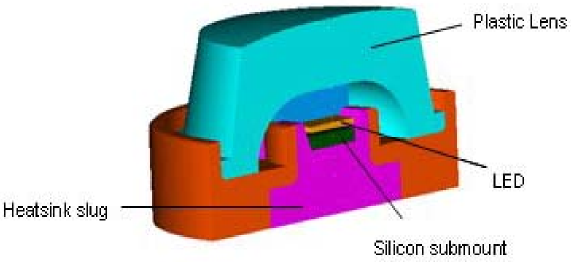

Figure 1.2 High power LED package

Table 1.1 Luminous efficacy and power efficiency of diverse light source [2]

Lamp Type	Luminous efficacy* (lm/W)	Power efficiency** (%)
Incandescent	12.6~17.5	1.9~2.6
Fluorescent	45~60	6.6~8.5
Halogen	16~25	2.3~3.6
Xenon arc lamp	50~55	7.3~8
UHP lamp	58~65	7.5~9
High brightness LED	55~60	10

[*] The luminous efficacy of optical radiation is luminous flux per optical unit power

[**] The power efficiency is optical output power per input electrical unit power.

Table 1.1 summarizes the luminous efficacy and power efficiency of diverse light source [2]. Higher efficiency and thus stable long term reliability compared to conventional light sources is evident. In addition, LEDs have numerous other advantages [3]:

- It operates at a low supply voltage and has instant on-off (i.e., no warm-up wait),
- It offers higher luminous efficacy,
- It produces sharper and more vibrant colors,
- It offers longer life time and a compact size,
- It does not contain UV or heat in the light beam.

The longer life time of an LED is probably the greatest advantage of high power LEDs. The Luxeon emitter has fallen only by 10% in efficiency after 9000 hours of stress time while the life time of a typical incandescent bulb is less than 2000 hours [1]. In addition to the advantages listed above, an LED light source consisting of red, green and blue LEDs can provide full high definition color gamut (up to 140% of NTSC gamut as shown in Figure 1.3 where the green triangle is the NTSC gamut and the yellow polygon is the color gamut of LED). Since the color wheel or filter is no longer needed, the LED light source is emerging in its application to digital display devices such as projection and LCD backlit screens.

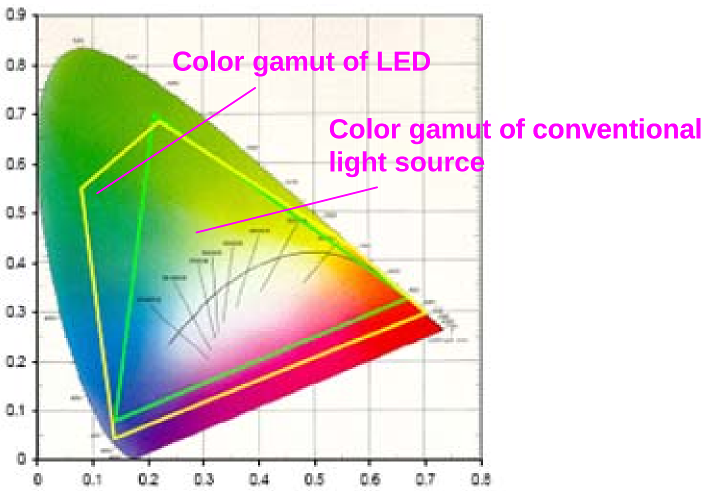

Figure 1.3 Color gamut comparison [4]

Table 1.2 summarizes the widely used light sources and the amount of power needed to replace them with LEDs. Considering that the input power which the current high power LED package can handle is only 5W, it is clear from the table that the current single LED cannot replace the existing light sources due to the high input power to generate required optical output. The size of an LED chip can be increased to produce the required optical power for a highly light demanding system [5]. Besides the cost, however, controlling the light output poses some difficulty.

Table 1.2 Light sources and the amount of power needed to replace these sources with LED [6]

Light source	Application	Input power (W)	Efficacy (lm/W)	Flux (lm)	LED power			
					Current @ 40 lm/W		Near future @ 100 lm/W	
					Input (W)	85% Loss* (W)	Input (W)	70% Loss (W)
60W GLS	Home	60	12	720	18	15.3	7.2	5
100W GLS	Home	100	12	1200	30	25.5	12	8.4
11W CFL-1	Home	11	65	720	18	15.3	7.2	5
50W Halogen	Shop	50	18	900	22.5	19.1	9	6.3
90W Halogen	Shop	90	18	1620	40	34	16.2	11.3
58W TL	Office	58	90	5220	130.5	110.5	52.2	36.5

*Loss of the input power which is converted to heat not to light.

The optical output of an LED can be increased with a higher input power but this poses two interrelated problems; higher current density and elevated junction temperature. The current density increases with input power. If the current density of an LED exceeds the optimized current density (around 50 A/cm^2) [1], the luminous output per watt is decreased due to the electro-migration effect. Subsequently, the loss of luminous output is converted to heat, resulting in an elevated junction temperature [6].

The light output decreases dramatically as the junction temperature increases. The optical output of AlInGaP LEDs, which produce a series of red color, exponentially decreases as the junction temperature is elevated. The optical output of red color can decrease as much as 80% when the junction temperature is elevated to 100°C [7]. The optical output of InGaN LEDs which produce the range of blue and green color decreases linearly with the junction temperature. The optical output of blue and green color LEDs decreases by 10% and 40%, respectively, with the same level of junction temperature elevation [7].

The elevation of the junction temperature also shortens the lifetime of LEDs. Jacob [8] examined the junction temperature effect on the lifetime. He measured the optical output degradation at different junction temperatures. As the junction temperature decreased, the lifetime of the LEDs increased from 10,000 to 20,000 hours [8].

In summary, the junction temperature elevation will result in decreased luminosity, wavelength shifting, reduced life span and even failure of LED package. For these reasons, a single LED cannot produce the optical flux required for the highly light demanding system such as a projection system. Therefore, it is important to consider an array of LEDs for such a light demanding system. Even though an LED is a very efficient light source, the power efficiency is only 10%, which means 90% of input power is dissipated as heat. With that in view, thermal characteristics should be examined, and precise prediction of the junction temperature is required before employing high power LEDs into a highly light demanding system.

Chapter 2

Thermal Issue of LEDs

2.1 Thermal Resistance of Single LED package

A high power single LED package and the corresponding thermal resistance network are shown in Figure 2.1. An LED chip is mounted on a submount and the submount is directly mounted on a heat slug. The LED subassembly is mounted on a metal-core printed circuit board (MCPCB), which provides a path for the input power. An optional heat sink can be attached to the bottom of the MCPCB for thermal management. A plastic lens collects the output light and the gap between the lens and the chip is filled with a silicone encapsulant to enhance the light extraction efficiency.

The thermal resistance of the high power LEDs can be divided in three parts: thermal resistances of (1) junction to heat slug ($R_{j\text{-}s}$), (2) slug to board ($R_{s\text{-}b}$), and (3) board to air ($R_{b\text{-}a}$).

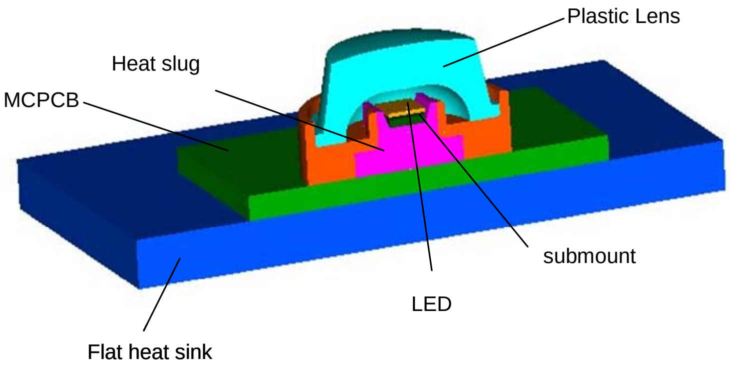

(a) Schematic diagram of high power LED

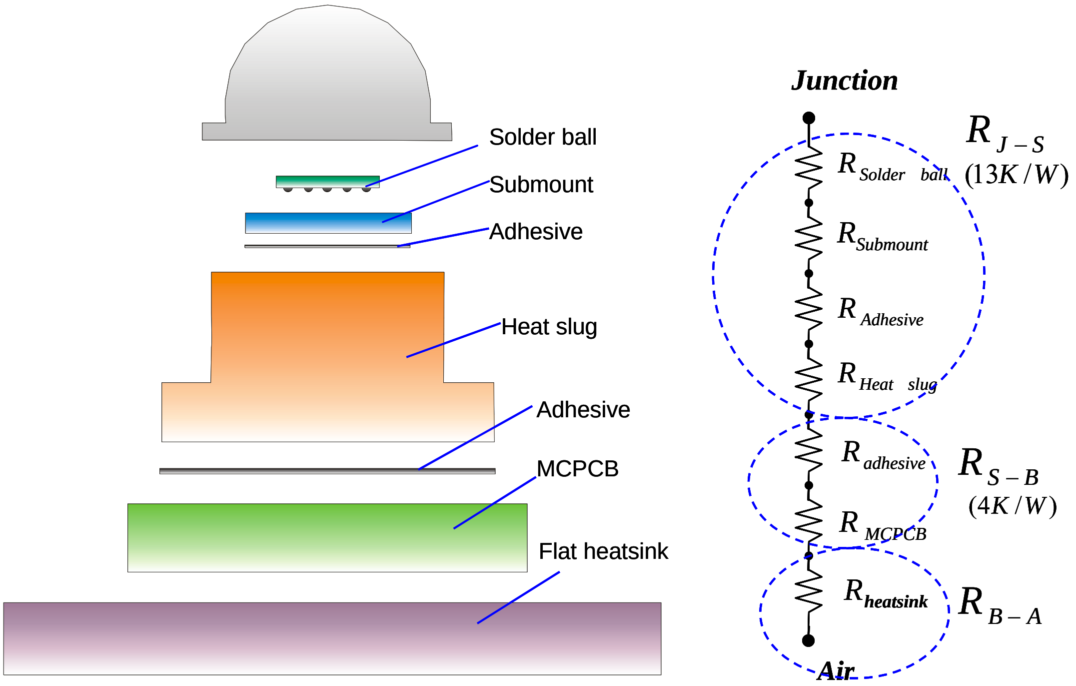

(b) Thermal resistance network of high power LED

Figure 2.1 Thermal resistance and schematic diagram of high power LED package [9]

Heat generated from the LED die goes through the junction to the solder ball, which connects the LED die to the submount, the thermally conductive adhesive, and the heat slug. The thermal resistance of junction to heat slug can be expressed as

$$R_{J-S} = R_{die} + R_{solderball} + R_{submount} + R_{adhesive} + R_{heatslug} \tag{2.1}$$

The thermal resistance of heat slug to board and board to environment can be further decomposed as

$$R_{S-B} = R_{adhesive} + R_{MCPCB} (= R_{dielectric\ layer} + R_{Al\ layer}) \tag{2.2}$$

$$R_{B-A} = R_{tape} + R_{convection} \tag{2.3}$$

The thermal resistance of junction to heat slug of a typical LED package (e.g., Lumileds Luxeon III LED) is 13 K/W [10]. The dimensions of the LED package and material properties are listed in Table 2.1. A thermal analysis was performed using a commercial FEA tool, ANSYS Ver. 10.0. The steady state heat conduction equation with heat generation is employed as the governing equation to calculate the temperature field in the 3-D FEA model.

$$\frac{\partial}{\partial x}\left(k\frac{\partial T}{\partial x}\right)+\frac{\partial}{\partial y}\left(k\frac{\partial T}{\partial y}\right)+\frac{\partial}{\partial z}\left(k\frac{\partial T}{\partial z}\right)+q=0 \qquad (2.4)$$

where T , k and q are the temperature, the thermal conductivity and the heat generation rate, respectively.

The thermal path LED die through the silicone filling and the plastic lens was ignored due to their relatively high thermal resistance. The heat slug was molded by polymer. Considering the low thermal conductivity of a polymer used for the mold and its small surface area, the heat loss through the heat slug to the ambient was also ignored. Therefore, it was assumed that the convective heat transfer occurred only at the bottom of the heat slug and a representative result is shown in Figure 2.2.

Table 2.1 Material Properties of LED package

	Thermal conductivity (W/m-k)	Thickness (mm)
Solder	50	0.1
Submount (Si)	150	0.5
Adhesive (Submount-heat slug)	1	0.035
Heatslug (Cu)	360	2.87
Adhesive (Heat slug-MCPCB)	1	0.07
MCPCB		
Dielectric Layer	1.8	0.1
Metal layer (Al)	237	1.5
Tape	0.067	0.130
Heat sink (Al)	237	1.6

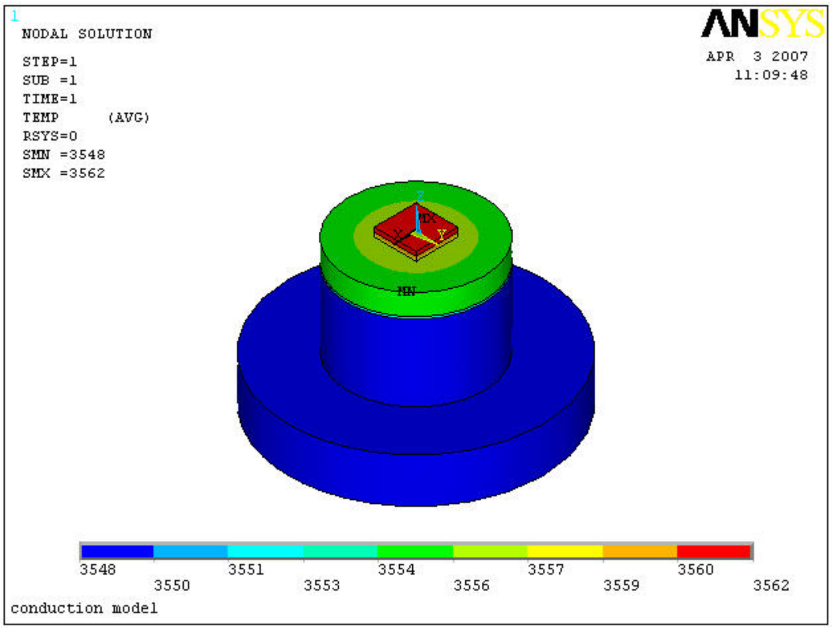

Figure 2.2 FEA thermal analysis result of Luxeon III LED package of Lumileds

2.2 Thermal solutions for LED package

The preliminary thermal analysis indicated that the main barrier of thermal pass of the LED package is the Thermal Interface Materials (TIM). The TIM should be improved to enhance the performance of the LED package. Liquid cooling solutions can be considered to handle the extremely high flux. Figure 2.3 shows the scheme of a liquid cooled LED package, and Table 2.2 shows the heat transfer coefficient which is available in the literature. The FEA modeling scheme described in the previous section (Luxeon III LED, Lumileds) was used to simulate the effect of the TIM and liquid cooling solutions.

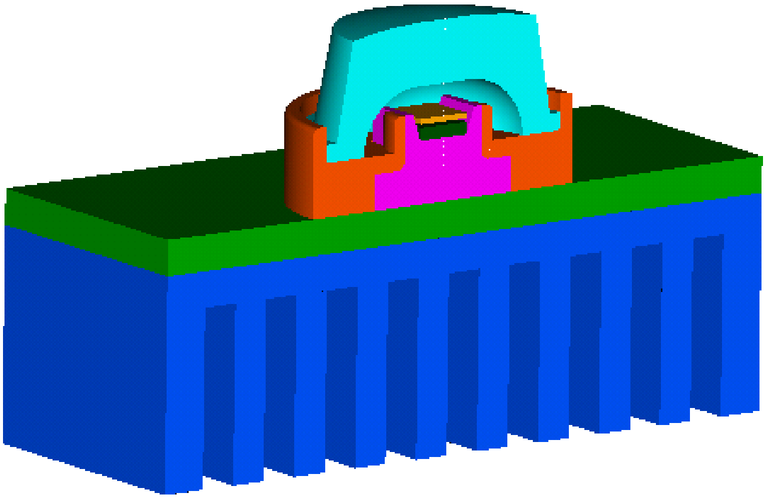

Figure 2.3 Schematic diagram of liquid cooled LED package

Table 2.2 Heat transfer coefficient of liquid cooled channel

Hydraulic diameter (μm)	Flow rate (l/min)	Heat flux (W/cm^2)	Quality	Thermal Resistance	Heat transfer coefficient (W/m^2-K)
318	4.5	45.0	-	0.89	20000 [11]
67.2	0.31	62.7	-	0.82	32598 [12]
248.95	0.000432	62.6	0.25	0.73	40000 [13]
207	0.000407	11.9	0.2	0.49	60000 [14]
207	0.000407	21.5	0.1	0.36	80000 [14]
207	0.000172	54.0	0.09	0.293	100000 [14]

The enhanced thermal resistance network is illustrated in Figure 2.4.a, where a dotted circle indicates the enhanced part of thermal resistance. The thermal resistance of R_{B-A} is decreased by a liquid cooled channel and was decreased further by a two-phase cooling scheme. The resultant convection resistance as a function of the increased heat transfer coefficient is shown in Figure 2.4 (b).

The effect of the heat transfer coefficient on the junction temperature was evaluated and the results are shown in Figure 2.5. The junction temperature exceeds the maximum allowable junction temperature when the input power is 5 W or larger, and the junction temperature remains nearly the same regardless of the value of the heat transfer coefficient. The effect of the heat transfer coefficient on the junction temperature is negligible due to the high thermal resistance of the TIM. Therefore, the current package can handle only up to 3 W or 4 W even when a liquid cooling scheme is employed.

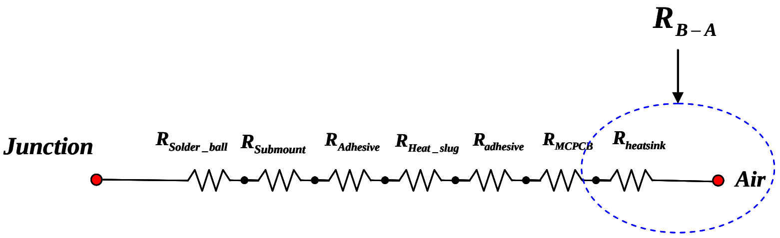

(a) Enhanced thermal resistance

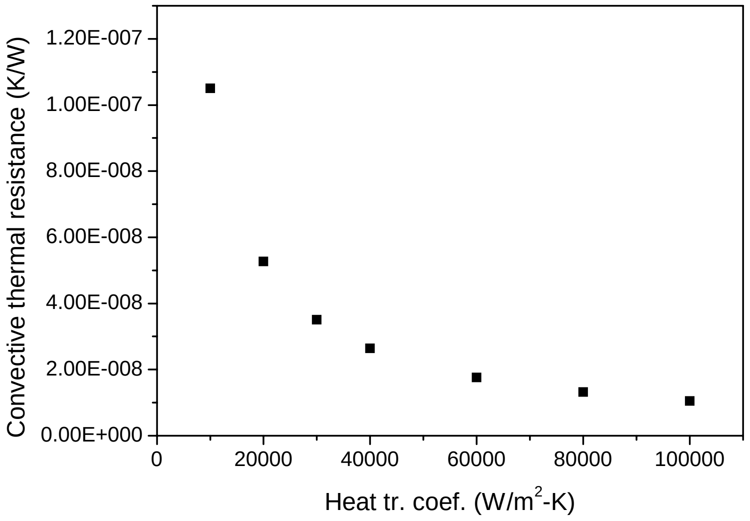

(b) Convective thermal resistance vs. heat transfer coefficient.

Figure 2.4 Thermal resistance vs. heat transfer coefficient

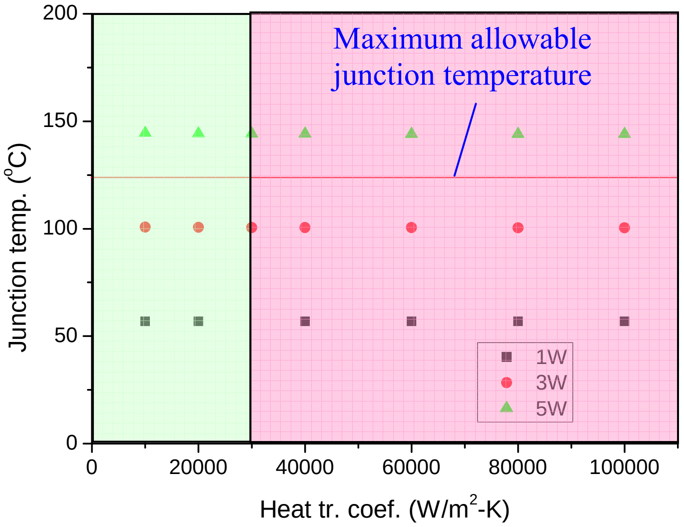

Figure 2.5 Junction temperature vs. Heat transfer coefficient of Lumileds Luxeon III LED

In order to take advantage of advanced cooling solutions, the thermal performance of the TIM should be improved. In their recently released LED (LUXEON® K2, Lumileds), the adhesive between submount and heat slug was replaced with AuSn 80/20 solder (thermal conductivity of 57 W/m-K) and the thermal resistance was reduced to 9 K/W [15]. This improvement in the thermal resistance network is illustrated in Figure 2.6 (a) (blue dotted circle) and the corresponding junction temperature vs. heat transfer coefficient is shown in Fig. 2.6 (b).

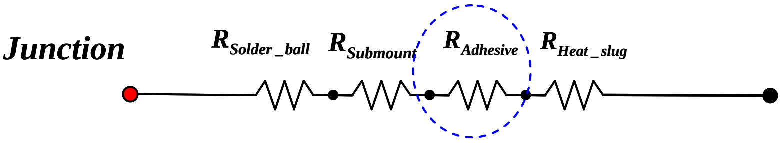

(a) Enhanced thermal resistance part of Luxeon K2 [15]

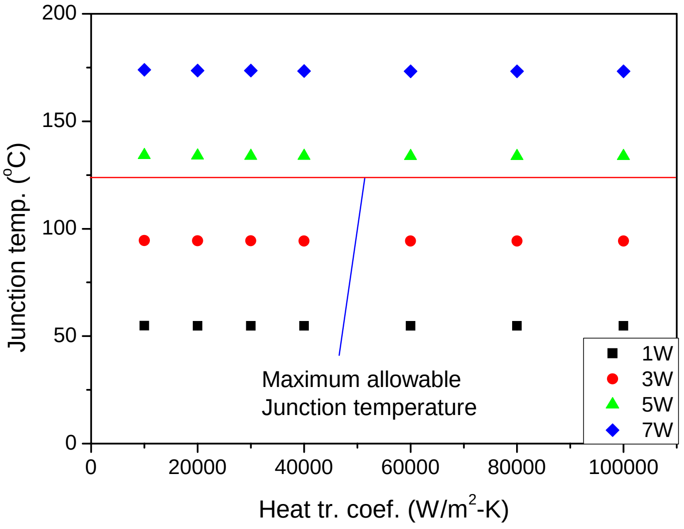

(b) Junction temperature vs. Heat transfer coefficient

Figure 2.6 Water cooled Luxeon K2 LED package

This improvement enhanced thermal performance but the effect was not substantial. The junction temperature is reduced only by 7%, and again it remains virtually unchanged regardless of the high heat transfer coefficient. This improvement is not sufficient to meet the demand for an optical output to replace the conventional light sources of high power applications such as a projection system.

It has been reported that more than 20 LEDs are needed to produce the required optical output of each color of a projection system [16] ~ [18]. For the projection system, it is desirable to place each LED as closely as possible to obtain a pin-like source. However, the thermal resistance of the current package configuration is simply too large to accommodate the array of LEDs.

One possible solution for the array scheme is to replace the TIM materials with materials with extremely high thermal conductivity. Using a TIM material of 45 W/m-K (Diemat, DM6030 HK) [19], an LEDs array (3 x 2 with 0.15 mm gap) was analyzed. The thermal enhancement in the network and the numerical results are shown in Figure 2.7.

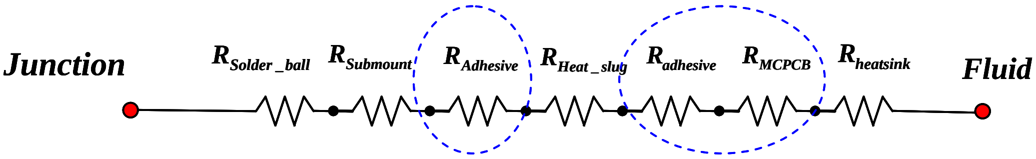

(a) Enhanced thermal resistance due to change of TIMs to highly conductive thermal epoxy.

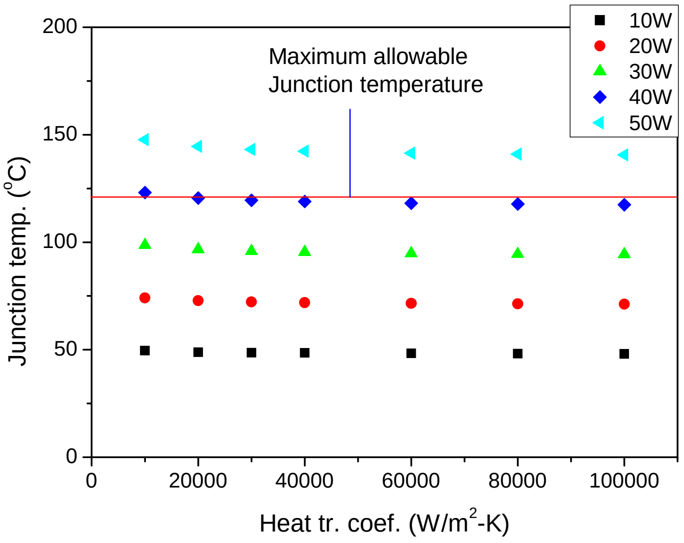

(b) Junction temperature vs. heat transfer coefficient

Figure 2.7 Water cooled Luxeon K2 LED array with highly conductive TIM

Although the results of Figure 2.7 are promising, the use of thin thermal adhesives is not desirable for high power LEDs due to mechanical reliability. Thermal stresses induced by the CTE mismatch between the adjacent materials can cause delamination at the interfaces and thus produce hot spots.

The challenging but more attractive solution will be *direct* submount cooling using micro-gap coolers. This concept is illustrated schematically in Figure 2.8. With this scheme, the LED array is mounted directly on the micro gap and thus the TIM is completely removed. The metal core printed circuit board (MCPCB) can be placed under the submount of the LED package with a groove to attach the submount and a hole to attach the micro gap coolers as shown in Figure 2.8 (a). Figure 2.8 (b) is the section diagram of this schematic. LED package is attached to the groove of the MCPCB and the electrical input can be provided through wire bonding between the submount and the MCPCB. Then the microgap cooler is directly attached to the submount. This scheme can potentially reduce the thermal resistance to less than 6 K/W.

Figure 2.9 shows the results of the direct submount cooling. The FEA results suggest that single-phase cooling with water (with heat transfer coefficient as high as 30 kW/m^2-K) could provide adequate thermal management for a 3 mm x 2 mm, 6 device LED array dissipating 40 W. This scheme requires neither TIM nor micromachining of the substrate, and can be a very attractive cooling scheme for high power imaging devices.

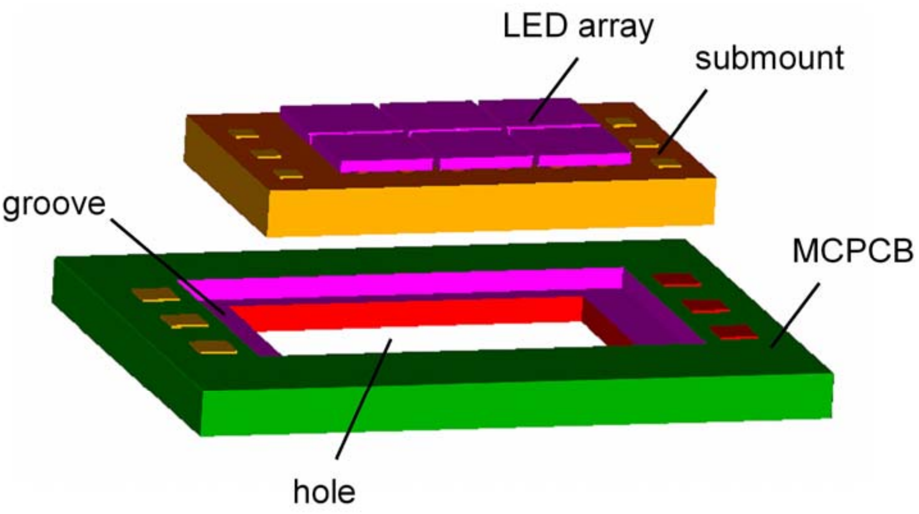
LED array
submount
groove
MCPCB
hole

(a)

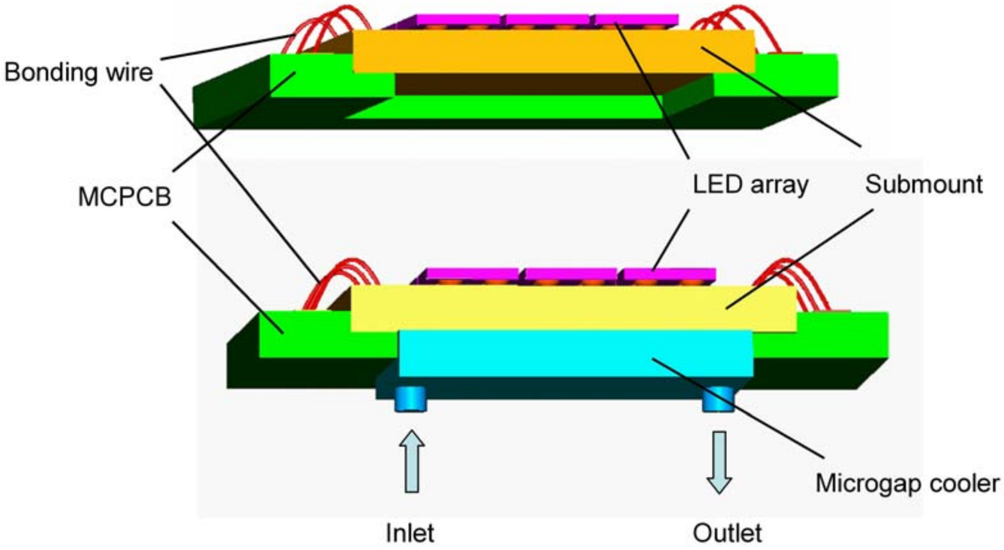
Bonding wire
MCPCB
LED array
Submount
Microgap cooler
Inlet
Outlet

(b)

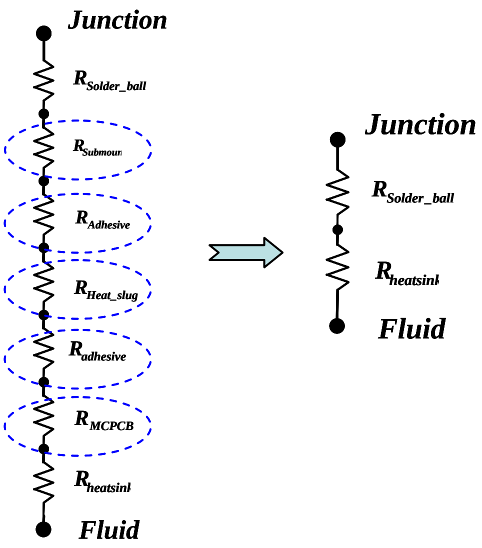

(c)

Figure 2.8 (a) schematic diagram of direct submount cooling, section diagram of this scheme and (c) change of the thermal resistance network

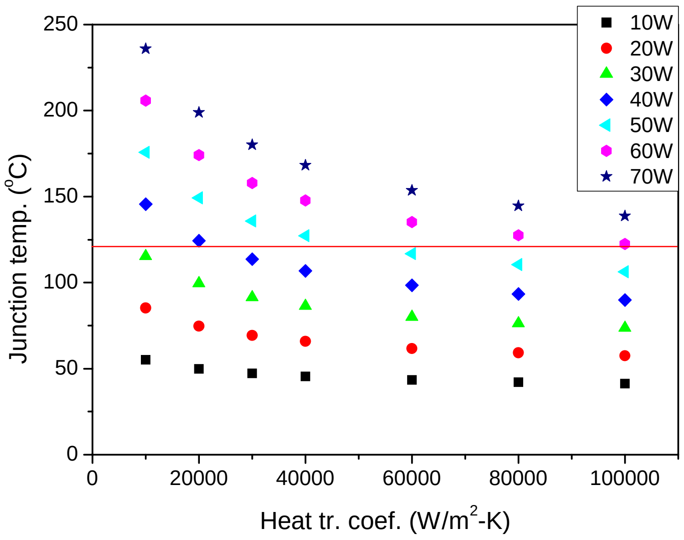

Figure 2.9 Schematic diagram of direct submount cooling

Chapter 3

Experimental set-up and Error analysis

3.1 Experimental set-up and apparatus

The purpose of the experiment is to investigate the hydraulic and thermal performance of a single gap channel as a liquid cooled heat exchanger. The overview of the experimental set-up and the photo of the actual apparatus are shown in Figure 3.1 (a) and (b), respectively. In the setup, a coolant is supplied to a test “clamshell” channel by a pump. The flow rate is measured by a flow meter and a desired rate is set by a regulating valve which connects the pump and the meter. A chiller cools the coolant exiting from the outlet of the test channel and supplies the cooled coolant to the pump. The temperature of the channel is measured by thermocouples attached to the channel, and the pressure drop is measured by a pressure transducer that is connected to the inlet and outlet of the channel. The pressure drop and the temperature are recorded through a data acquisition system at a preset sampling rate.

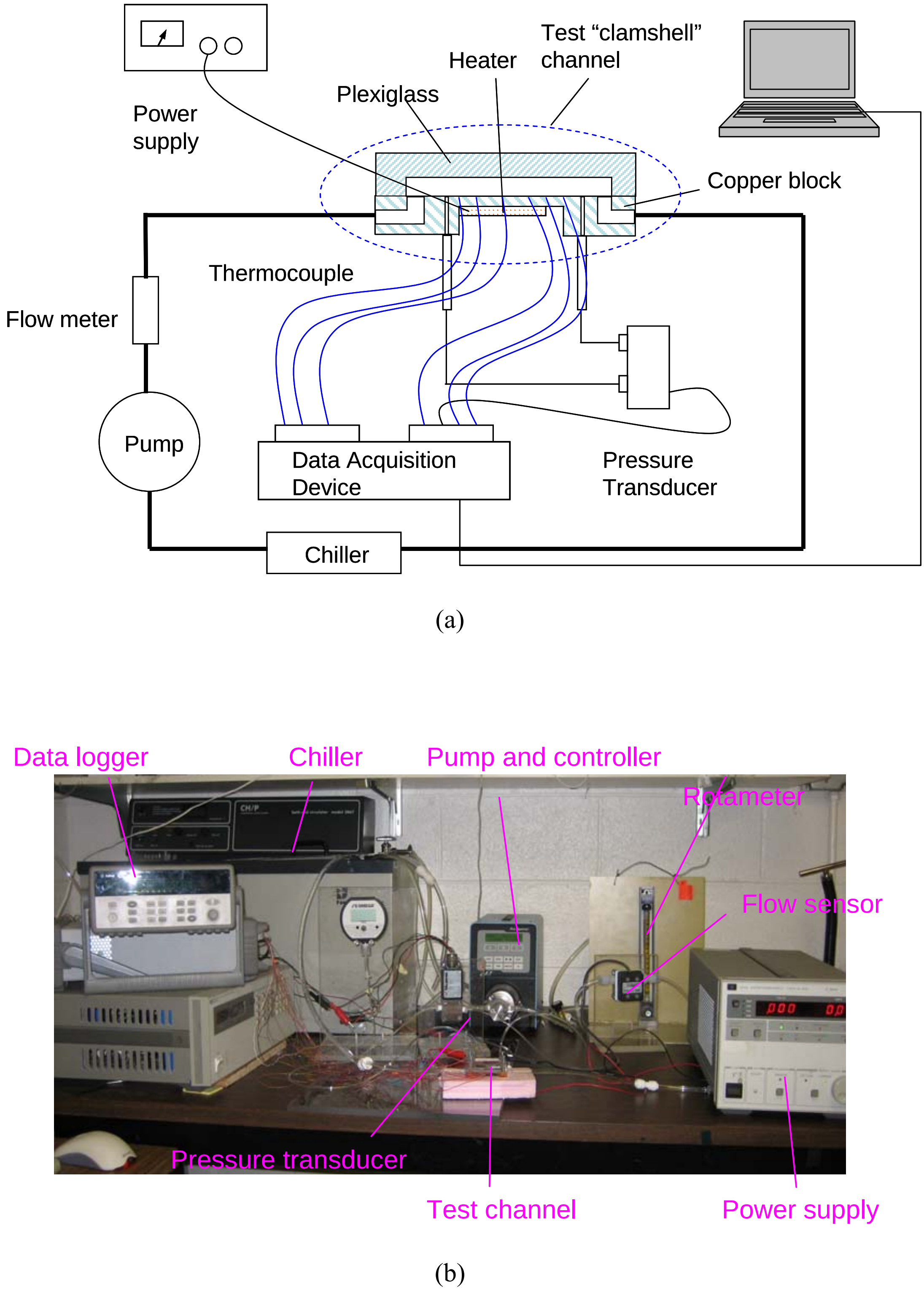

Figure 3.1 Experimental set-up (a) schematic diagram (b) picture of experimental apparatus

The test "clamshell" channel is illustrated schematically in Figure 3.2 (a). The base plate was made of copper and the top plate was made of Plexiglas for flow visualization during the experiment. The center of the top plate was machined differently to produce various channel gaps as illustrated in Figure 3.2 (b).

Two single-gap channels with two different dimensions were fabricated; 31 mm x 34 mm and 10 mm x 37 mm (Figure 3.2 (c) and (d)). The gap of the third channel (Figure 3.2 (c)) was filled with open cell metal foam. The photographs of these three configurations are shown in Figure 3.2 (b), (c), and (d), respectively. During the experiments, the channel was placed within a Styrofoam box (160 mm x 250 mm x 90 mm). The thickness of the foam was 20 mm and it insulated the channel effectively during experiments.

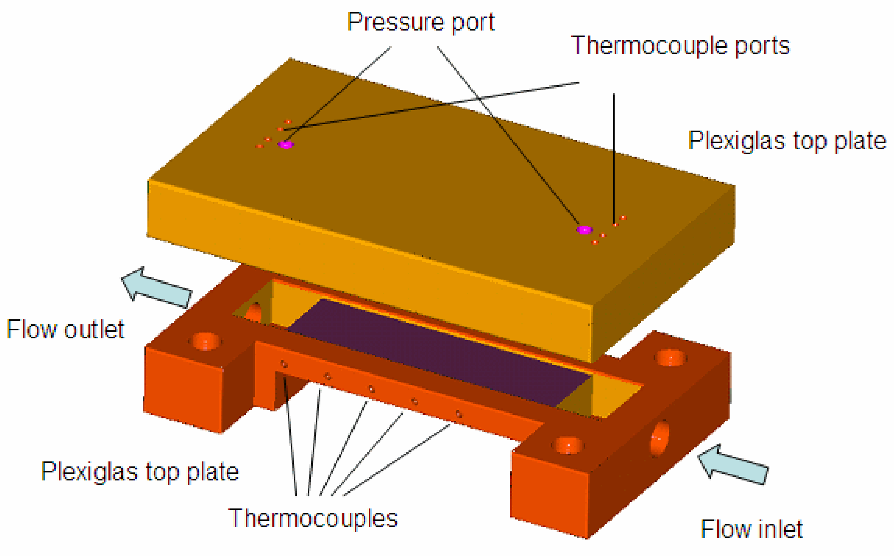

(a)

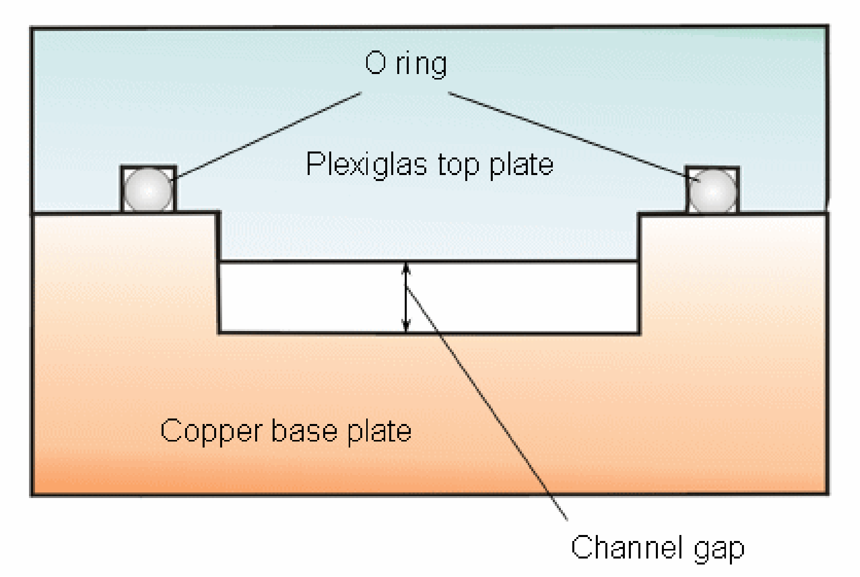
O ring
Plexiglas top plate
Copper base plate
Channel gap

(b)

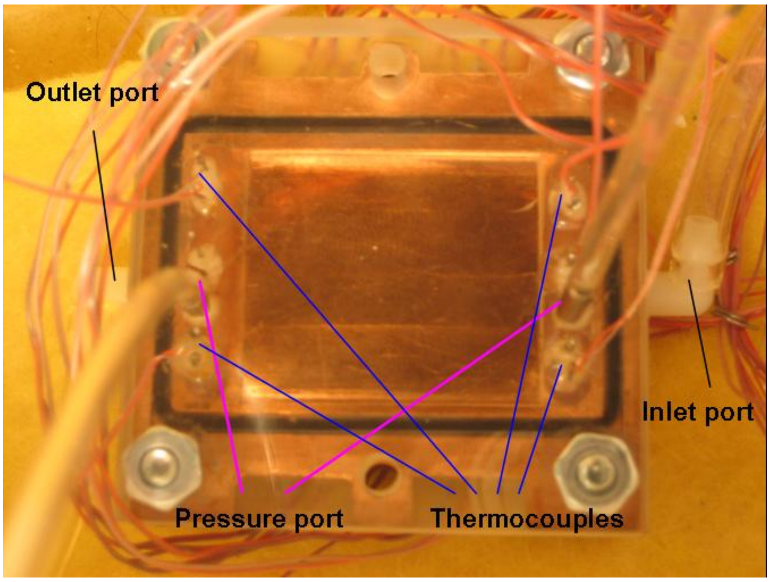
Outlet port
Inlet port
Pressure port
Thermocouples

(c)

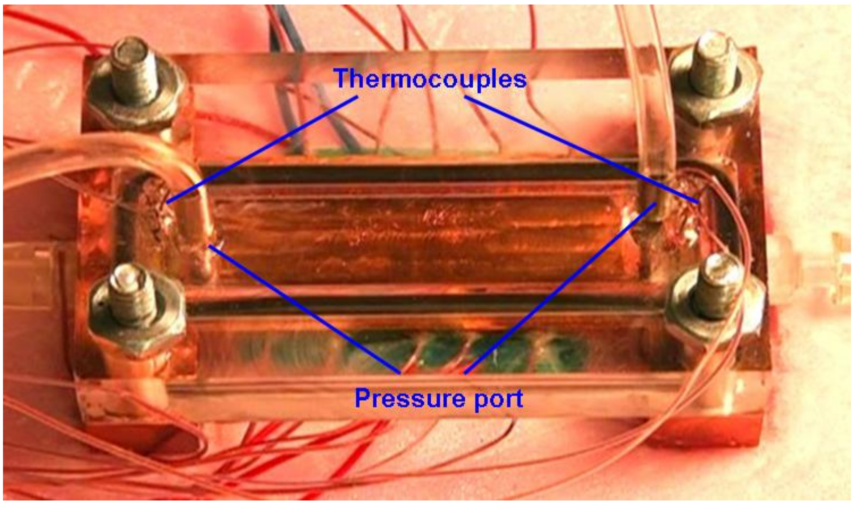

(d)

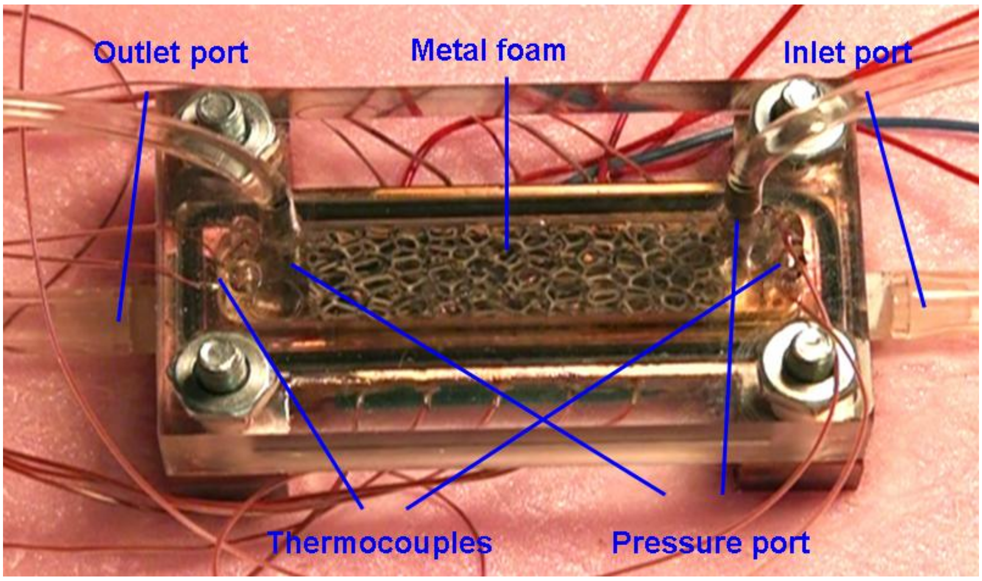

(e)

Figure 3.2 (a) Schematic diagram of channel, (b) Section diagram of single gap channel, picture of (c) wide (31 mm x 34 mm) channel, (d) narrow (10 mm x 37 mm) channel and (e) open cell metal foam channel

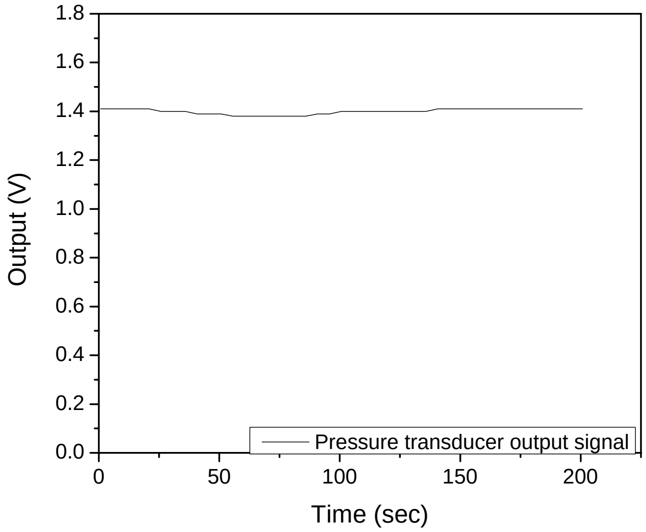

(a)

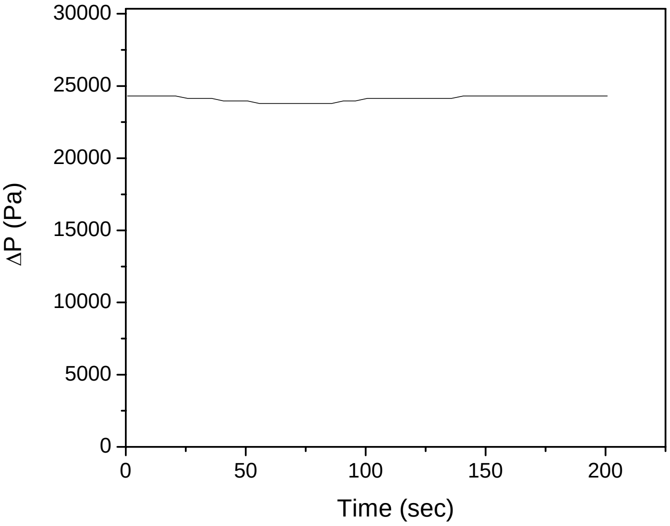

(b)

Figure 3.3 (a) Output of pressure transducer and (b) corresponding pressure drop

The coolant was pumped by a commercial pump (200 GB, Micropump) which has a capability of the maximum 3200 ml/min at 5000 rpm. The flow rate was controlled by a regulating valve (Pro-spense, Cole-Parmer), which can control the flow rate within ± 0.5% of accuracy. The flow rate was measured by two different flow meters. The low flow rate (up to 200 ml/min) was measured by a liquid flow sensor (FPR1502, Omega), which provides ± 3% full scale (FS) accuracy and 0.2% FS repeatability. Flow rates greater 200 ml/min were measured by a rotameter (FL-3840ST, Omega), which offers ± 2% FS accuracy and 0.25% FS repeatability.

Two pressure ports (1/16" diameter) were bored into the top plate to measure the pressure drop across the channel. The static pressure drop of the fluid was measured by two different differential pressure transducers manufactured by Valydine; Model P55D-32 for the low pressure ranging from 0 to 3.2 psi and Model P55D-40 is used for higher pressure drops up to 12 psi. Both models offer an accuracy of ± 0.25% FS. The output of the pressure transducer is a DC signal (± 5V in FS) and was documented by a data logger (34970A, Agilent). The representative output of the pressure transducer and the corresponding pressure drop are shown in Fig. 3.3. The results show that the variation of the output signal is less than 3%.

The temperature of the coolant was controlled by a chiller (CH/P 2067, Forma Scientific). The chiller could remove up to 600W from the coolant, and thus regulate the inlet temperature within 0.3°C in the range of 50°C.

The temperature of the test block was measured by a series of thermocouples as shown in Fig. 3.4. First 10 holes (1mm in diameter) were bored from both sides of the walls (5 holes in each side) through the center of the channel, just 1 mm below the wetted surface, and E-type thermocouples (diameter of 75 μm) were placed in the holes. In addition, four additional thermocouples were inserted through the thermocouple ports in the top plate (Fig. 3.2a) to measure the temperature of the coolant at both the inlet and the outlet. The inlet temperature of the coolant was maintained at 25 ± 0.2°C.

A conventional polyimide coated heater (HK5574, Minco) was used originally to heat the copper base plate. Two heaters were attached to the bottom of the wide channel copper base plate (31 mm x 34 mm) and each of them provided the maximum heat flux of 11.8 W/cm^2.

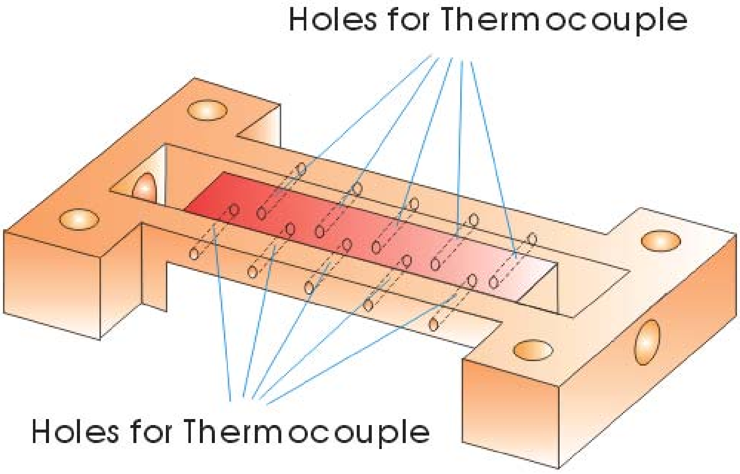

Figure 3.4 Thermocouples to measure the wall temperature

Although available, the conversion efficiency of higher flux heaters (as high as 105.3 W/cm^2) was extremely low due to the high contact resistance created by the coating and they were not considered for the experiments. In addition the effective length of the heater was only 6.35 mm x 6.35 mm, which was not suitable for the narrow channel (10 mm width). For these reasons, ceramic leaded chip resistors (LR

13737T0100J; American Technical Ceramics) were used for the narrow channel. The ceramic leaded chip resistor can dissipate 100% of the power under 100°C. The dimension of the resistor is 1 cm x 1 cm, and it can generate the maximum of 250 W (250 W/cm^2 of heat flux). Three resistors were soldered to the whole bottom surface of the copper base plate. The direct soldering eliminated the contact resistance and offered the required high conversion efficiency.

Considering the capacity of the power supply (6038A, Agilent), a 50 Ω resistor was selected. The maximum power of the power supply was 200 W (the maximum voltage and current were 60 V and 10 A, respectively). The equivalent resistance of three resistors was 16.67 Ω and the possible current output was 3.6 A under the maximum voltage of 60 V. Consequently the dissipated power by the resistors was 216 W and the maximum heat flux was 50 W/cm^2.

The thermocouple data were also documented by the data logger. Representative results are shown in Figure 3.5. Before the heater was turned on, the temperature was maintained at 25°C and the temperature difference among the thermocouples was less than ± 0.2°C. After the heater was turned on, the temperature of each thermocouple increased rapidly and reached the steady-state condition. At the steady-state condition, the temperature variation of each thermocouple was less than ± 0.2°C. Note that thermocouple reached slightly different steady-state temperatures due their positions relative to the center of the channel. Table 3.1 shows the list and specification of the experimental equipment.

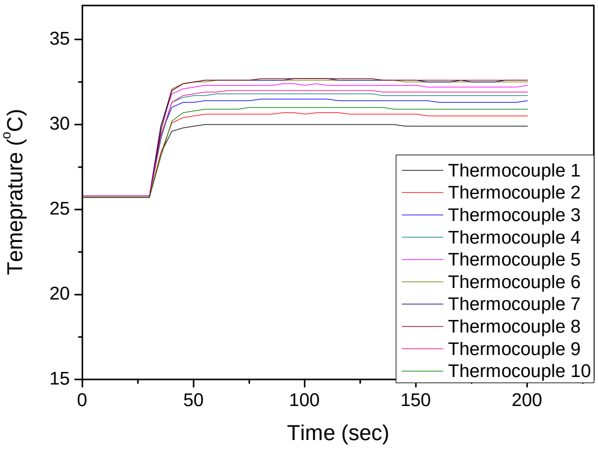

Figure 3.5 Measured data of thermocouple inside of the test block

Table 3.1 List and specification of experimental equipment

Equipment	Specification	Manufacturer	Model no.
Power supply	60V (± 0.035% error) 10A (± 0.09% error) Maximum power: 200W	Agilent	6038A
Data acquisition	20 channel	Agilent	34970A
Pump controller	control the flow rate within ± 0.5% of accuracy	Cole Parmer	Pro-spence
Pump	maximum 3200 ml/min at 5000 rpm	Micropump	200 GB
Pressure transducer	up to 3.2 psi (± 0.25% FS error) up to 12 psi (± 0.25% FS error)	Valydine	P55D-32 P55D-40
Flow meter	3% FS accuracy and 0.2% FS repeatability ± 2% FS of accuracy and 0.25% of repeatability	Omega	FPR1502 FL-3840ST

3.1.1 Fluids selection

Water is one of the most popular coolants. As a coolant, water possesses good characteristics such as high thermal conductivity, high convective heat transfer coefficient, and high heat capacity. However, it is electrically conducting (non-dielectric) and can cause device failure when it leaks out from the cooling channel. This disadvantage is too critical, and in practice electrically non-conducting dielectric liquids have been the preferred choice for electronic devices.

Among the existing dielectric liquids, Fluocarbon fluids such as FC-72, HFE-7100, FC-70 etc. manufactured by 3M are known to have superior dielectric and chemical characteristics. However, they still suffer from the disadvantages of other dielectric liquids such as low thermal conductivity (only 10% of water) and thus low convective heat transfer coefficient.

In this research water and dielectric liquid FC-72 were used as a coolant for the experiments. FC-72 was selected over the other dielectric fluids because of the high latent heat, the relatively high boiling temperature, and the low viscosity and surface tension which are critically required for the single-phase and two-phase heat transfer characteristics in micro gap channels. One unique disadvantage of the FC-72 is that FC-72 contains a high volume of air. This large quantity of air makes it hard to measure the exact physical properties. It was not difficult to degas the dissolved air but was impossible to maintain the degassed status during the measurements. For this reason, the gassy liquid was used in the experiments.

Table 3.2 Physical properties of fluid

Property	FC-72	Water
Boiling point (°C)	56	100
Density (kg/m3)	1680	997.1
Viscosity (cP)	0.64	0.89
Thermal conductivity (W/m-K)	0.057	0.61
Specific heat (J/kg-K)	1100	4179
Surface tension (dynes/cm)	12	72

3.1.2 IR (Infrared) Thermography Preparation

In this study, an IR camera was also used to investigate the wall temperature of wetted surface. For the purpose of viewing, a UV grade synthetic sapphire window fabricated by Swiss Jewel (25.4 mm in diameter and 3.2 mm in thickness) was attached to the center of the Plexiglas top plate as shown in Fig. 3.6a. An adhesive was used to attach the sapphire window and a silicone-based sealant was applied around the perimeter of sapphire to prevent the possible leakage of fluid. Figure 3.6 (b) shows the picture of the micro gap channel with the Sapphire window. A mid-wave (wavelength of 3 ~ 5 μm) science grade infrared camera (Merlin) was utilized for this study. It is worth noting that FC-72 has excellent transmissibility (over 97%) for the mid-wave infrared spectrum.

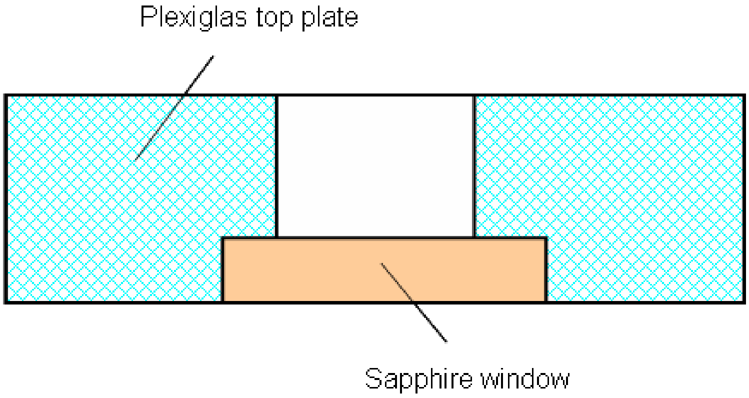

(a)

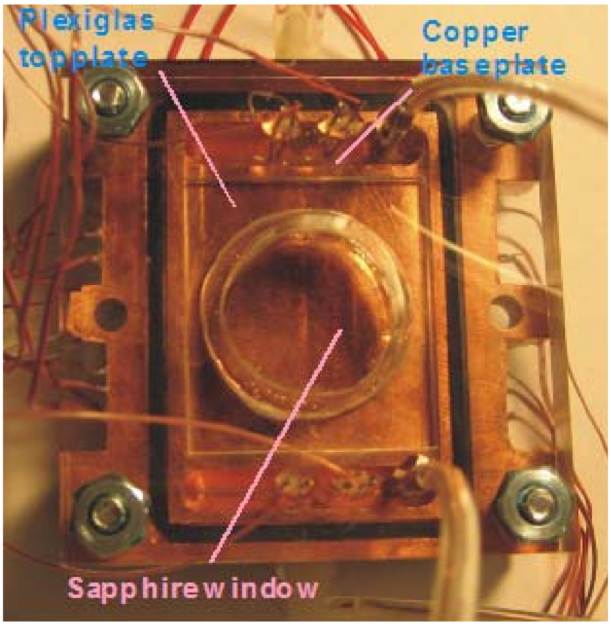

(b)

Fig. 3.6 (a) Section diagram of sapphire widow attached top plate and (b) a picture of the micro gap channel with sapphire window

Table 3.3 Specification of IR camera

Feature	Specification
Detector Type	InSb (Indium Antimonide)
Temperature measurement range	0 - 350° C standard
Spectral range	1.5 - 5.5 microns (3-5 microns set by cold filter)
accuracy	± 2° C, ± 2 % of reading
Thermal sensitivity	0.025° C (0.018° C typical)
Image frequency	60 Hz
Array format	320 x 256 (data pixel: 81920)

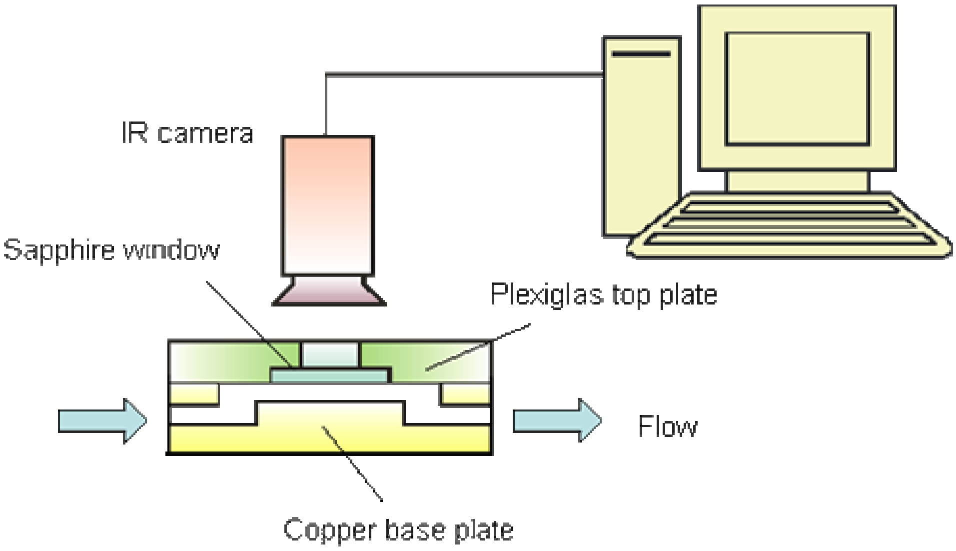

(a)

(b)

Fig 3.7 Experimental set-up of IR image analysis (a) schematic diagram and (b) photograph

3.2 Experiment procedure and Error analysis

3.2.1 Experimental procedure

First the chiller was turned on. After the temperature reached the setting temperature, the data logger was turned on and began to record the thermocouple readings that represented the temperature of the test channel. At this initial stage of the experiment, the temperature difference of thermocouples was less than 0.3°C.

Next the flow rate of pump controller was set to the desired flow rate and the pump was turned on. A small deviation of the flow rate from the desired value was controlled by the regulating valve while the flow rate was monitored by the flow meter. As the fluid went through the channel, a pressure drop was generated and was measured by the pressure transducer. The power supply was then turned on to activate the heater. The temperature of the channel was increased gradually and eventually reached steady state. The recorded temperature data was used to calculate the heat transfer coefficient and energy balance.

Each micro gap cooler was tested under the same conditions at least three times. After each experiment, the apparatus was given several minutes to return to the initial status, prior to commencing the next experiment.

Table 3.4 The parametric matrix of wide (31 mm x 34 mm) channel

Channel gap	Fluid	Maximum flow rate of single-phase	Maximum mass flux of two-phase
600 μm	water	9.5 ml/s	-
	FC-72	10.6 ml/s	-
260 μm	water	9.5 ml/s	-
	FC-72	10.6 ml/s	105.1 kg/m^2-s
120 μm	FC-72	7.25 ml/s	105.1 kg/m^2-s

Table 3.5 The parametric matrix of narrow (10 mm x 37 mm) channel

Channel gap	Fluid	Maximum flow rate of single-phase	Maximum mass flux of two-phase
500 µm	water	9.5 ml/s	-
	FC-72	9.5 ml/s	280 kg/m^2-s
210 µm	water	8.3 ml/s	-
	FC-72	8.3 ml/s	666.7 kg/m^2-s
110 µm	FC-72	3.0 ml/s	1273 kg/m^2-s

Tables 3.4 and 3.5 summarize the test matrix for the two channels, respectively. Each channel was tested with 3 different gaps with single-phase water and single and two-phase FC-72. The maximum mass flux was decided by the maximum heater rating.

3.2.2 Error Analysis

The measurement error can be divided into bias errors and precision errors [20]. The bias error remains constant during the measurements under a fixed operating condition. The bias error can be estimated by calibration, concomitant methodology, inter-laboratory comparison and experience. When measurements are repeated under fixed operating conditions, the precision error is affected by the repeatability and resolution of equipments, the temporal and spatial variation of variables, the variations in measured variables, and variations in operating and environmental conditions in measurement processes.

Each measurement error would be combined with other errors in some manner, which increases the uncertainty of the measurement. A first-order estimate of the uncertainty in the measurement due to the individual errors can be computed by the root-sum-square method as [20]

$$u = \sqrt{e_1^2 + e_2^2 + \cdots + e_k^2} \tag{3.1}$$

where u is the uncertainty in measurement and e is the elemental error of equipment.

The uncertainty in the single-phase heat transfer coefficient, obtained from the energy balance equation (Eq. 4.6), is linear and is affected by the uncertainties in the measured quantities including the flow rate, the temperature of the copper block, the temperature of inlet and outlet, the stability of data logger and power supply. It can be expressed mathematically as

$$\frac{\delta h}{h} = \sqrt{\left(\frac{\delta Q}{Q}\right)^2_{flow\ rate} + \left(\frac{\delta Q}{Q}\right)^2_{read\ out} + \left(\frac{\delta q}{q}\right)^2 + \left(\frac{\delta \Delta T_{wall}}{\Delta T_{wall}}\right)^2 + \left(\frac{\delta\left(T_{outlet} - T_{inlet}\right)}{T_{outlet} - T_{inlet}}\right)^2} \tag{3.2}$$

where δh is uncertainty of heat transfer coefficient, $(\delta Q)_{flow\ rate}$ is error of flow rate which is caused by error of pump controller, $(\delta Q)_{read\ out}$ is the read out error of rotameter, δq is error of input power, $\delta \Delta T_{wall}$ is the measurement error of wall excess temperature and $\delta\left(T_{outlet} - T_{inlet}\right)$ is the measurement error of temperature difference of inlet and outlet. The errors of the pump controller, the rotameter and the read out error of the rotameter are estimated to be ± 0.5%, ± 3% and 5%, respectively. The error of the power supply is 0.1%, the maximum error of wall excess temperature measurement is ± 0.5°C which causes maximum error of 2% and the error of $T_{outlet} - T_{inlet}$ is assumed as 8%, because an error of 0.1°C in the $\left(T_{outlet} - T_{inlet}\right)$

difference changes 8% the dissipated heat from the energy balance in Eq. (4.6). Thus, the possible maximum error of measuring the heat transfer coefficient is 10.1%, obtained from Eq. (3.2). Figure 3.8 shows the measured heat transfer coefficient of 600 µm gap wide (31 mm x 34 mm) channel for water with 10% error bar. Most of the measured data is within 10% of the prediction.

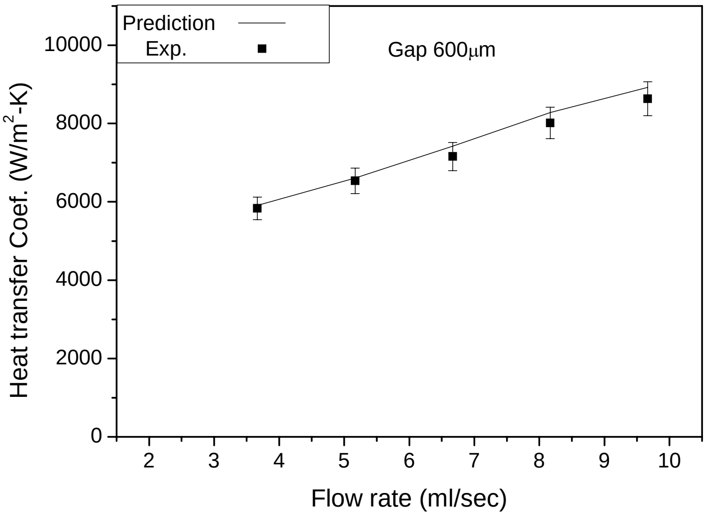

Figure 3.8 Measured heat transfer coefficient of 600 µm gap wide (31 mm x 34 mm) channel with water

The uncertainty in the measured pressure drop is determined by the accuracy of the pressure transducer (± 0.25% FS). However, the uncertainty in the measurement of flow rate is a combination of the visual and data logger errors. Therefore the resulting uncertainty of measuring pressure drop can be expressed as

$$\frac{\delta \Delta p}{\Delta p} = \sqrt{\left(\frac{\delta Q}{Q}\right)^2_{flow\ rate} + \left(\frac{\delta Q}{Q}\right)^2_{read\ out} + \left(\frac{\delta \Delta p}{\Delta p}\right)^2_t} \tag{3.3}$$

where, Δp is pressure drop and $\delta\Delta p$ is the uncertainty of pressure drop measurement and $(\delta\Delta p)_t$ is error of the pressure transducer.

The error of pressure transducer is ± 0.25% FS, the measurement error of data logger of dcV is 0.05% and the error related to measurement flow rate are ± 3% of rotameter and 5% error of read out error. Therefore, the possible maximum error of pressure drop measurement is 6.5%.

Figure 3.9 shows the measurement result of pressure drop of water from the 10 mm x 37 mm channel with a 500 µm gap. The average standard deviation of the experimental results is less than 7% of the predicted value by Eq. (4.1) and Eq. (4.2) and the variation of different experiments is within 7%. These experimental results are close to the calculation and are within expected uncertainty.

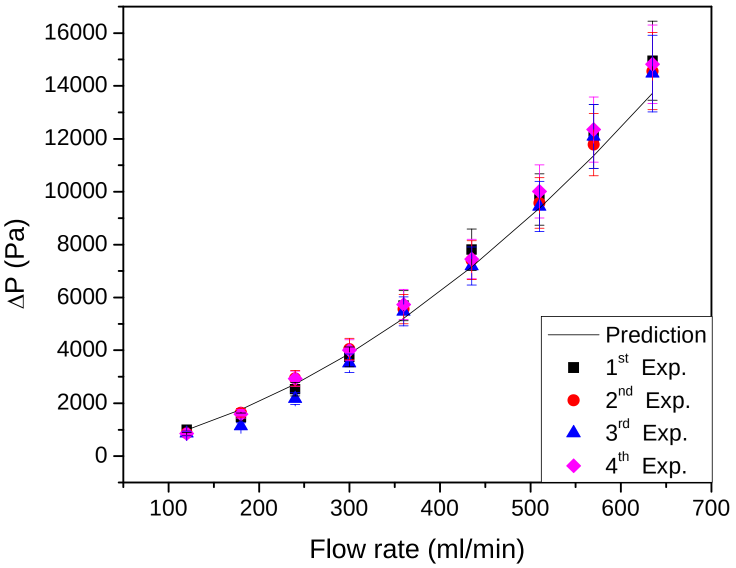

Figure 3.9 Pressure drop measurement result and repeatability of 500 µm gap narrow (10 mm x 37 mm) channel with water

As shown in Figure 3.9, the pressure drop measurement results are within the error of the experiment and are in good agreement with the predicted value. Therefore, the exact channel gap can be determined from the measured data.

For the two-phase experiment, flow sensor which has ± 2% error was used for the measurement of flow rate instead of rotameter. Therefore, the error of rotameter read out is removed, the uncertainty related to the equipments is reduced than single-phase experiment. However, due to the complexity of two-phase behavior, the repeatability of two-phase experiment was around 5 ~ 10% as shown in chapter 5 and chapter 6.

Chapter 4

Micro-gap Channel - Theoretical Background and Preliminary Experiments

A single microgap channel is a promising thermal management solution for high heat flux electronic devices because it requires no attachment (no TIM between heat source and cooling solution) and no micromachining. In order to figure out the capability of a single microgap channel, the hydrodynamic and thermal characteristic are studied and preliminary experiments are performed and compared with theoretical prediction. For the experiment, water and a dielectric liquid, Fluorinert FC-72 from 3M, were used as the working fluids. Since the physical properties of water are well known, in order to confirm the experimental set-up, the theoretical prediction was compared with the experiment result for water. The dimension of the channel for these preliminary experiments was 31 mm wide x 34 mm long and the channel gap was 600 μm, 260 μm and 120 μm, respectively.

4.1 Pressure Drop

4.1.1 Theoritical Prediction

The amount of work required to pump the coolant through a channel is a critical parameter for the design of liquid cooled micro-channel and micro-gap coolers. As the laminar flow pressure drop of a parallel plate channel has been studied by numerous researchers, it can be predicted very accurately. In general, the flow through a channel enters from the upstream plenum and is discharged through a down stream plenum. Kays and London [21] correlated the overall pressure drop in a parallel plate channel in dimensional form and it is expressed as

$$\Delta P = \frac{\rho V^2}{2}\left[\left\{\left(1-\sigma_c^2\right)+K_c\right\}+4\cdot f\frac{L}{D_h}-\left\{\left(1-\sigma_e^2\right)+K_e\right\}\right] \tag{4.1}$$

Where, $\rho V^2/2$ is the dynamic pressure associated with flow in the channel, $\sigma_c = A_c / A_{in}$ and $\sigma_e = A_c / A_{out}$ are area ratios associated with contraction and expansion of the flow at the channel entrance and exit. K_c and K_e are loss coefficients associated with the flow irreversibilities, and f is friction factor which accounts for losses resulting from friction in the channel. For hydrodynamically developing laminar flow, Shah and London [22] correlated the friction factor in a parallel plate channel in the form of

$$f = \left[\frac{3.44}{\left(x^+\right)^{1/2}} + \frac{24+\dfrac{0.674}{4\cdot x^+}-\dfrac{3.44}{\left(x^+\right)^{1/2}}}{1+0.000029\cdot\left(x^+\right)^{-2}}\right]/\mathrm{Re} \tag{4.2}$$

where x^+ is dimensionless hydrodynamic axial distance which can be expressed by

$$x^+ = \frac{x/D_h}{\mathrm{Re}} \tag{4.3}$$

In the fully-developed limit, i.e. for $x^+ >> 0.1$, the friction factor asymptotically approaches 96/Re.

4.1.2 Experimental Results for Water and FC-72

The goal of the single phase experiments with water was to measure the hydraulic and thermal performance of the single micro-gap cooler and compare the results with existing theory and correlations. This comparison could serve to establish the accuracy and reproducibility of the experimental data attained with this apparatus, validate the use of a computational fluid dynamics software product, and set the stage for later two-phase experiments. The comparison of the values predicted by Eq. (4.1) and the measured pressure drops for various flow rates of water and FC-72 through a 34 mm long channel, with a 600 μm and 260 μm gap, is plotted in Figure 4.1 (a) and (b). The maximum Reynolds number in the data shown was 1218 for FC-72 and 458 for water, indicating laminar flow in the channels. The hydrodynamic axial distance, x^+ and channel Reynolds number of water at 600 μm gap was 0.13 and 207 at a flow rate of 3.67 ml/s and 0.05 and 546.57 at a flow rate of 9.67 ml/s. The equivalent values for water at 260 μm gap was 0.3 and 210 at a flow rate of 3.67 ml/s and 0.11 and 552.9 at a flow rate of 9.67 ml/s. The x^+ and channel Reynolds number of FC-72 at 600 μm gap was 0.06 and 332.3 at a flow rate of 2 ml/s and 0.01 and 552.9 at a flow rate of 9.67 ml/s. The values for FC-72 at 260 μm gap were 0.13 and 503.8 at a flow rate of 3 ml/s and 0.03 and 1776.8 at a flow rate of 10.6 ml/s, suggesting that fully-developed flow is only attained in the lower flow rates in the larger channels, while the majority of the data was in developing flow. As anticipated, pressure drops for the 600μm gap are seen to increase monotonically with the flow rate and to range from 150 Pa to 870 Pa for water and 100 Pa to 930 Pa for FC-72. For the 260 μm gap, the values range from 550 Pa to 5.4 kPa for water and 540 Pa to 9.2 kPa for FC-72. The measured values of the pressure drop for the flow of water and FC-72 in the 600 μm and 260 μm channels were attained at channel Reynolds numbers of up to 458 for water and up to 1218 for FC-72, respectively.

The error bar of 5% and 7% are drawn for 600 µm and 260 µm gap channels and most of the data is within this range. In the case of the 600 µm gap channel, all the experimental results are within 5% of the theoretical prediction. For the 260 µm gap channel, several measured point at low flow rate are out of the 7% error bound, but the other measured results come very close to the predicted values. From Figure 4.1, it can be concluded that the deviation of the experimental results is less than 10% of the predicted value. Interestingly, despite the lower viscosity of the FC-72 and due to the compensating effect of the higher liquid density, as compared to water, the pressure drops for the two fluids in these microgap channels are nearly equal.

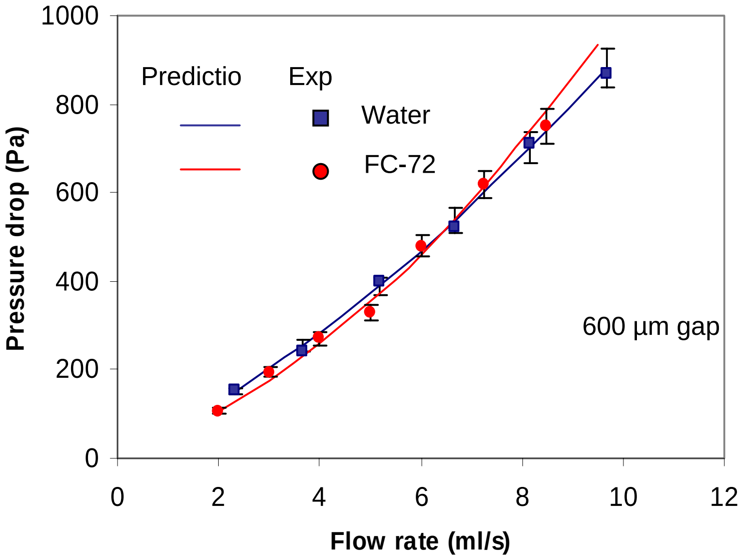

(a)

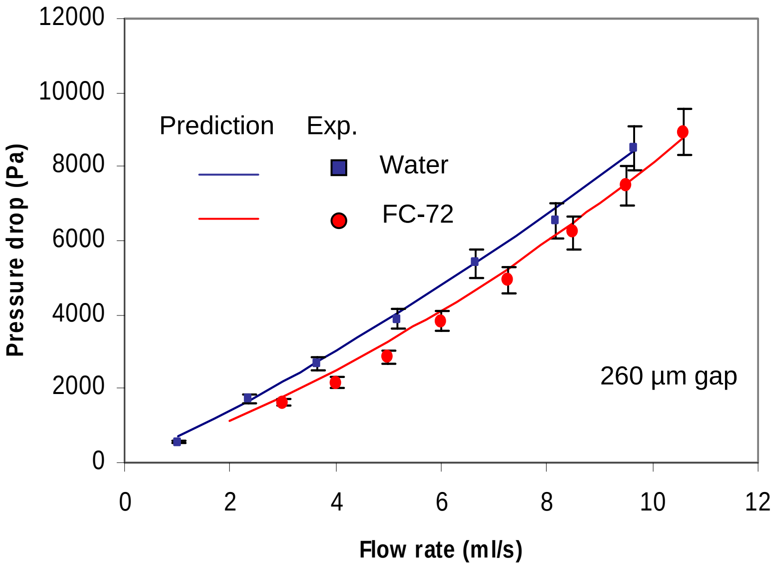

(b)

Figure 4.1 Pressure drop for single-phase water and FC-72 flow in microgap channels: (a) 600 µm gap, (b) 260 µm gap

4.2 Numerical Modeling

A three-dimensional numerical model was developed with a commercial Computational Fluid Dynamics software product, IcePak ver. 4.1, to obtain the wall temperature, heat transfer coefficient, and heat flux. The CFD model included the Styrofoam enclosure and the number of elements was 1,040k. For the evaluation of single-phase heat transfer results, the wall temperature and energy balance were compared with measured data. The average deviation of the measured temperature between experiment and numerical modeling is less than 0.7°C. For the two-phase situation, in order to determine the net heat transfer rate into the channel, simulations were performed with a pseudo fluid which had very high specific heat and high thermal conductivity to mimic the properties of a boiling liquid. The properties of the pseudo fluid were changed until the wall temperature from the CFD modeling matched the measured temperatures. The wall superheats and “inversely” computed wall heat fluxes were then used to determine the heat transfer coefficients.

4.3 Single-Phase Heat Transfer

4.3.1 Theoritical Background

The thermal performance of a micro gap cooler is evaluated with the dimensionless Nusslet number as given by

$$Nu = \frac{hD_h}{k} \tag{4.4}$$

where k is the thermal conductivity of the liquid, D_h is the hydraulic diameter, and h is the heat transfer coefficient. The heat transfer coefficient is defined as

$$h = \frac{q}{A\Delta T} \tag{4.5}$$

where ΔT is the temperature difference between the heated surface (copper block) and coolant and q is heat transfer rate to the coolant. The heat transfer rate can be determined from an energy balance on the channel, i.e.

$$q = \dot{m}C_p\left(T_{outlet} - T_{inlet}\right) \tag{4.6}$$

where $\dot{m}$ is the mass flow rate of the coolant.

From the above equations, the empirical Nusselt number can be calculated by the following expression, using the experimental data.

$$Nu = \frac{\dot{m}C_p(T_{outlet} - T_{inlet})}{A\Delta T}\frac{D_h}{k} \tag{4.7}$$

In their classic textbook, Kays and Crawford [23] discuss many of the available Nu equations for uniform surface temperature and uniform surface heat flux boundary conditions, applied to circular tubes, circular tube annuli, and rectangular tubes and covering the laminar flow of fluids of various Prandtl number for both fully-developed and thermally-developing flow. Therefore, single-phase, laminar flow heat transfer can be predicted very well in most cases. Mercer et al. [24], performed experiments with a 12.7 mm (0.5") high parallel plate, copper channel with air flow and correlated their experiment data in terms of the thermally-developing length x*. The local and mean heat transfer coefficients for isoflux, asymmetrically-heated, parallel plate channels can be predicted with Eq. (4.8) and Eq. (4.10) [22] - [24].

$$Nu_x = \left[\frac{1}{6} - \sum_{n=1}^{\infty} \frac{\exp\left(-4n^2\pi^2 x^*\right)}{n^2\pi^2}\right]^{-1} \tag{4.8}$$

$$Nu_m = \left[\frac{1}{6} - \sum_{n=1}^{\infty} \frac{1-\exp\left(-4n^2\pi^2 x^*\right)}{n^2\pi^2}\right]^{-1} \tag{4.9}$$

where dimensionless thermal axial distance x* is defined as

$$x^* = \frac{x/D_h}{\mathrm{Re}\,\mathrm{Pr}} \tag{4.10}$$

Even though single-phase heat transfer characteristic can be predicted accurately by the existing correlation, most of the available heat transfer data was obtained with the flow of gas and water in micro-scale channels. Little has been done to generate data with other liquids, especially new types of coolants which are aimed at the cooling of modern electronic devices. Recently, Xie et al. [25], reported their experimental result for microchannels with the flow of FC-72. With a 0°C coolant inlet temperature, they achieved a 3.8 kW/m^2-K heat transfer coefficient at a 6.67 ml/s FC-

72 flow rate in a channel 300 µm wide x 900 µm high and 55 mm length. At a lower flow rate of 4.44 ml/s they found a 1.58 kW/m^2-K heat transfer coefficient with a channel 300 µm wide x 2.1 mm height with 55 mm length. Nineteen different channels were used in these experiments.

4.3.2 Experimental Results for Water

The average heat transfer coefficients predicted by Eq. (4.9), the values obtained from the Computational Fluid Dynamics software IcePak ver. 4.1, and the measured average heat transfer coefficient for the 600 µm and 260 µm gap, at various liquid flow rates, are shown in Figure 4.2. A heat flux of 5.7 W/cm^2 was transferred to the channel and the average wall temperature was 32 ± 3˚C, varying somewhat with the channel gap and flow rate.

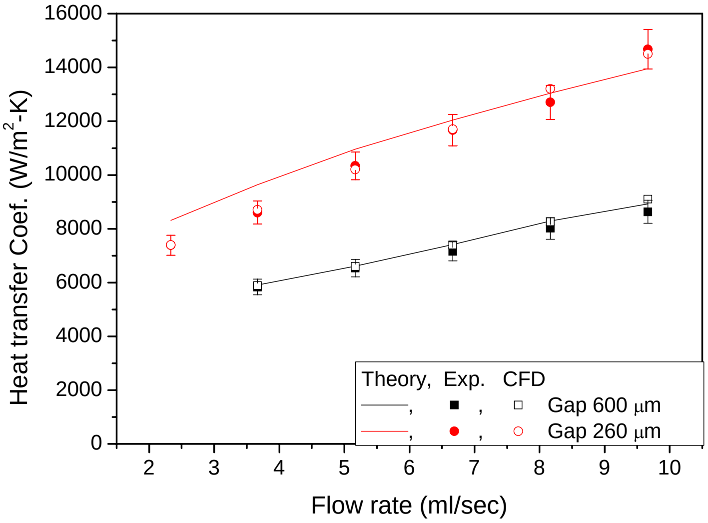

Figure 4.2 Average heat transfer coefficient for single phase flow of water in microgap channels

As anticipated, the heat transfer coefficients are seen to rise monotonically with the flow rate. At the highest flow rate of 9.7 ml/s, the peak measured heat transfer coefficient for water flowing in the 600 μm gap cooler is seen to reach 8.5 kW/m^2-K and 15 kW/m^2-K for the case of the 260 μm gap. The 5% error bars are drawn for each point. For the 600 μm gap channel, all of the experimental results fall into within 5% of the predicted value. For the 260 μm gap channel, the error between experiment and prediction was greater than 5% at less than 5 ml/s of flow rate. However, the experimental results are closer to the predicted value as the flow rate increases beyond 5 ml/s. The CFD result of ICePak ver. 4.1 is also shown in the Figure 4.2. Since the CFD results are nearly identical with the experimental result, the model can be used for the prediction of different configurations of this channel.

4.3.3 Experimental Results for FC-72

The results obtained for the single-phase flow of FC-72 in 3 distinct microgap channels are shown in Fig 4.3 for an applied heat flux of 4.3 W/cm^2. The highest average heat transfer coefficients measured were 1.2 kW/m^2-K for a channel gap of 600 μm, 2.8k W/m^2-K for a channel gap of 260 μm, both at a liquid flow rate of 10.5 ml/s, and 3.1 kW/m^2-K for the 120 μm gap, at a flow rate of 7.2 ml/s. As expected from the previously presented theoretical relations, the microgap heat transfer coefficients increase with flow rate and vary inversely with the channel gap, and are approximately just 10% of those obtained for water, due to the low thermal conductivity and specific heat of FC-72. Once again there is nearly perfect agreement between the CFD results and the values obtained from the classical theoretical predictions, but the agreement between theory and data is inferior to that achieved with water, with a standard deviation of 15 % for 600 µm, 8% for 260 µm, and 6% for 120 µm. In Figure 4.3, 10%, 15% and 20% error bars are drawn for the 600 µm, 260 µm and 120 µm gap channel results, respectively. It may also be seen that for unexplained reasons, the slope of the experimental heat transfer coefficient data for the 260µm channel is considerably steeper than suggested by theory or observed in the other two channels.

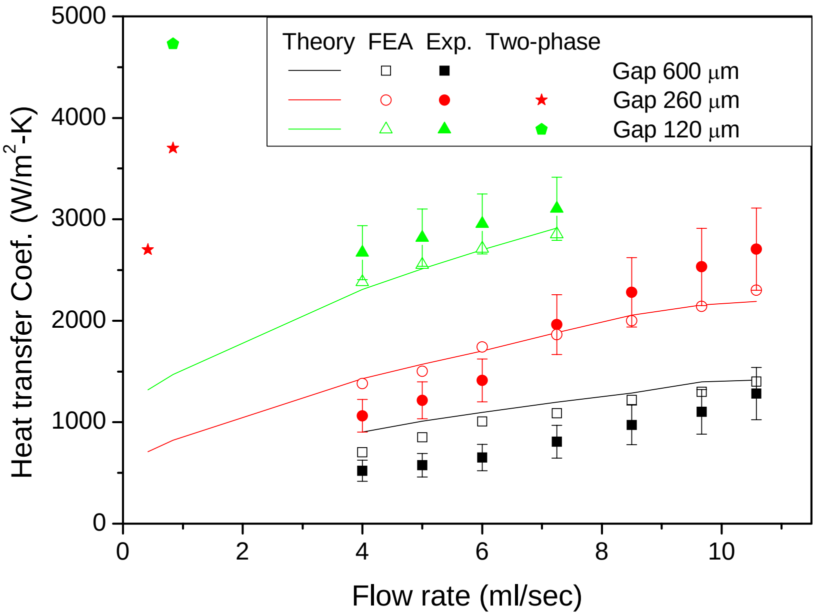

Figure 4.3 Average Heat transfer coefficients for FC-72 flowing in three microgap channels

It is believed that a significant part of the observed discrepancy between the measured and predicted values is associated with the presence of a high concentration of dissolved gas in the FC-72 (48 ml gas/ 100ml liquid for 1atm, gas-saturated FC-72, [26]**)** and some possible inaccuracies in fluid properties. For very low single-phase liquid inlet volumetric flow rates (less than 1ml/s), two-phase flow was observed to occur and the measured heat transfer coefficients are seen, in Figure 4.3, to be 3-5 times higher than the single-phase predicted values for the appropriate channel gap and flow rate. The highest measured heat transfer coefficient, at 4700 W/m^2-K, is also seen to exceed the highest single phase measured value by approximately 50%.

As noted above, due to the large amount of dissolved gas in FC-72, bubbles were observed before the wall temperature reached the saturation or boiling point temperature and may be responsible for the observed enhancement of the heat transfer capability of FC-72. The dissolved gas effect is shown more clearly in Figure 4.5.

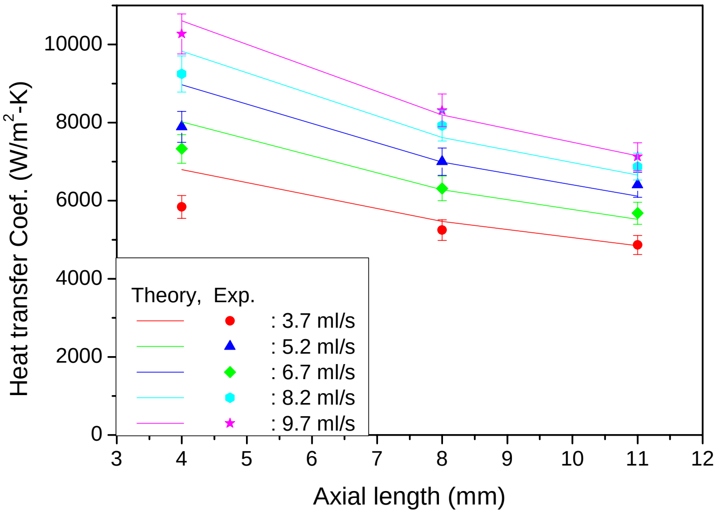

Figure 4.4 Local heat transfer coefficients for water flowing in a 600 µm gap channel

The development of the thermal boundary layer in the inlet regions of microgap channels can be expected to reduce the local heat transfer coefficient in the axial direction, as shown in the theoretical predictions plotted in Figures 4.4 and 4.5 for various flow rates of water and FC-72. Comparing Figs 4.4 and 4.5**,** it is also observed that the axial variation of the local heat transfer coefficient in the channel for FC-72 differs from that of water and the classical solutions. For the case of water, the local heat transfer coefficient decreases – as expected - with the axial distance and the experimental result is within a 5% error bar, but in the FC-72 data obtained in this study, the local heat transfer coefficients – especially for the small gap channels and the lower flow rates - are seen to increase with the axial distance. The experiments with FC-72 were repeated 3 times for each case and, as shown in Figure 4.6, these repeated results are nearly identical, reflecting less than 5% variation, in the presence of a 10% experimental uncertainty.

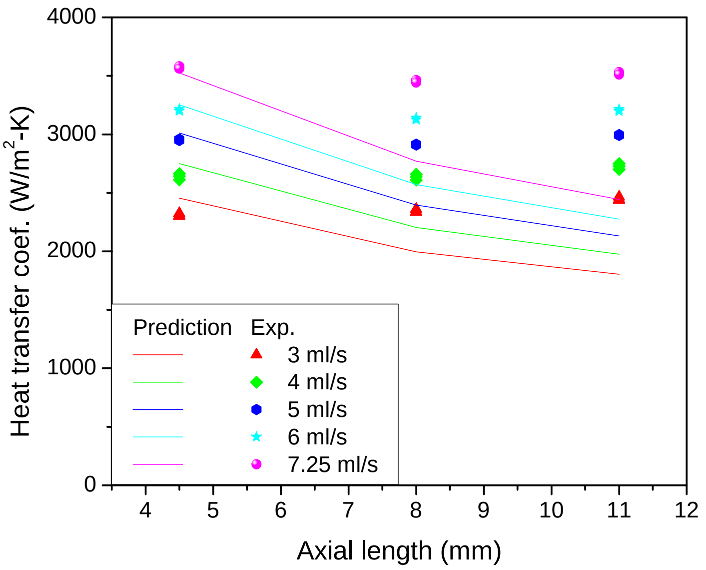

Figure 4.5 Local heat transfer coefficients for the flow of FC-72 in a 120μm gap channel

This phenomenon becomes more prominent as the flow rate decreases. Due to the high air solubility in FC liquids, typically reaching some 50% per volume at atmospheric pressure [26], [27], the effective saturation temperature of the liquid is reduced by as much as 18K. Consequently, pseudo-boiling, associated with the formation and release of bubbles – containing a mixture of gas and vapor - can begin when the wall temperature is still well below the atmospheric pressure saturation temperature of 56°C but exceeds the 38°C saturation temperature of the air-vapor mixture. The formation and release of bubbles on the channel wall can then enhance the heat transfer rate significantly above the theoretical single phase values.

Table 4.1 presents the inlet and outlet temperatures of the FC-72 as well as the average wall temperature and maximum wall temperature for the 120 μm gap channel. The Table reveals that the average wall temperatures for the lowest flow rates were substantially above the 38°C gas-air mixture saturation temperature for the gassy FC-72. It may thus be argued that, as the flow rate decreases, "pseudo boiling" in the channel becomes prominent [27] and acts to increase the heat transfer coefficients in the axial direction. This "gassy enhancement" is partially responsible for the high heat transfer coefficients attained in nominally single-phase flow with FC-72 in these microgap channels.

Table 4.1 Measured temperatures for a 120 µm gap channel with FC-72 as the coolant

Flow rate (ml/s)	Inlet temp. (°C)	Outlet temp. (°C)	Average wall temp. (°C)	Maximum wall temp. (°C)
2.0	29.45	41.52	50.3	50.6
3.0	28.87	36.6	44.2	44.7
4.0	28.45	34.03	41.2	41.6
5.0	28.36	32.66	39.4	39.8
6.0	28.27	31.82	38.3	38.7
7.25	28.27	31.29	37.4	37.9

4. 4 Two-Phase Heat Transfer

Phase change heat transfer in parallel plate micro-gaps was investigated by several researchers. Lee and Lee [28] used R113 in a 300 mm long, 20mm wide single horizontal rectangular gap with the hydraulic diameter, approximately twice the gap height, varying from 0.784 – 3.636 mm, for flow rates varying from 52 to 208 kg/m^2-s, and wall heat flux of 3 to15 W/m^2. In analyzing their 491 data points, they accounted for pressure-induced variations in the saturation temperature along the channel. Heat transfer coefficients were found to be in the range of 5 kW/m^2-K and the experimentally measured total pressure drop reached up to 40 kPa [28].

Yang and Fujita [29] used R113 in a very similar experimental setup; 100mm long single horizontal rectangular gap, with the width fixed at 20 mm while the height varied from 0.2 mm to 2 mm, to yield hydraulic diameters from 0.396 mm to 3.636

mm. In their database of 292 points, they observed the usual flow patterns in the largest gap of 2 mm, with the lowest heat transfer coefficient. New combinations of flow patterns were identified, particularly in the 0.2 mm gap with the highest heat transfer coefficient, in which local dry out in the middle of the channel appeared to occur at a low overall vapor quality, with some of the liquid inventory trapped in the channel corners. Micro-bubbles were assumed to be generated in those corners. In these experiments [29] the mass flux ranged from 100 to 200 kg/m^{2}s, heat flux varied from 20 to 90 kW/m^2, pressure drop reported was as high as 118 kPa, and the flow boiling heat transfer coefficient measured reached as high as 10 kW/m^2-K [29].

Kuznetsov and Shamirzaev [30] studied R22 in a single vertical channel with dimension of 1.6 mm by 6.3 mm that yields a hydraulic diameter of 2.552 mm. The heat transfer coefficient was calculated based on the saturation temperature at each site, using a linear interpolation for the local pressure between the measured inlet and outlet values. They ascribed their observed behavior to the dominance of convective boiling even at low vapor qualities and associated the steep heat transfer coefficient increases at qualities greater than 0.5 with a domain dominated by the thin film evaporation mechanism [30].

4.4.1 Taitel-Dukler Two-phase flow regime map

The flow of a two-phase mixture in pipes has different characteristics from single-phase flow, due to the formation of an interface between the two phases. The action of gravity, along with drag forces, surface tension forces, and turbulence are responsible for creating distinct flow patterns and gas-liquid distribution patterns in two-phase flow. Following the methodology initially developed by Taitel and Dukler [31], a flow regime map – based on physics-based criteria for the transitions among the regimes - can be developed for two-phase flow in a microgap channel for the dimensions and working fluids of interest.

Figure 4.6 displays the flow patterns of co-current flow of a gas and liquid mixture in a horizontal tube and Figure 4.7 displays such a flow regime map for FC-72 flowing in a channel with a height of 0.26 mm and width of 31 mm, or a 0.52 mm hydraulic diameter. The map presents the zones occupied by the four primary flow regimes for horizontal pipe flow:

- **Bubbly flow**: Bubbles of gas move along the upper part of the pipe due to buoyancy and move at nearly same velocity as the liquid
- **Intermittent-Slug**: in this regime, large amplitude waves intermittently wash the top of the tube with smaller waves in-between. At higher gas velocity, the diameter of the elongated bubbles formed by the coalescence of smaller bubbles becomes similar to the channel height.
- **Stratified**: this regime occurs at low liquid and gas velocity. In this regime, the gas flows along the top and the liquid along the bottom of the channel, separated by an undisturbed interface. The two phases are completely separated.
- **Annular**: this regime occurs at higher gas velocity and involves the formation of a continuous liquid film, or annulus, around the perimeter of the tube.

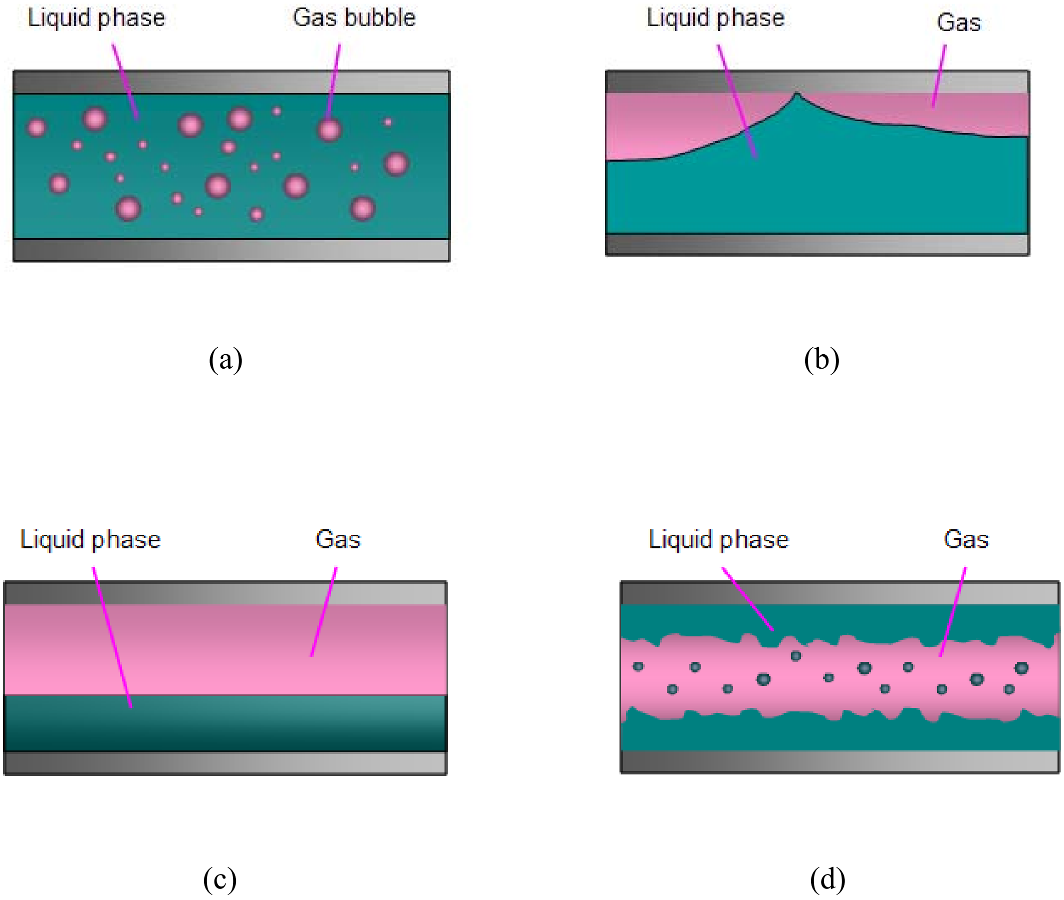

Figure 4.6 flow patterns of gas and liquid mixture in a horizontal tube (a) Bubbly flow, (b) Intermittent-Slug, (c) Stratified and (d) Annular flow

Examining the flow regime map, Figure 4.7, at a point with a superficial liquid velocity of 0.001 m/s and superficial gas velocity of 0.1 m/s, we can see the point falls into the stratified flow regime, which is identified by a liquid layer flowing on the bottom of the channel and a vapor film flowing on top. Increasing the superficial liquid velocity, which can be achieved by increasing the mass flow rate, will lead to the increase of the thickness of the liquid layer flowing in the channel; therefore waves on the liquid surface will be able to reach the top of the channel and form liquid plugs that surround the vapor slugs and together constitute the intermittent-slug flow regime. This transition on this sample map occurs at a superficial liquid velocity of 0.008 m/s for a superficial gas velocity of 0.1 m/s. Increasing the superficial liquid velocity, while keeping the superficial gas velocity constant at 0.1 m/s, will lead to a transition to a bubbly flow at a superficial liquid velocity of 0.6 m/s. This transition mainly occurs when the liquid inventory in the channel is high enough to cause the break down of the vapor slugs into dispersed bubbles.

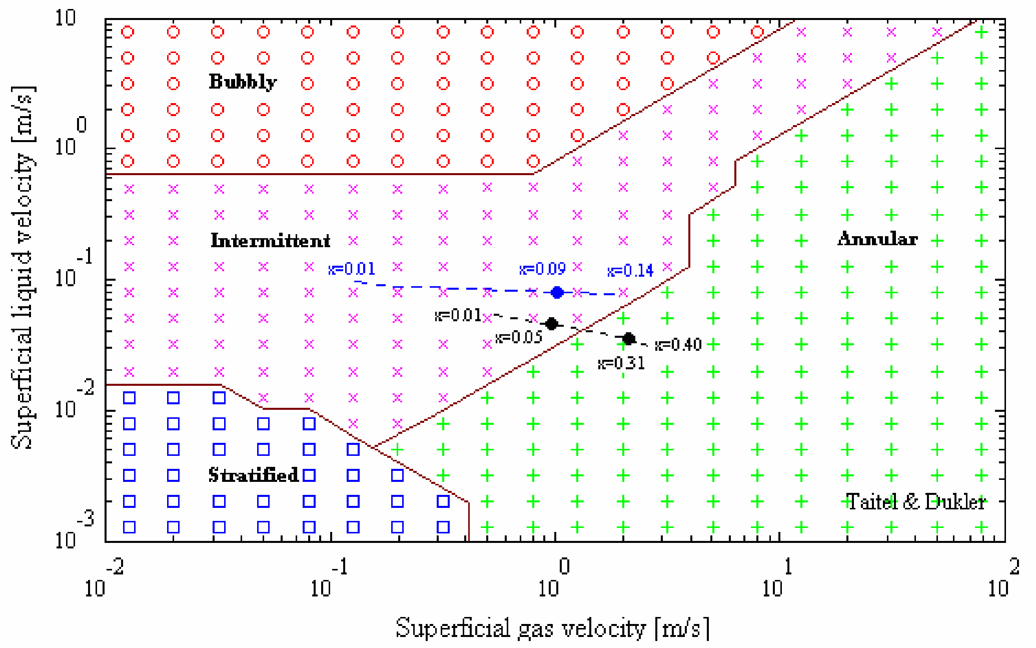

Figure 4.7 FC-72, $D_h = 0.52mm$, $G = 80 \sim 170\ kg/m^2-s$, $q'' = 51 \sim 64\ kW/m^2$ Upper locus $G = 170\ kg/m^2-s$, Lower Locus $G = 80\ kg/m^2-s$ [32]

Starting in the Bubbly flow regime, with a superficial liquid velocity of 1 m/s and a superficial gas velocity of 0.1 m/s, and increasing the superficial gas velocity, as occurs in an evaporation process, the bubbles get larger and tend to agglomerate into slugs. At an approximate superficial gas velocity of 1.5 m/s, the dominant flow regime becomes Intermittent-Slug. With further increase of the vapor quality and therefore the superficial gas velocity to an approximate value of 10 m/s, the vapor core expands to such an extent that it can break through the liquid plug and push the liquid mass towards the channel's walls to form a liquid film, which constitutes the annular flow regime. In horizontal flow, the Annular flow regime remains stable as long as the vapor core is capable of providing the shear stress necessary to sustain the liquid film and prevent it from breaking or falling. The flow regime map shows a transition from stratified to annular flow as gas velocity is increased, for a low liquid velocity. For a high liquid velocity, an increasing gas velocity can produce a transition from dispersed bubble flow to intermittent slug flow, and eventually to annular flow. For the stated conditions of this study, it is possible to conclude that a transition from Intermittent flow to Annular flow will occur at a superficial gas velocity of approximately 1 m/s and superficial liquid velocity of approximately 0.03 m/s. The upper locus is under the condition of mass flux 174 kg/m^2-s and heat flux 64 kW/m^2. The locus shows that in order to enter the Annular regime the quality should be more than 0.15 for this case. The lower locus is under the condition of mass flux 87 kg/m^2-s and heat flux of 51 kW/m^2. Under this condition, the flow enters Annular regime when the quality becomes greater than 0.1.

4.4.2 Heat Transfer Coefficients

The Chen correlation [33], originally developed to fit flow boiling data for water, is one of the most enduring and widely used correlations for the prediction of two-phase heat transfer coefficients. The original rationale of the correlation was that the heat transfer coefficient (h) for saturated convective boiling consisted of a microscopic contribution and a macroscopic contribution, as in:

$$h = h_{mic} + h_{mac} \tag{4.11}$$

The microscopic contribution is thought to be primarily due to nucleate pool boiling, whereas the macroscopic contribution is thought to be due to the bulk convective flow. The macroscopic contribution was calculated using the Dangler Addoms correlation with a Prandtl number correction factor to generalize the correlation to the various working fluids and expressed by Eq. (4.12).

$$h_{mac} = h_l F\left(X_{tt}\right) \mathrm{Pr}_l^{0.296} \tag{4.12}$$

where F is an empirically-determined enhancement factor and h_l is single-phase liquid heat transfer coefficient and is calculated by

$$h_l = 0.023\left(\frac{k_l}{D}\right) \mathrm{Re}_l^{0.8}\, \mathrm{Pr}_l^{0.4} \tag{4.13}$$

where $\mathrm{Re}_l = \dfrac{G(1-x)D}{\mu_l}$.

The microscopic contribution was calculated using the Forster-Zuber correlation for pool boiling with an additional correction factor.

$$h_{mic} = 0.00122\left[\frac{k_l^{0.79} C_{pl}^{0.45} \rho_l^{0.49}}{\sigma^{0.5} \mu_l^{0.29} h_{fg}^{0.24} \rho_g^{0.24}}\right] \Delta T_{sat}^{0.24} \Delta P_{sat}^{0.75} S \tag{4.14}$$

where S is suppression factor and is function of two-phase Reynolds number:

$$\mathrm{Re}_{tp} = \mathrm{Re}_l \left[F(X_{tt})\right]^{1.25} \tag{4.15}$$

In order to calculate the suppression factor Collier [34] found the following empirical fit:

$$S(\mathrm{Re}_{tp}) = \left(1.25 + 2.56\ x10^{-6} \cdot \mathrm{Re}_{tp}^{1.17}\right)^{-1} \tag{4.16}$$

Collier also developed empirical fits for the $F(X_{tt})$ enhancement factor:

$$F(X_{tt}) = 1 \qquad \text{for } X_{tt}^{-1} \le 0.1$$

$$F(X_{tt}) = 2.35\left(0.213 + \frac{1}{X_{tt}}\right)^{0.736} \qquad \text{for } X_{tt}^{-1} > 0.1 \tag{4.17}$$

where X_{tt} is the Martinelli parameter and is calculated as:

$$X_{tt} = \left(\frac{1-x}{x}\right)^{0.9} \left(\frac{\rho_g}{\rho_l}\right)^{0.5} \left(\frac{\mu_l}{\mu_g}\right)^{0.1} \tag{4.18}$$

The Shah correlation [35] is very similar to the Chen correlation in that both the nucleate boiling and convective boiling mechanisms are calculated. The Shah correlation, however, is different in that it equates the two-phase heat transfer coefficient to the value of the dominant mechanisms rather than summing their individual contributions. Shah employs four dimensionless parameters defined by

$$\psi = \frac{h_{tp}}{h_l} \tag{4.19}$$

$$Co = \left(\frac{1-x}{x}\right)^{0.8} \frac{\rho_g}{\rho_l} \tag{4.20}$$

$$Bo = \frac{q''}{G h_{\lg}} \tag{4.21}$$

$$Fr_l = \frac{G^2}{\rho_l^2 gD} \tag{4.22}$$

where Co is the Convection number, Bo is the boiling number and Fr_l is the Froud number assuming all the mass to be flowing in liquid form and h_l is calculated by the Dittus-Boelter equation as:

$$h_l = 0.023\left[\frac{G(1-x)D}{\mu_l}\right]^{0.8} \Pr_l^{0.4} \frac{k_l}{D} \tag{4.23}$$

The original correlation proposed by Shah was hard to use in graphical form. Later [36], he developed the equations provided below.

For $N > 1$

$$\psi_{nb} = 230Bo^{0.5} \qquad \text{for } Bo > 0.3E-4 \tag{4.24}$$

$$\psi_{nb} = 1 + 46Bo^{0.5} \qquad \text{for } Bo \leq 0.3E-4 \tag{4.25}$$

where $\boldsymbol{\psi_{nb}}$ is the value of ψ in the pure nucleate boiling regime.

$$\boldsymbol{\psi_{cb}} = \frac{1.8}{\boldsymbol{N}^{0.8}} \tag{4.26}$$

where $\boldsymbol{\psi_{cb}}$ is value of ψ in the pure convective boiling regime.

$$\psi = \max(\psi_{cb}, \psi_{nb}) \tag{4.27}$$

N is defined as:

$$N = Co \qquad \text{for } Fr_l \geq 0.04 \tag{4.28}$$

$$N = 0.038Fr_l^{-0.3}Co \qquad \text{for } Fr_l \geq 0.04 \tag{4.29}$$

For $N \leq 1$

$$\psi_{bs} = F \cdot Bo^{0.5} \exp(2.47N^{-0.1}) \qquad \text{for } 0.1 < N \leq 1 \tag{4.30}$$

$$\psi_{bs} = F \cdot Bo^{0.5} \exp(2.47N^{-0.15}) \qquad \text{for } N \leq 0.1 \qquad (4.31)$$

where ψ_{bs} is value of ψ in the bubble suppression regime.

$$F = 14.7 \qquad \text{for } Bo \geq 11E-4 \qquad (4.32)$$

$$F = 15.4 \qquad \text{for } Bo < 11E-4 \qquad (4.33)$$

ψ_{cb} is calculated by Eq.(4.26) and

$$\psi = \max(\psi_{bs}, \psi_{cb}) \qquad (4.34)$$

These correlations were found to have acceptable agreement with mini-gap data for the Intermittent-slug regime and the relatively low quality regions of the annular flow regimes by Bar-Cohen et al. [37].

4.4.3 Inverse Wall Heat Flux Calculation

For the two-phase experiments, the same experimental apparatus was used as in the single phase experiments and the experiment was performed at flow rates of 0.42 ml/s and 0.83 ml/s. Convective heat transfer coefficients predicted by the detailed thermo-fluid Computational Fluid Dynamics software product IcePak ver. 4.1 model were earlier shown to yield very good agreement with the analytical values and experimental results. In this part of the study, the IcePak model was exercised with a series of assumed heat transfer coefficients until the computed wall temperatures matched to the measured wall temperatures and calculated heat transfer coefficient matched to the assumed heat transfer coefficient. Then, from the ratio of the "inversely" computed wall heat fluxes to the input power, the conversion efficiency is determined. The number of element in this model was 1040k. Figure 4.8 shows the comparison of temperature profile of channel axial length between experiment and inversely calculated IcePak result, the heat flux contour of 260 µm gap channel at mass flux 53 kg/m^2-s, and photograph of the heater. Figure 4.8 (a) is the comparison of axial length wall temperature between experiment and inversely calculated IcePak result. 5% error bar is drawn in Figure 4.8 (b) and the temperature deviation is less than 1.1˚C. As shown in Figure 4.8 (b), the heat flux decreases in the axial direction of the channel and the heat flux on both sides is approximately 83% of the center. The lower heat flux near the edge is due to the heat losses to the sides from the copper block which reduce the heat flux near the edge. The axial decreasing of the heat flux is due to the shorter length of the heater than the copper block, creating an unheated, down stream section of the channel wall. As shown in Figure 4.8 (c) the effective heating area of the heater is 25.4 mm and it can cover 75% of the axial channel length. The CFD results were also used to determine the net heat transfer into the channel, as well as the resulting thermodynamic quality at various channel locations. From the IcePak model, it was determined that over the range of the experimental conditions, 68% to 75% of the heat generated was transferred into the channel and contributed to the phase change process.

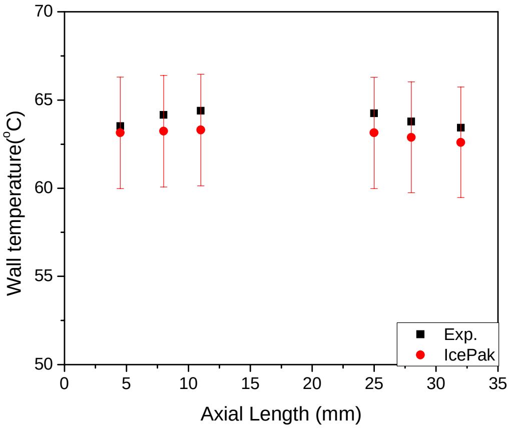

(a)

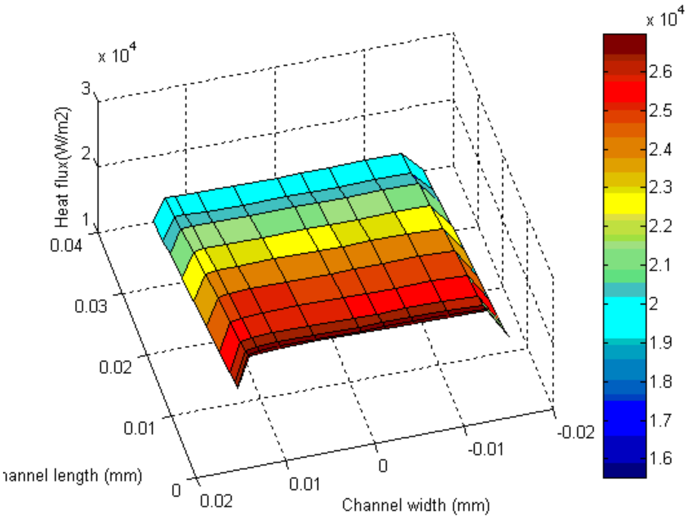

(b)

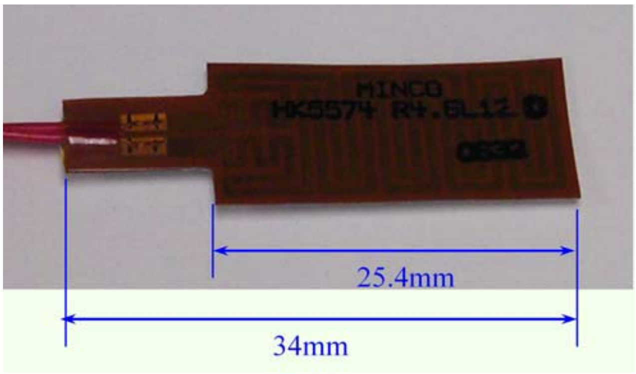

(c)

Figure 4.8 (a) Temperature profile of the channel axial length (b) numerically-determined microgap heat flux contours of 260 µm gap channel at G=50 kg/m^2-s, and (c)photograph of heater

4.4.4 Experimental Results

Due to heat addition to the channel, the flow quality increased axially in the channel. Figure 4.9 presents the flow regime map for the gap of 120 µm at the mass flux of 180 kg/m^{2}s and volumetric flow rate of 0.42 ml/s. For the conditions of Fig 4.9, the two-phase flow of FC-72 was found in the annular flow regime for the imposed flow rate of 0.40 ml/s. Subcooled flow boiling, with zero superficial gas velocity, was observed at the flow rate of 0.80 ml/s, and hence the superficial velocity locus does not appear on the figure. This Taitel and Dukler map displays the four primary flow regimes and the locus traversed on the superficial velocity coordinates by the reported data points.

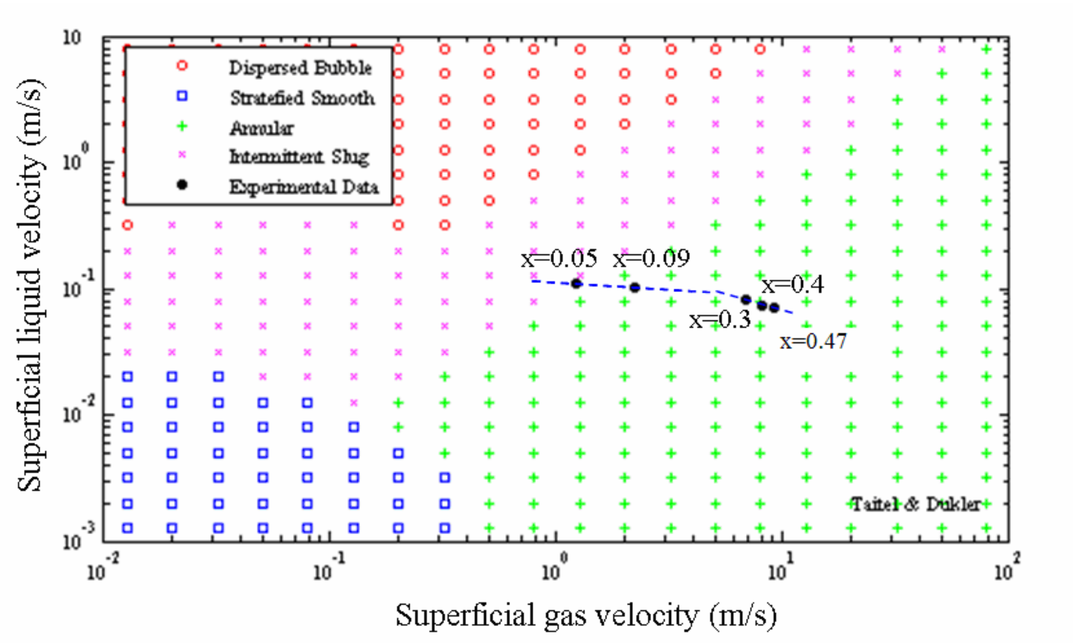

Figure 4.9 Two-Phase Flow Regime Map and Experimental Locus for FC-72, $D_h = 0.24mm$, $G = 180kg/m^2 - s$, and $q'' = 58kW/m^2$

Figure 4.10 displays the flow regime maps for FC-72 flowing in a channel with a larger gap of 260 μm and width of 31 mm, yielding a 520 μm hydraulic diameter. For the 0.83ml/s flow rate, the current data seem all to fall into the Intermittent flow regime. It should be noted that the maximum heat flux of approximately 75 kW/m^2 achievable in the current apparatus and the relatively high cooling capacity of fast flowing FC-72 liquid, were found to limit the number of useful two-phase heat transfer data points obtained in this first phase of the study.

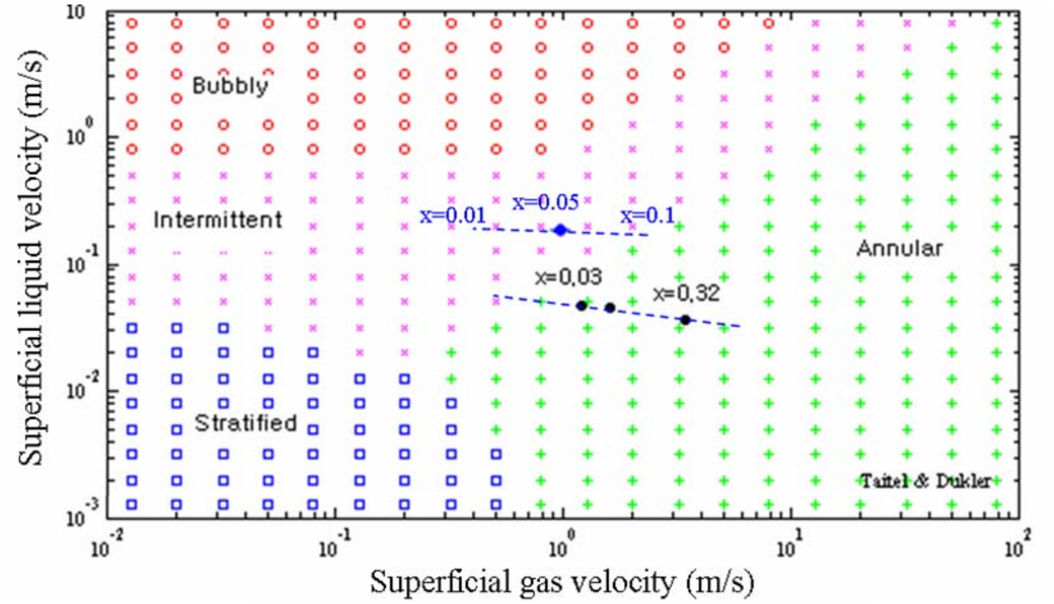

Figure 4.10 Two-Phase Flow Regime Map and Experimental Locus for FC-72, $D_h = 0.52mm$, $q'' = 58kW/m^2$ Upper locus $G = 170kg/m^2 - s$, Lower Locus $G = 80kg/m^2 - s$

The “inversely” calculated two-phase FC-72 heat transfer coefficients for these experiments, for the conditions displayed in the flow regime map of Figure 4.8, are compared in Table 4.2 and 4.3 to the values predicted by the Chen [33] and Shah [35] two-phase heat transfer correlations. The heat transfer coefficient predictions based on the Chen (Eq.4.11~4.18) and Shah (Eq. 4.19~4.23) correlations, respectively, at the indicated quality are listed in the last two columns of the Tables.

Table 4.2 Flow boiling of FC-72 in a 120 µm single gap channel

Remark	**D (mm)**	**q" (kW/m^2)**	**G (kg/m^{2}s)**	**Volumetric Flow Rate (ml/s)**	**x (Average quality)**	**Flow Regime**	**h (W/m^{2}K)**	**Chen Prediction (W/m^{2}K)**	**Shah Prediction (W/m^{2}K)**
Average value of Intermittent flow	0.24	30.2	180	0.40	0.073	Intermittent	6450	3100	6350
Average value of Annular flow	0.24	30.2	180	0.40	0.34	Annular	5700	5850	7450
Average Values over the entire channel	0.24	30.2	180	0.40	0.26		6050	4430	6900

Table 4.3 Flow boiling of FC-72 in a 260 µm single gap channel

Remark	**D (mm)**	**q" (kW/m^2)**	**G (kg/m^{2}S)**	**Volumetric Flow Rate (ml/s)**	**x Average quality**	**Flow Regime**	**h (W/m^{2}K)**	**Chen Prediction (W/m^{2}k)**	**Shah Prediction (W/m^{2}k)**
Average Values over the entire channel	0.52	30.2	80	0.40	0.13	Annular	2954	2100	3500
Average Values over the entire channel	0.52	30.9	170	0.80	0.05	Intermittent	3952	3695	6742

When comparing the correlations of Chen and Shah to available data for R-22 and R-113 in single gap channels [28]-[30], it was found that the correlations provided average error of approximately 28% for Chen and 27% for Shah with the available data. The authors, thus, concluded that the Shah correlation could be used successfully to predict the thermal transport in both flow regimes, while the Chen correlation should be preferred for the low-quality annular sub-domain and should not be used in the Intermittent regime for these microgap channels. For the 120 µm channel, the experimental two-phase heat transfer coefficients agree well with these recommendations, with the Shah correlation appearing to fall quite close to the

Intermittent flow regime heat transfer coefficient (within 3%) and the Chen correlation to the annular flow regime data (within 5%), while the Shah correlation provides agreement to within approximately 15% with the average h for the entire channel. For the 260 µm channel, the measured heat transfer coefficient values are well bounded by the Chen and Shah correlations, respectively, but the average discrepancy is approximately 7% for Chen and 60% for Shah in the Intermittent flow regime, 40% for Chen and 16% for Shah in the Annular flow regime.

4.4.5 IR Image Analysis

G. Hetsroni et al. [38], used an Infrared (IR) camera in order to investigate the temperature distribution along the surface of a triangular microchannel cooled by two-phase flow. The thermofuid characteristics of the previously discussed two-phase flow regimes may result in the nonuniform distribution of the working fluid inside individual channels, as well as across arrays of parallel channels, which can then lead to variation of the local heat transfer coefficients and, as a result, to a nonuniform temperature of the cooled surface. Therefore, Hetsroni et al. [38], used an IR (InfraRed) camera to obtain the thermal image of the heated surface which served as the base for a microchannel cooler. The microchannel was fabricated from a square silicon substrate. The dimensions of the microchannel cooler are 15 x 15 mm^2, and 530 µm in thickness, with 21 parallel triangular cross section etched microchannels. Their conclusion is that, at relatively high heat fluxes, two-phase flow boiling, with its nearly uniform saturation temperature, generates a much more uniform temperature distribution than single-phase flow with its associated sensible temperature rise.

Cortina-Diaz and Schmidt [39] investigated flow boiling heat transfer in a single vertical channel. They used n-Hexane and n-Octane in a single 12.7 mm by 0.3 mm rectangular channel with a hydraulic diameter of 0.586 mm. Infrared thermography was employed to measure the channel surface temperature instead of thermocouples. An IR camera has the capability of continuous and non-contact measurement of wall temperature without barely any time delay. From the data gathered with the IR camera, they confirmed the instability of surface temperature while flow boiling is occurring in the channel. The experiment was run with atmospheric pressure at the outlet. Heat transfer coefficient values were as high as 20 kW/m^2-K [39].

In the present study, the measured thermocouple data were used to calibrate the emissivity of the copper base plate. The IR image of unheated channel is shown in Figure 4.11. The temperature range of IR camera was set between 40˚C and 70˚C, because this was our temperature range of interest. The black circle at the center of Figure 4.11 is the Sapphire window area and the other area is the Plexiglas top plate. Due to the setting of the temperature range (from 40˚C to 70˚C) of the IR camera, it looks like 40°C, but the real temperature of the black circle is 25°C.

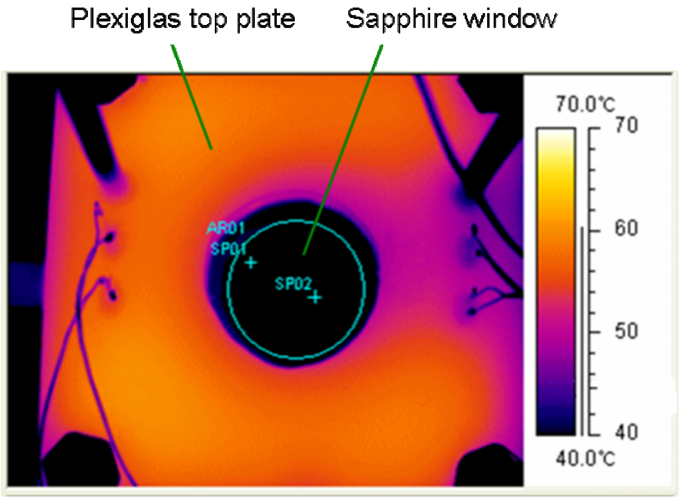

Figure 4.11 IR image of channel

The IR image was captured at different heat fluxes in the channel with hydraulic diameter equal to $D_h = 0.52$ mm and operating at a mass flux of $G = 35$ kg/m^2-s. The information obtained from the IR camera is displayed in three different ways: surface temperature bands across the window area at a specific time, the temporal temperature variations at specific spots on the surface, and a three-dimensional temperature amplitude plot for the entire window area. These sets of figures, for three distinct heat fluxes, provide evidence of significant spatial and temporal temperature variations in the observed area, which appear to reflect the complexity of two phase flow in a microgap channel.

The temperature distribution obtained from the IR camera, across the image area of 286.5 mm^2, is shown in Figure 4.12 (a) - (d) at 4 distinct times and for a heat flux of $q'' = 2.18$ W/cm^2 and Figure 4.12 (e) provides the visual image of the surface under the same conditions.

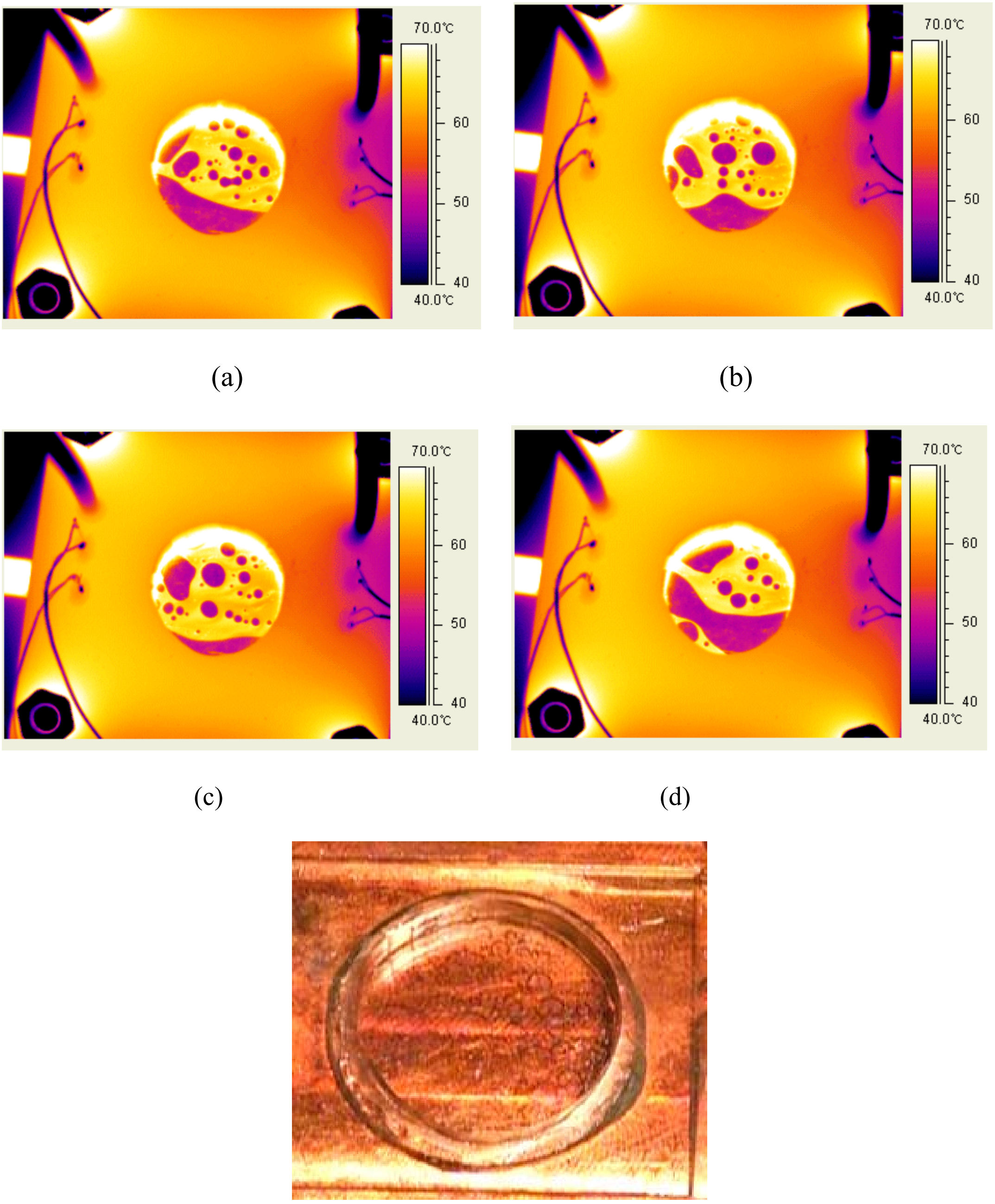

(a) (b)

(c) (d)

(e)

Figure 4.12 (a) - (d) IR images and (e) visual image of $D_h = 0.52mm$, $G = 35kg/m^2 - s$ and $q'' = 2.18W/cm^2$

In Figure 4.12, there are several cold spots of approximately 55°C that appear to be due to the subcooled FC-72 liquid contacting the surface immediately after the departure of a bubble or a temporary local dry out. In these experiments the inlet liquid temperature was 43.3°C and, if it is assumed that the temperature increases linearly along the channel until reaching the saturation temperature, the liquid temperature in the vicinity of the Sapphire window is 55.6°C. Figure 4.13 (a) shows the average temperature of the Sapphire window area and the temperature of the two spots (SP01 and SP02) in Figure 4.11. The black line in Figure 4.13 is the average temperature, the blue line is the temperature of SP01 in Figure 4.11 and the red line is the temperature of SP02 in Figure 4.11. As shown in Figure 4.13, the cold spot temperature on the surface, as in Figure 4.12, is around 55°C. The fluctuation of the temperature at these two spots, SP01 and SP02, is thought to reflect the temporal variations in the local void fraction (Intermittent flow) and local liquid film thickness (Annular flow) in this microgap channel. Figure 4.13 (b) shows the measured temperature by thermocouples which are located under the wetted surface of the channel. The temperature of measured thermocouple and average temperature of measured IR camera agree well. Figure 4.13 (c) shows the flow regime map under this condition. Due to low heat flux, positive quality can be obtained only close to the end of the channel. Under this condition, the xhannel is operating in the Intermittent regime, but very close to the Annular regime.

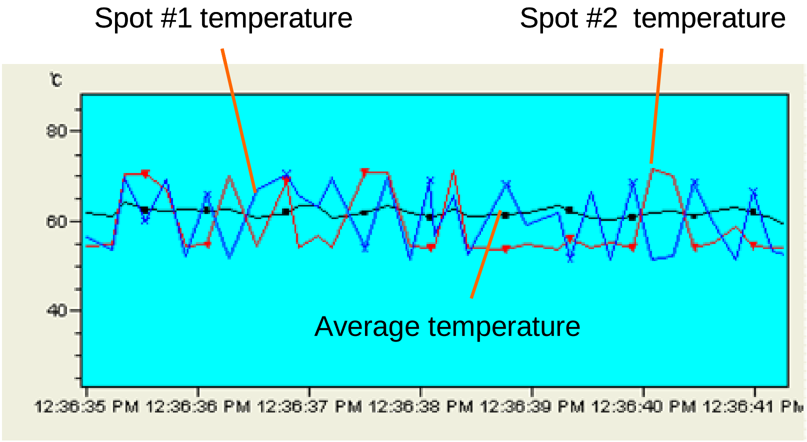
Spot #1 temperature
Spot #2 temperature
Average temperature
℃
80
60
40
12:36:35 PM
12:36:36 PM
12:36:37 PM
12:36:38 PM
12:36:39 PM
12:36:40 PM
12:36:41 PM

(a)

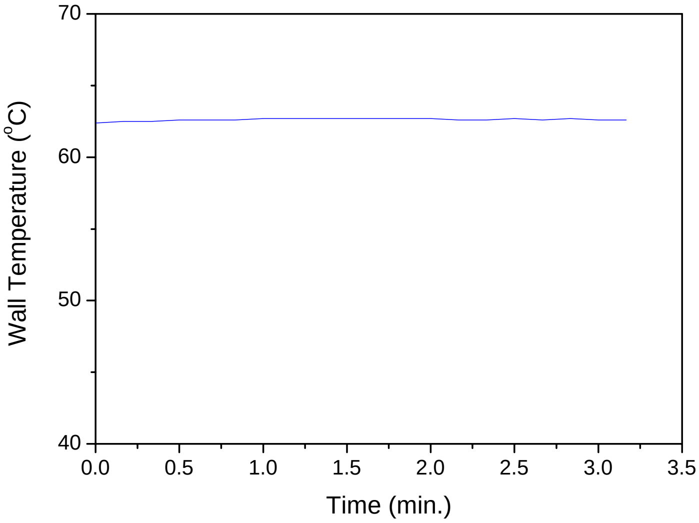
70
60
50
40
Wall Temperature (°C)
0.0
0.5
1.0
1.5
2.0
2.5
3.0
3.5
Time (min.)

(b)

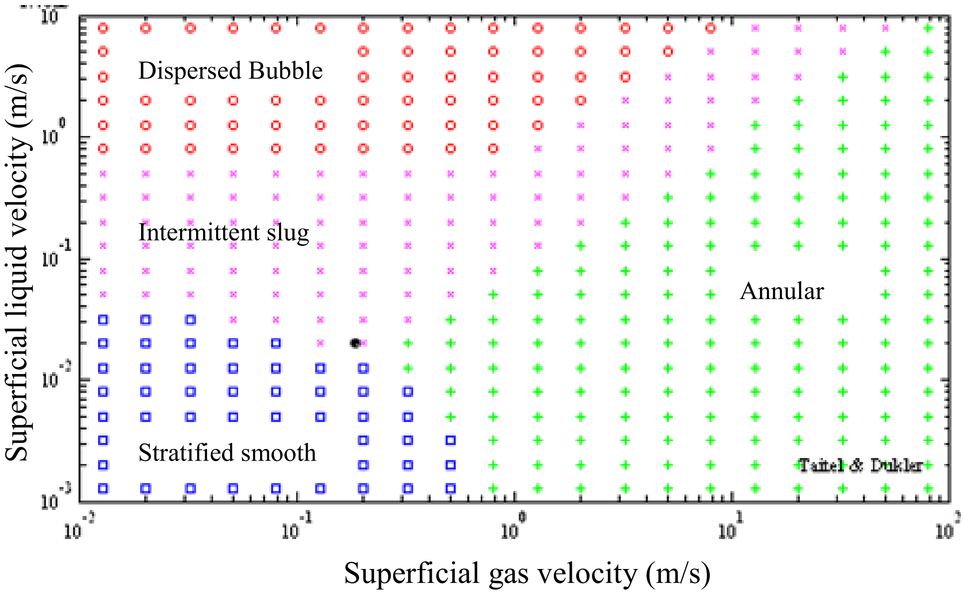

(c)

Figure 4.13 (a) Measured temperature by IR camera, (b) measured temperature by thermocouple below the wetted surface and (c) flow regime map under the condition of $D_h = 0.52mm$, $G = 35kg/m^2 - s$ and $q'' = 2.18W/cm^2$

Figure 4.14 shows the three-dimensional temperature amplitude, or surface, plot, based on the values obtained from the IR images. This representation of the surface temperature variations makes it relatively easy to determine the fraction of the surface above or below a specified temperature. For the conditions of Figure 4.14, the fraction below the saturation temperature is 37.5%. This is due to the subcoold liquid of the channel inlet. As shown in Figure 4.12 (e) the subcooled liquid entered (from the right side of the figure) to the IR window area and it changed to the saturation liquid.

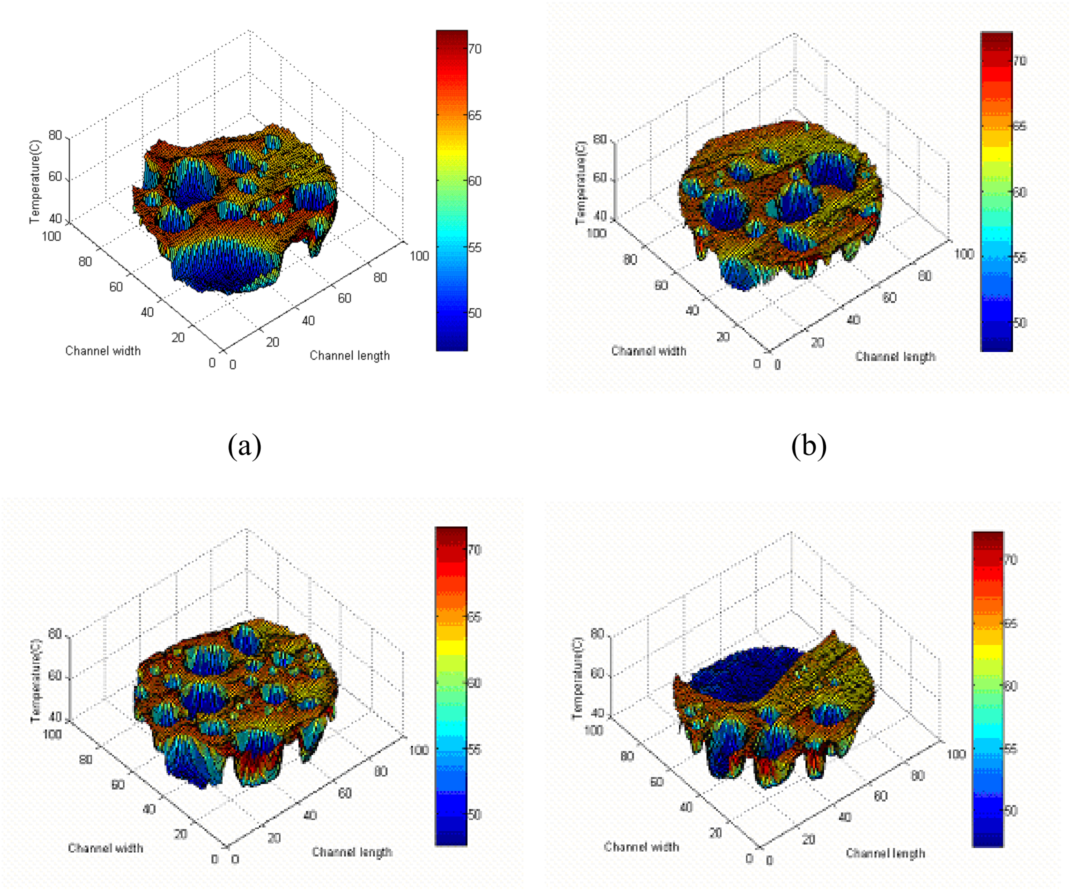

(a) (b)

(c) (d)

Figure 4.14 (a) - (d) 3-D temperature field of IR images of $D_h = 0.52mm$, $G = 35kg/m^2 - s$ and $q'' = 2.18W/cm^2$

The conditions of Figure 4.15 are nearly the same as those of Figure 4.12 but the channel is operating at a slightly higher heat flux ($q'' = 2.6W/cm^2$) than Figure 4.12.

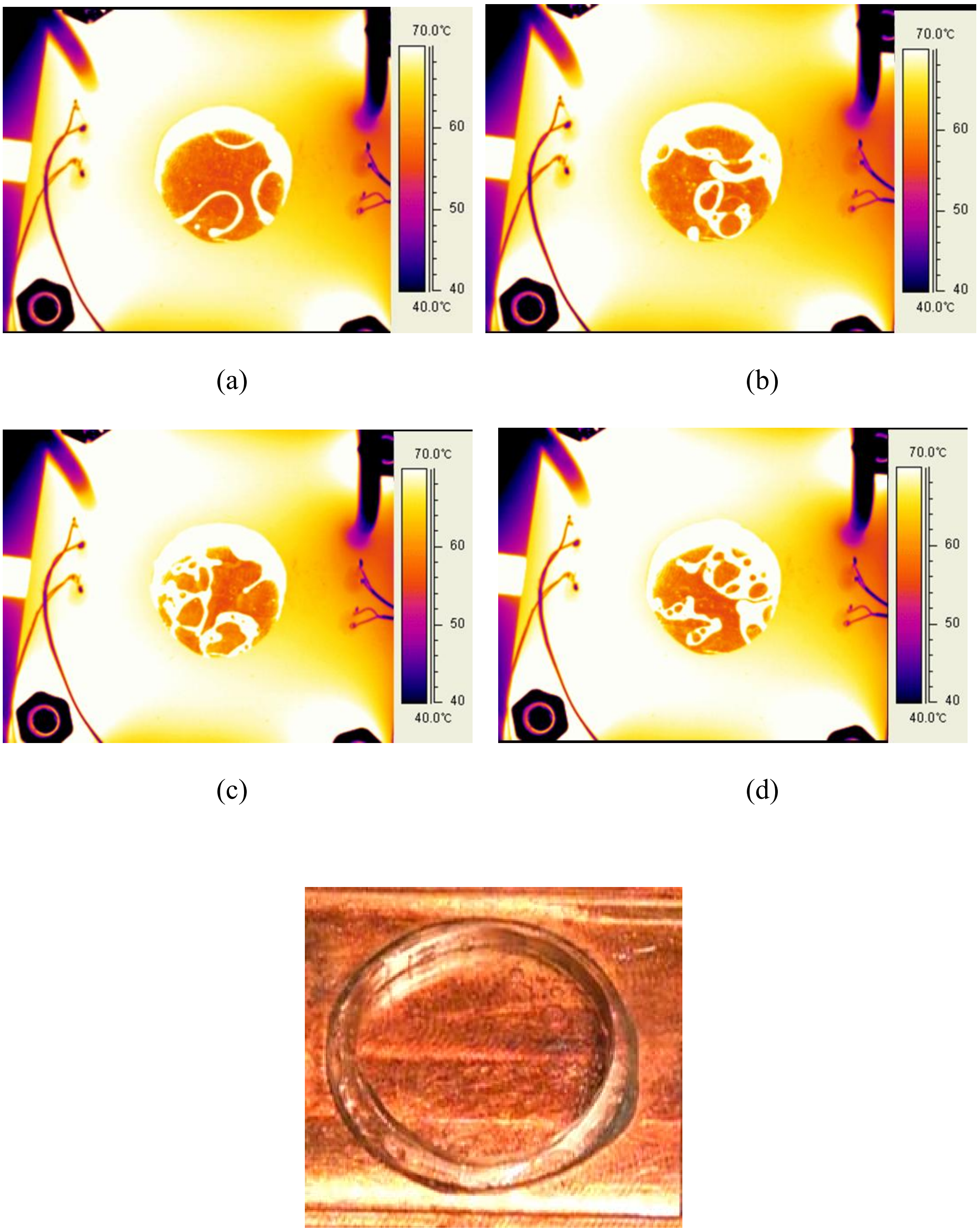

(a)

(b)

(c)

(d)

(e)

Figure 4.15 (a) - (d) IR images and (e) visual image of $D_h = 0.52mm$, $G = 35kg/m^2 - s$ and $q'' = 2.6W/cm^2$

As shown in Figure 4. 15, the increase of heat flux increases the temperature of the copper block. The white area of the IR image is hot spots which are close to 70°C or higher. The visual image, Figure 4.15 (e), shows that the bubble area of the channel decreases compared to the Figure 4.12 (e). Figure 4.16 (a) shows the average temperature of the sapphire window area and the temperature of two distinct spots, shown in Figure 4.11, under this condition. As the heat flux increases, the average temperature of the sapphire window area is increased and the cold spot and hot spot temperature are also increased. However, the spot temperatures are still occasionally below the saturation temperature. This is again thought to reflect the effect of subcoold liquid from the channel inlet contacting the copper surface. For these conditions, the inlet temperature is 44.3°C and the outlet temperature is 59.6°C.

Figure 4.16 (b) shows the measured temperature by the thermocouples which is nearly identical to the average measured temperature by the IR camera. Figure 4.16 (c) shows the flow regime map of this test condition. The flow regime transits from Stratified to Annular flow along the channel.

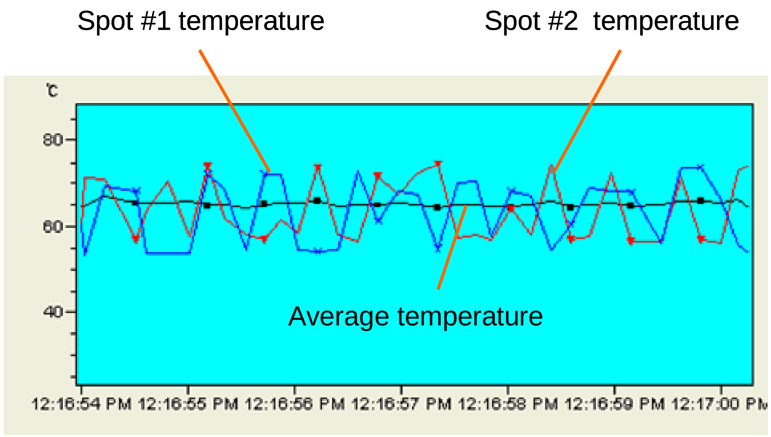

(a)

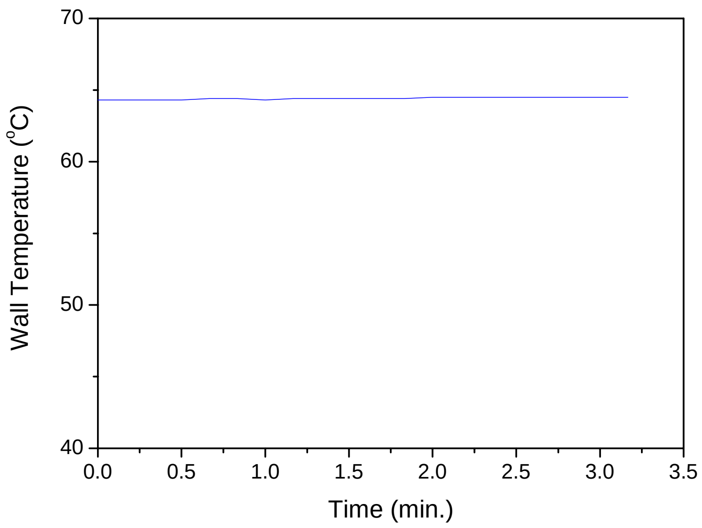

(b)

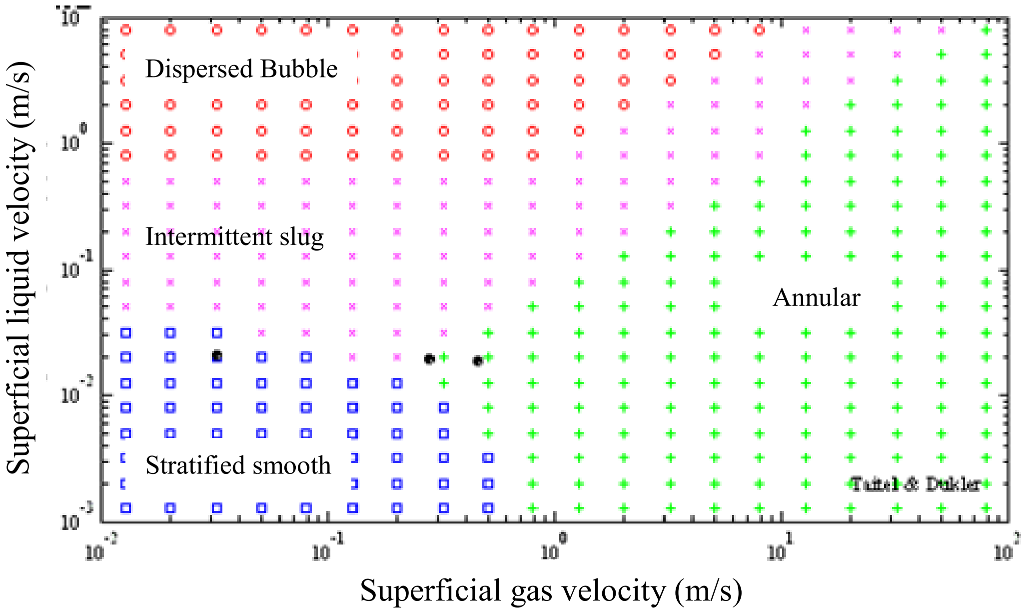

(c)

Figure 4.16 Measured temperature by IR camera, (b) measured temperature by thermocouple below the wetted surface and (c) flow regime map under the condition of $D_h = 0.52mm$, $G = 35kg/m^2 - s$ and $q'' = 2.18W/cm^2$

Figure 4.17 shows the temperature field of IR images. The portion of below saturation temperature decreases to 10.6%.

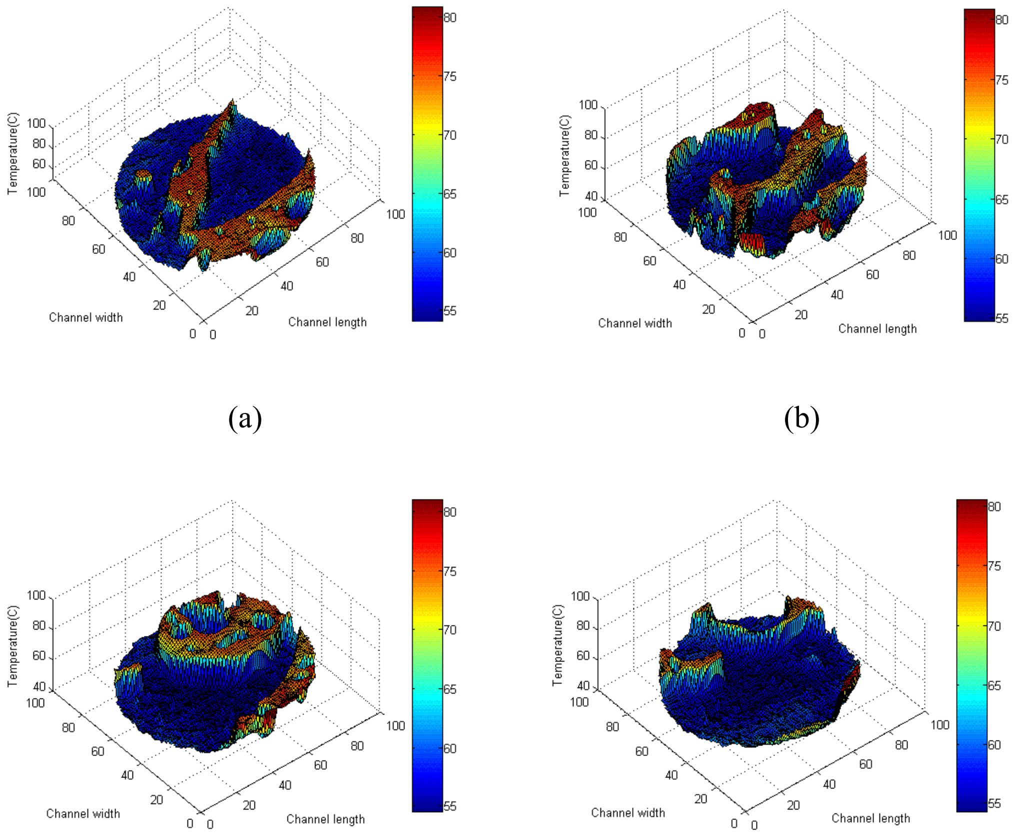

(a) (b)

(c) (d)

Figure 4.17 (a) - (d) 3-D temperature field of IR images of $D_h = 0.52mm$, $G = 35kg/m^2 - s$ and $q'' = 2.6W/cm^2$

Figure 4.18 shows the result of further increasing of heat flux to 3.17 W/cm^2.

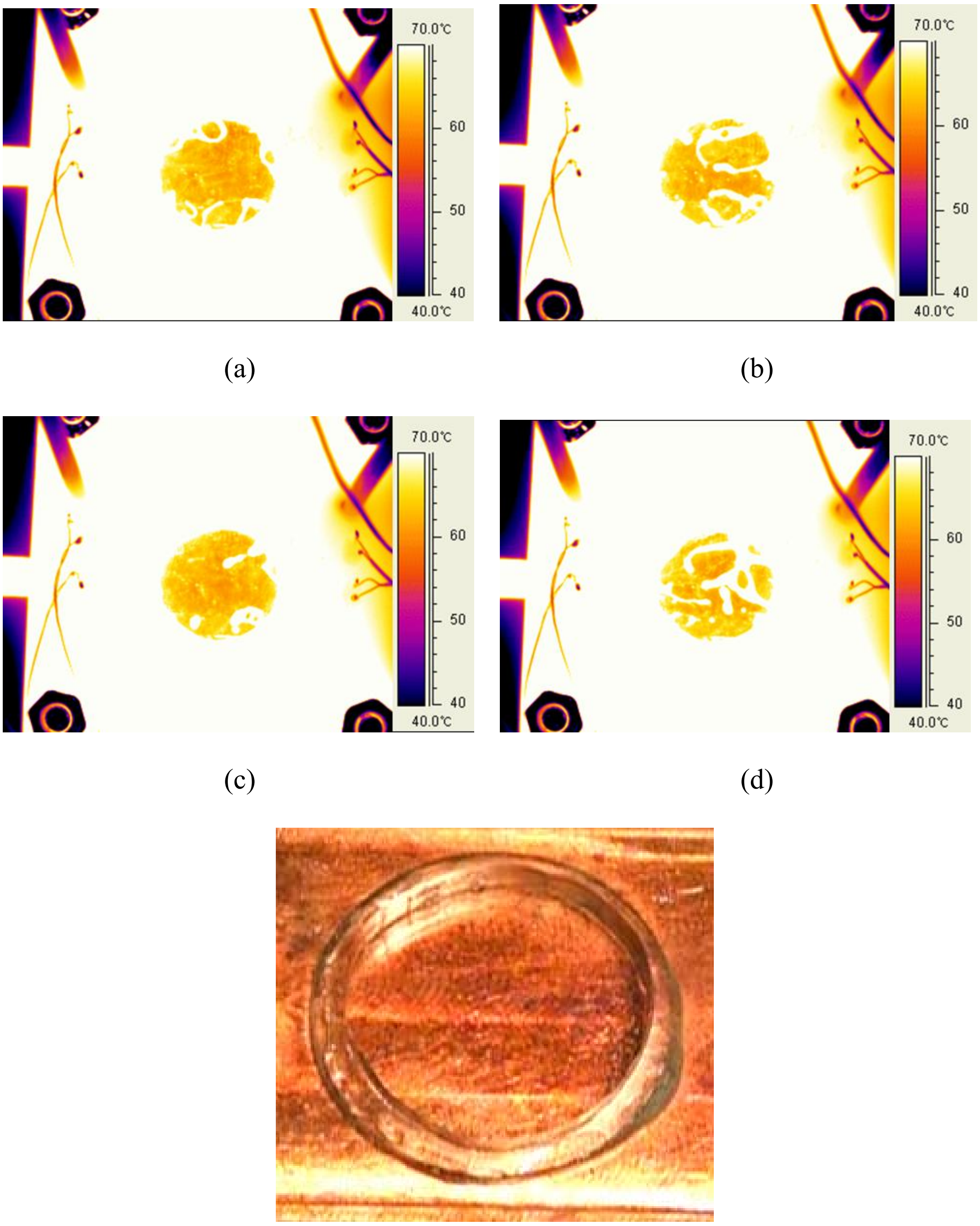

(a) (b)

(c) (d)

(e)

Figure 4.18 (a) - (d) IR images and (e) visual image of $D_h = 0.52mm$, $G = 35kg/m^2 - s$ and $q'' = 3.17W/cm^2$

The conditions of Figure 4.18 are nearly the same as those of Figure 4.12 and Figure 4.15 but the channel is operating at a higher heat flux than in Figure 4.15. This appears to cause a higher average temperature and in the visual image of this condition, as shown in Figure 4.18 (e), no bubble is observed. Figure 4.19 (a) shows the average temperature of the Sapphire window area and temperature of the two spots under this condition. As shown in the Figure 4.19, the average temperature increased and it is between 65°C and 70°C. Figure 4.19 (b) and (c) shows the measured temperature by thermocouple and flow regime map under this test condition. Under this condition the flow in the channel falls into the Annular regime.

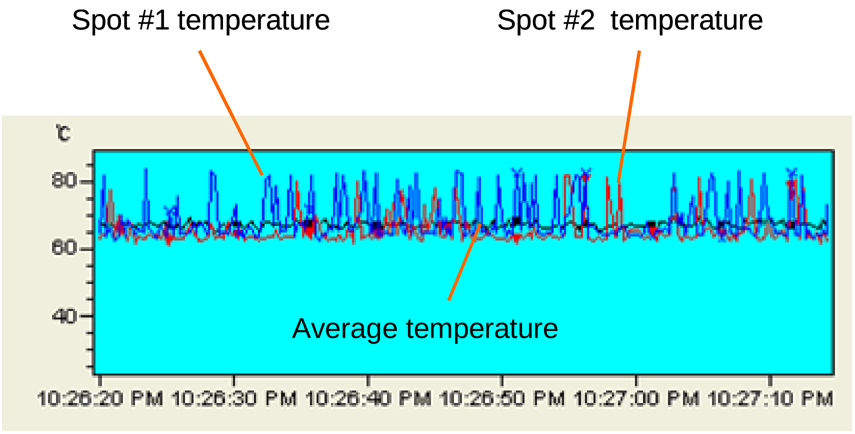

(a)

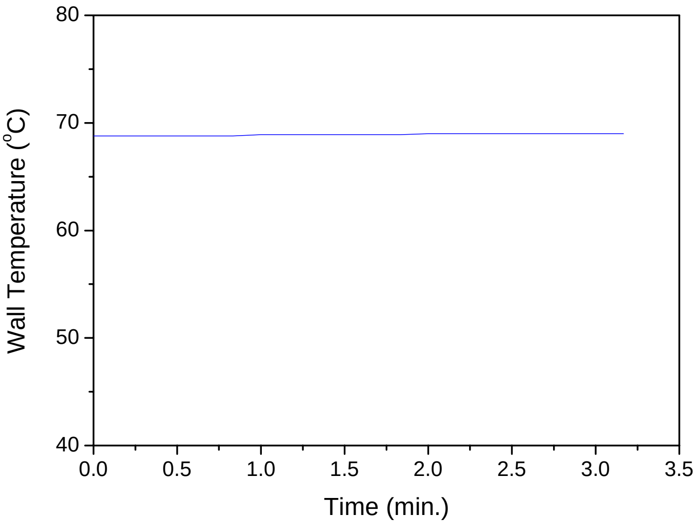

(b)

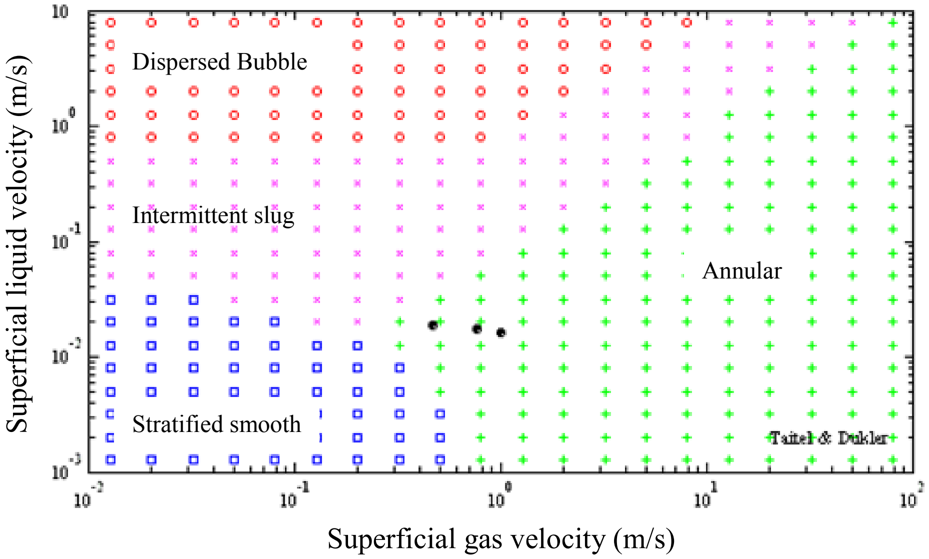

(c)

Figure 4.19 Measured temperature by IR camera, (b) measured temperature by thermocouple below the wetted surface and (c) flow regime map under the condition of $D_h = 0.52mm$, $G = 35kg/m^2 - s$ and $q'' = 3.17W/cm^2$

Figure 4.20 is the 3-D temperature field of this condition. There is no cold spot below the saturation temperature.

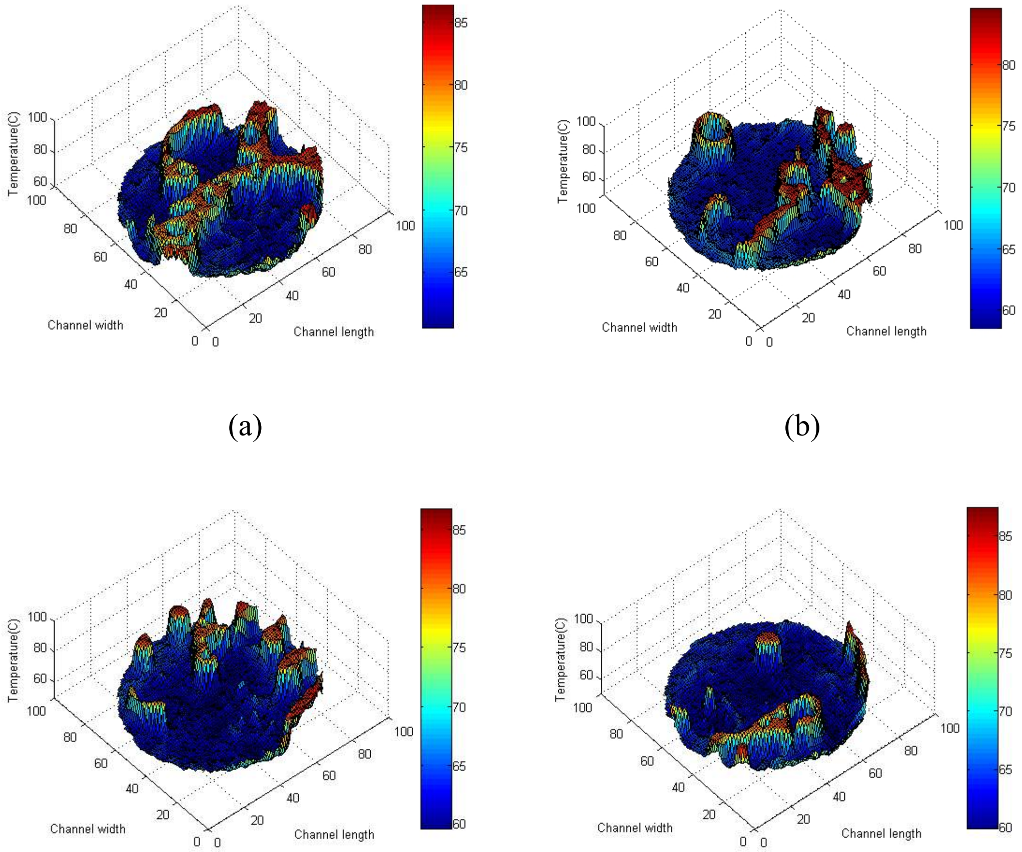

(a) (b)

(c) (d)

Figure 4.20 (a) - (d) 3-D temperature field of IR images of $D_h = 0.52mm$, $G = 35kg/m^2 - s$ and $q'' = 3.17W/cm^2$

It may be argued that the high temperature area of this Figure 4.20, occupying approximately 23% of the imaging area, would be due to a local and often temporary hydrodynamic axial distance. Alternatively, the coolest areas may be due to very high heat transfer coefficients where thin liquid films are experiencing rapid evaporation.

4.5 Conclusion

In this chapter the theoretical background of single-phase and two-phase heat transfer coefficient and pressure drop in narrow parallel plate channels was presented and the theoretical results compared with the preliminary experiment result. The pressure drop measurement was accurate and the thermo-fluid results of single-phase experiments with water agreed well with the predictions. A “pseudo boiling” phenomena, caused by the presence of dissolved gas, was found to enhance the heat transfer coefficient of FC-72. For the two-phase experiment, it was observed that the heat transfer rates and coefficients are in the range of the prediction of correlations which were developed by several researchers. However, due to the low heat flux of the heater, it was impossible to perform experiment with high heat flux which was the goal of this study. Therefore, in the next chapter, a narrow channel, which has the same width as the heater, will be tested with a much higher heat flux heater.

Chapter 5

Micro-gap narrow channel

This chapter deals with the fabrication and testing of a micro-gap narrow channel attached to a high heat flux heater. In order to minimize the heat loss to the copper base block from conduction, the width of the channel (10 mm) itself is the same as the width of the heater. The channel length (37 mm) is determined by the heater dimension as well as the capability of the power supply. Other than the dimension of the channel and the heater capability, the test apparatus is the same as the wide channel test apparatus discussed in Chapter 4. The experimental results are, thus, compared with the prediction which was used in Chapter 4. The micro-gap of the channel is controlled by the placement of the Plexiglas top plate, which is the same as the channel width (as in Chapter 4) and used to create three different channel gaps for testing.

5.1 Single Phase Pressure drop

5.1.1 500 µm Gap Channel

The pressure drop of this 10 mm by 37 mm "narrow" channel was measured with the same equipment as used in the experiments described in Chapter 4 to determine the pressure drop for the 31 mm by 34mm "wide" channel. Figure 5.1 shows the result of the pressure drop measurement for the 500 µm high channel and the results of the repeatability experiment on the pressure drop of water flow in that channel. A 7% error bar is added to the results. The deviation of most of experimental results, among the 4 measurements, is less than 7%, which is within the error of the experimental equipment. The pressure drop is seen to increase monotonically with the flow rate and the experimental results are found to be within 7% of the prediction, with Eq. (4.1) and Eq. (4.2), for both water and FC-72. The measured pressure drop of water and FC-72 is up to 14.7 kPa at a flow rate of 10.6 ml/s and 9.9 kPa at a flow rate of 9.5 ml/s. The highest channel Reynolds number of water is 2239 at a flow rate of 9.67 ml/s, the corresponding velocity is 2.02 m/s and mass flux is 2090 kg/m^2-s. The highest channel Reynolds number of FC-72 is 4750 at a flow rate of 9.5 ml/s, the corresponding velocity is 1.9 m/s and mass flux is 3190 kg/m^2-s. The hydrodynamic entry length, $\boldsymbol{x}^+$ which is defined in Eq. (4.3) is 0.07 at a flow rate of 2.3 ml/s for water and 0.04 at a flow rate of 2 ml/s for FC-72. Therefore the flow condition is usually developing laminar flow, with a weak tendency towards developing turbulent flow in the highest FC-72 flow rates. These results for pressure drop in the parallel plate, 500 μm channel serve to verify the accuracy of the experimental apparatus and set the stage for a more extensive single- and two-phase flow thermal transport experiments.

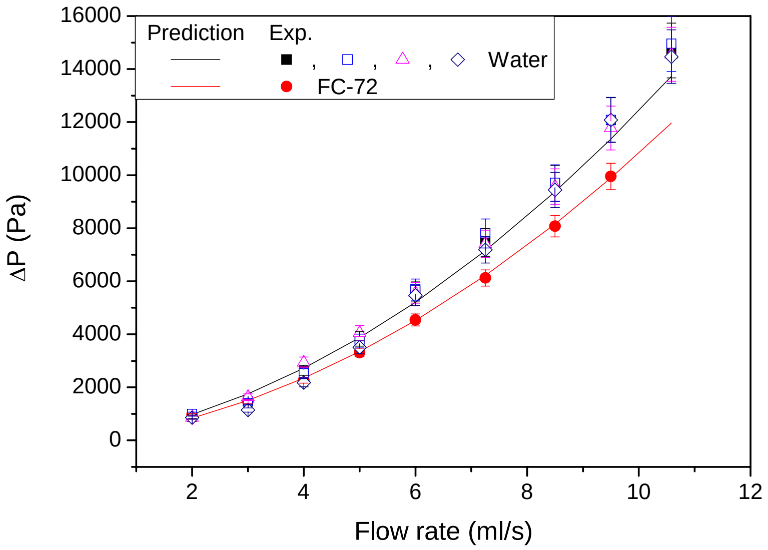

Figure 5.1 Pressure drop for the flow of water and FC-72 in a 500 μm gap channel

5.1.2 210 μm Gap Channel

The measured pressure drop for the 210 μm gap and the predicted pressure drop by Eq. (4.1) are shown in Figure 5.2 for the two working fluids. The measured pressure drop of FC-72 is up to 74.12 kPa at a 9.6 ml/s flow rate and up to 75.84 kPa for a 9.5 ml/s flow rate of water. The channel Reynolds number for this measured data varies with the flow rate from 512.8 to 2117.2 and corresponding velocity, the hydraulic dynamic entry length, x^+, and the mass flux is 1.11 m/s to 4.59 m/s, 0.17 to 0.042 and 1110 kg/m^2-s to 4580 kg/m^2-s for water. For FC-72, the channel Reynolds number varies from 1028.4 to 4884.9 and the corresponding velocity, the hydraulic dynamic entry length, x^+, and the mass flux are 0.952 m/s to 4.52 m/s, 0.08 to 0.018 and 1600 kg/m^2-s to 7600 kg/m^2-s. From these result, it is confirmed that our experiment is in the range of developing or fully developed laminar flow. As shown in Figure 5.2, although the pressure drop for the two fluids is nearly equal, the predicted pressure drop of FC-72 is slightly lower than water at low flow rates. However, at flow rates greater than 3.7ml/s, the pressure drop of FC-72 is predicted to slightly exceed that of water. This crossover is due to the subtle interplay of the lower viscosity and higher density of FC-72 relative to water in the developing flow pressure drop equation, (Eq. 4.2). Interestingly, the measured difference in pressure drop between these two fluids is more modest than indicated by Eq. (4.2). All the experimental results are in the range of the 10% measurement error bar determined for this apparatus.

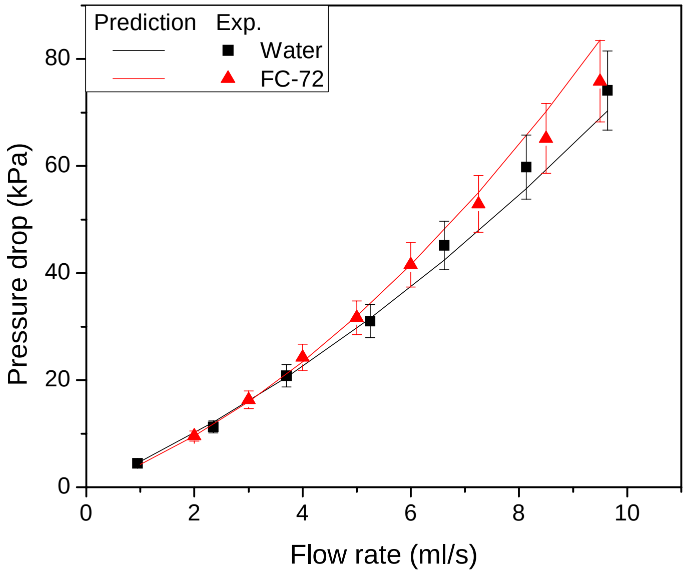

Figure 5.2 Pressure drop for the flow of water and FC-72 in a 210 µm gap channel

5.1.3 110 μm Gap Channel

Figure 5.3 shows the pressure drop measurement result for the 110 μm gap, "narrow" channel. The cross over of the pressure drop between water and FC-72 does not occur at 110 μm gap channel. Due to the limitation of the pump, the highest possible flow rate is 2.3 ml/s and the corresponding measured pressure drop is 82.0 kPa for water and 86.2 kPa at 3.2 ml/s of flow rate for FC-72. The channel Reynolds number for the measured data varies with flow rate from 210.8 to 517.9 and the corresponding velocity, the hydraulic dynamic entry length, $\boldsymbol{x}^+$, and the mass flux are 0.86 m/s to 2.12 m/s, 0.80 to 0.33 and 860 kg/m^2-s to 2120 kg/m^2-s for water. For the FC-72, the channel Reynolds number varies from 432.74 to 1557.8 and corresponding velocity, the hydraulic dynamic entry length, $\boldsymbol{x}^+$, and the mass flux are 0.76 m/s to 2.73 m/s, 0.39 to 0.011 and 1270 kg/m^2-s to 4580 kg/m^2-s. From these result, it is confirmed that our experiment is in the range of developing or fully developed laminar flow. A 5% error bar is drawn in Figure 5.3. These results for pressure drop in the parallel plate, 110 μm channel verify again the accuracy of the experimental apparatus.

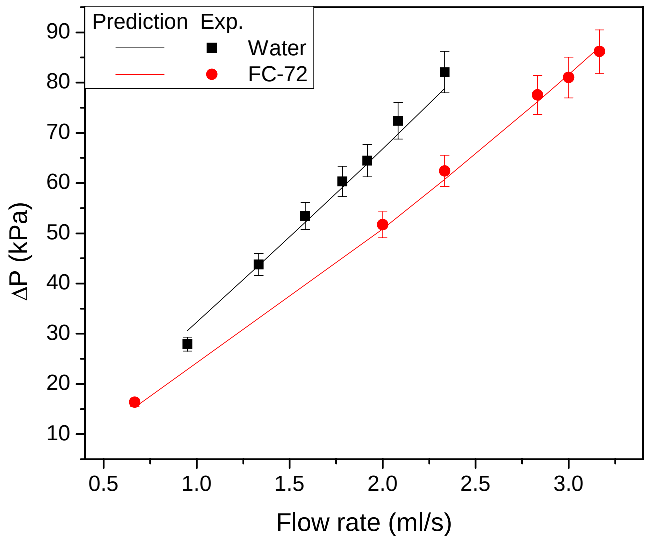

Figure 5.3 Pressure drop for the flow of water and FC-72 in 110 μm gap channel

5.2 Single-phase Heat Transfer

5.2.1 500μm Gap Channel

Single-phase heat transfer experiments with water and FC-72 as the working fluid were performed with the exact same equipment as used for the wide channel experiments and the results were compared with the correlation given in Eq. (4.9). For the single-phase experiment of FC-72, the wall temperature of the copper base plate was controlled to lower than 38˚C in these experiments to avoid the pseudo boiling effect. The measured experimental results are compared with predicted values obtained with the correlation, Eq. (4.8) and (4.9), and the results of the CFD simulation, using the thermo-fluid Computational Fluid Dynamics software product IcePak ver. 4.1 in Figure 5.4.

The heat transfer coefficient is seen to linearly increase with the flow rate for both fluids and reflect a high degree of repeatability. The 5% and 10% error bar is added to the Figure 5.4 and Figure 5.4 (b) and (c) shows the detailed view of repeatability of the water and FC-72 data. The deviation of the different experiments of water is less than 5% and less than 10% for FC-72. The measured average heat transfer coefficient of water is seen to be typically four times larger than that of the FC-72. In particular, the water heat transfer coefficient attains a value of 13.4 kW/m^2-K at a flow rate of 9.7ml/s, the corresponding channel Reynolds number, x^+, mass flux is 2061.89, 0.02, 1930 kg/m^2-s and FC-72 reaches 4.5 kW/ m^2-K at a flow rate of 8.5 ml/s and the corresponding channel Reynols number, x^+, mass flux is 4750, 0.008, 3190 kg/m^2-s. The standard deviation between experimental results and correlation is 5% for water and 9% for FC-72. The CFD result is closer to the experimental result than the correlation. This would appear to be the result of the CFD modeling accurately representing the experimental environment. The error between CFD and experiment is 5% for water and 10% for FC-72. Overall, the correlation and CFD result of water is closer to the experiment than FC-72. This is most likely due to the modest uncertainty of the physical properties of FC-72.

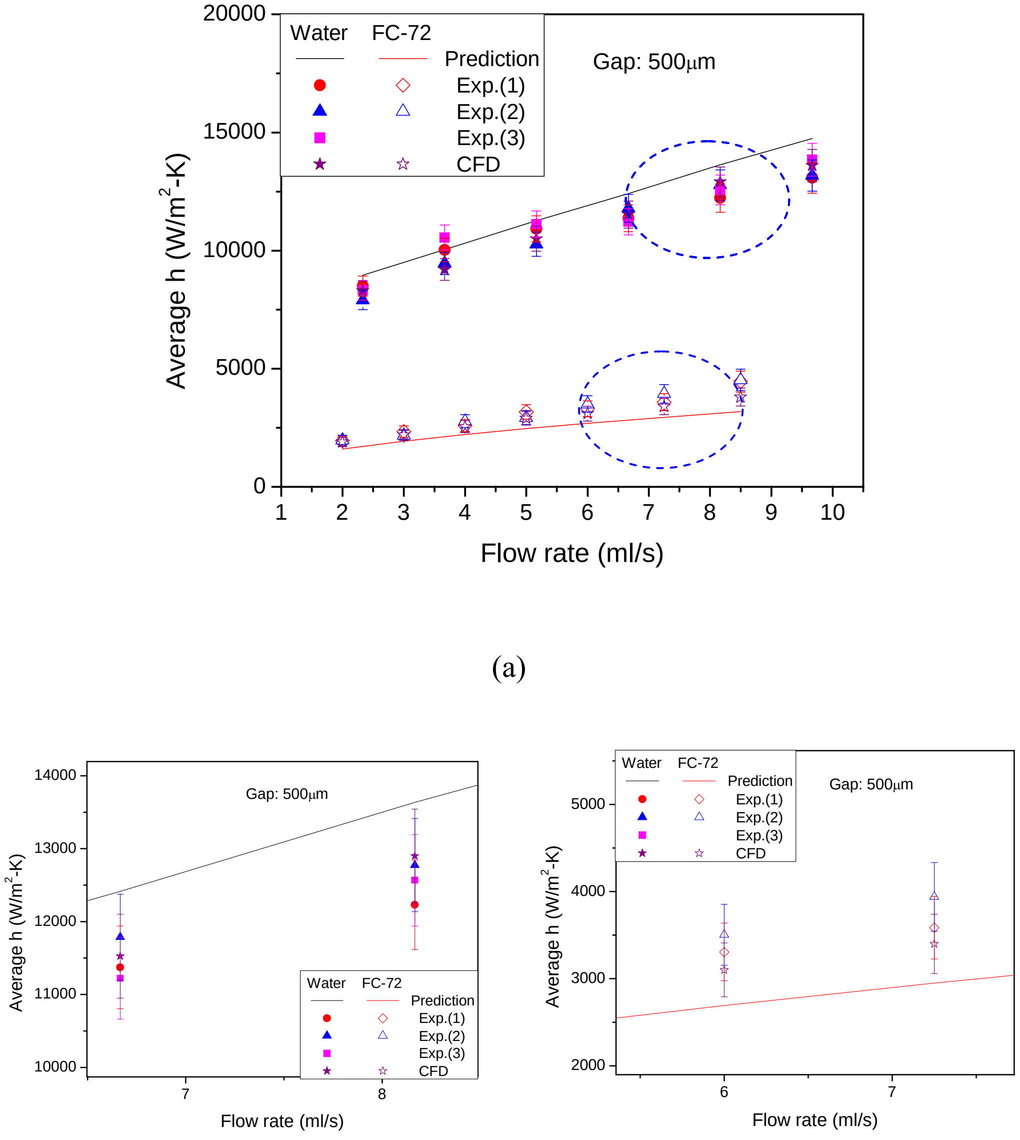

(a)

(b) (c)

Figure 5.4 (a) Single-phase heat transfer coefficients for water and FC-72 flowing in a 500 μm gap channel (b) detail of water and (c) detail of FC-72

5.2.2 210 μm Gap Channel

Figure 5.5 shows the experimental results for the 210 μm gap channel. The heat transfer coefficient linearly increases with flow rate. The measured heat transfer coefficient is up to 24 kW/m^2-K at 8.2 ml/s of flow rate for water. The corresponding channel Reynolds number, x^+, mass flux are 1794.83, 0.05 and 3890 kg/m^2-s. For FC-72, at flow rate of 8.5 ml/s, a heat transfer coefficient of 5.4 kW/m^2-K is achieved and the corresponding channel Reynolds number, x^+, mass flux are 4370.7, 0.02 and 6800 kg/m^2-s. A 10% error bar is drawn in Figure 5.5 and most of the experiment data are seen to fall in the range of the anticipated error. The cooling capability of FC-72 is again seen to be approximately 25% of water at the same volumetric flow rate.

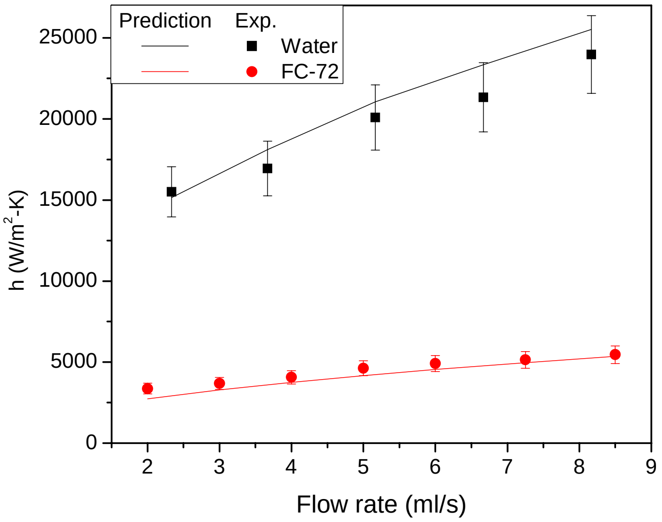

Figure 5.5 Single-phase heat transfer coefficients for water and FC-72 flowing in a 210 µm gap channel

5.2.3 110 µm Gap Channel

Figure 5.6 shows the average heat transfer coefficient resulting from the single-phase flow of FC-72 in the “narrow” 110 µm mcirogap channel. The area-averaged heat transfer coefficient of the 110 µm experiments is up to 5 kW/m^2-K at 3 ml/s of flow rate. The corresponding channel Reynolds number, x^+, and mass flux are 1557, 0.1 and 4580 kg/m^2-s, indicating that fully developed flow is attained at the channel exit. The 10% error bar is drawn in Figure 5.6. The experimental results are seen to be on the edge of 10% error from the predicted value. Due to the high pressure drop, this is the highest flow rate which could be achieved in the experimental apparatus with the current pump.

In this experimental series it was determined that, unfortunately, water could not be used as a coolant in the 110 μm gap channel. Due to the high viscosity and surface tension (72 dynes/cm^2) of water, which is 6 times greater than FC-72, air bubbles became trapped in the channel gap, blocking the channel and making it impossible for the water to fully wet the channel wall. This resulted in an increase in the wall temperature and a lower average heat transfer coefficient for the 110 μm channel than for the 210 μm gap channel. Due to the effect of such trapped air bubbles and their interaction with heater surface roughness, no experiments were performed with water flowing in microgap channels smaller than 210 μm.

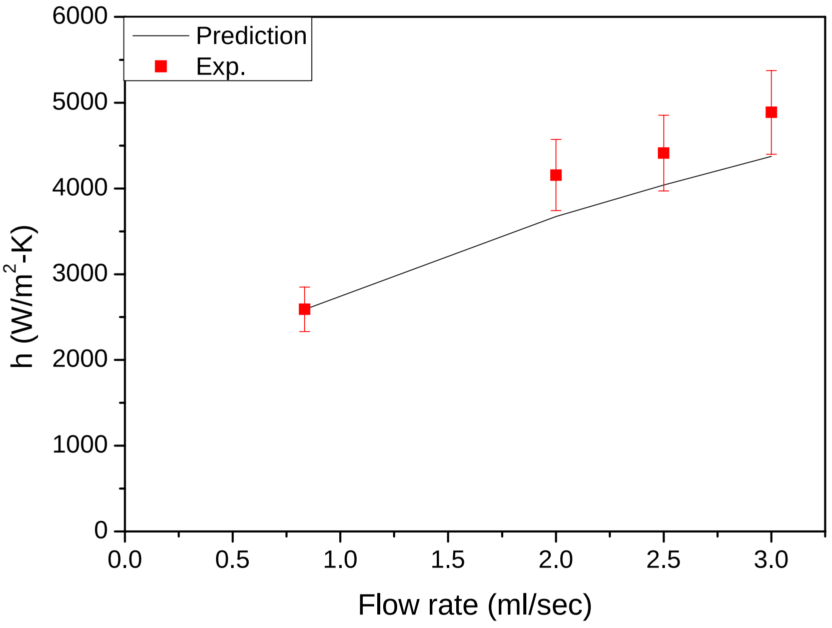

Figure 5.6 Single-phase heat transfer coefficients for FC-72 flowing in 110 µm gap channel

5.2.4 Channel Gap Effect

Combining the previous thermal transport results in this section, Figure 5.7 shows the channel gap effect on the single phase cooling capability of water and FC-72. For the case of water as the coolant, when the channel gap decreases from 500 µm to 210 µm, the heat transfer coefficient increases 85% over the full flow rate range and for FC-72, it increases 70%. For FC-72, a further decrease in the channel gap from 210 µm to 110 µm, increases the heat transfer coefficient by an additional 25%.

The combination of smaller channel volume and higher heat transfer coefficients in the narrow gap channels, leads to a dramatic increase in the volumetric heat transfer coefficient which can be expressed by Eq. (5.1).

$$h_v = \frac{q''}{H \cdot \Delta T} \tag{5.1}$$

where q'' is dissipated heat flux, H is channel gap and ΔT is temperature difference between channel and coolant.

For the case of water as a coolant, the volumetric heat transfer coefficient of 210 μm gap becomes 4 times greater than that of 500 μm at low flow rate and it becomes greater as the flow rate increases. For the FC-72, decreasing the channel gap from 500 μm to 210 μm increases the volumetric heat transfer coefficient 4 times and it becomes 2.5 times greater again as the channel gap decreases from 210 μm to 110 μm, for an overall 10-fold improvement in the volumetric heat transfer coefficient.

Thus, as seen in Figure 5.8, a decreased channel gap is a highly efficient way to provide aggressive thermal management, even when restricting the application to single-phase flow.

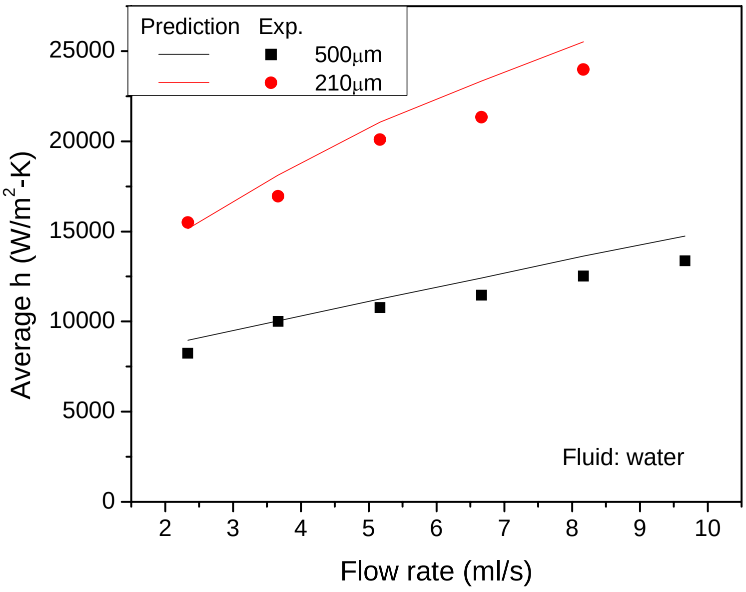

(a)

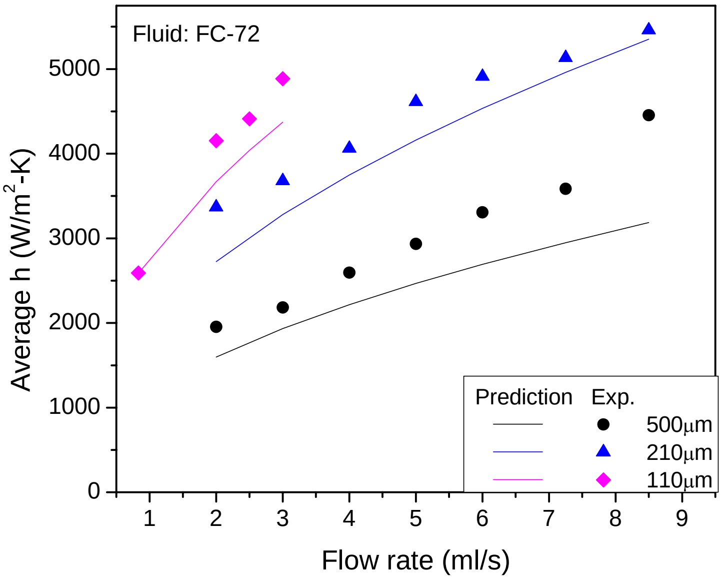

(b)

Figure 5.7 Channel gap effect on single-phase heat transfer coefficients for the flow of (a) water and (b) FC-72 in a microgap channel

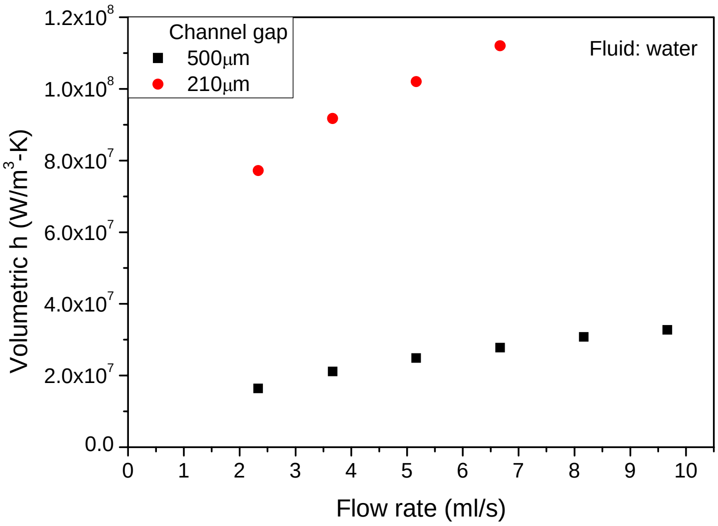

(a)

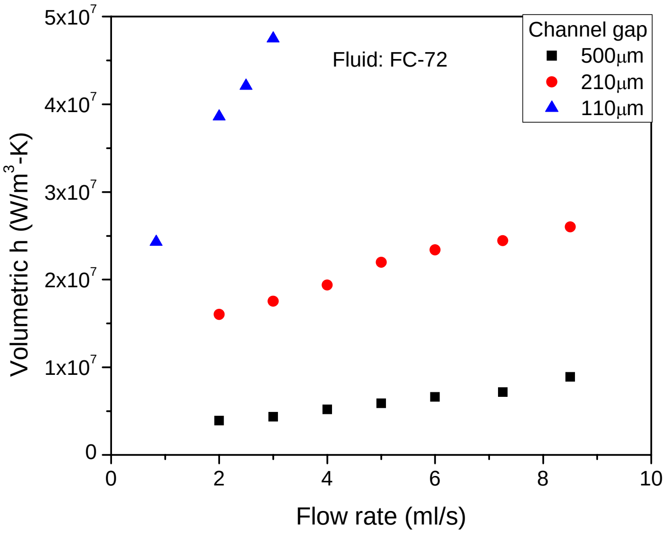

(b)

Figure 5.8 Channel gap effect on the single-phase volumetric heat transfer coefficients for (a) water and (b) FC-72 flowing in a micro-gap channel

However, the decreased channel gap substantially increases the pressure drop for flow across each microchannel, as is shown in Figure 5.9. The pressure drop increases greatly with decreasing channel gap and increasing flow rate. To better appreciate the efficiency of single-phase cooling in microgap channels, it is instructive to relate the observed heat transfer capability to the required pumping power obtained by multiplying the volumetric flow rate and the pressure drop, to find the Coefficient of Performance of each channel as a function of flow rate.

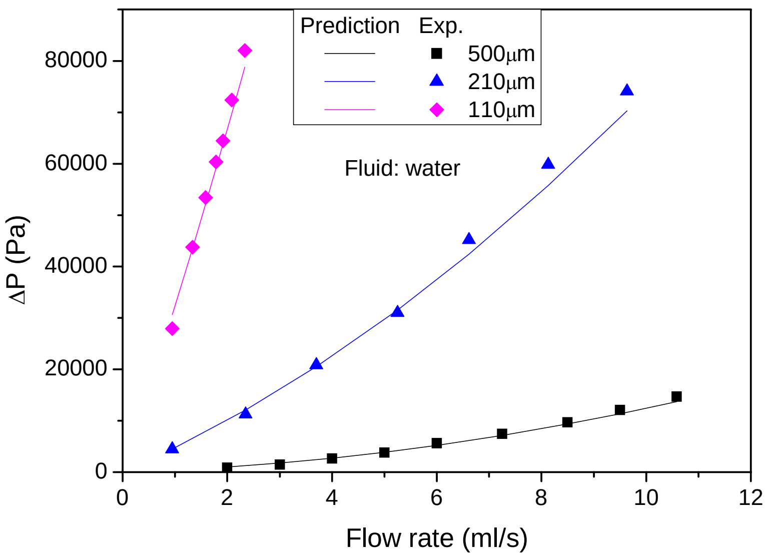

(a)

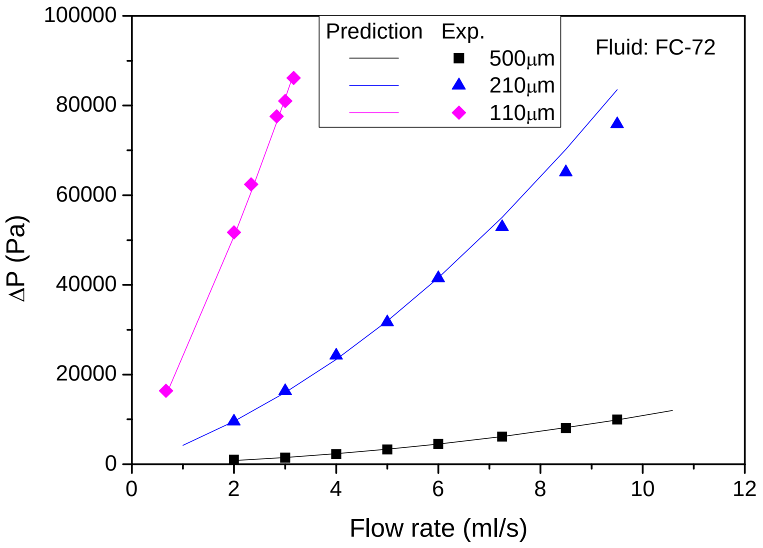

(b)

Figure 5.9 Channel gap effect on single-phase pressure drop of (a) water and (b) FC-72 flowing a microgap channel

Figure 5.10 shows the calculated COP's of each channel as a function of flow rate. As expected, large gap channel reveal higher COP at the same flow rate, due to the low pressure drop. This is more distinct at low flow rates. As the flow rate increases, the COP exponentially decreases. Overall, water shows higher COP than FC-72. However, it is encouraging that at a flow rate of 2 ml/s, with only 1W of pumping power, a 500 μm microgap channel can dissipate 2330W, a relatively high heat transfer rate for FC-72.

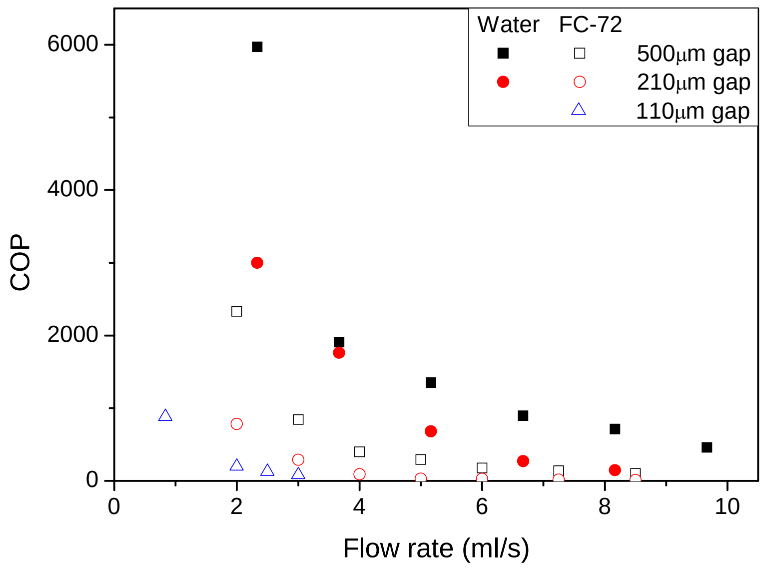

Figure 5.10 COP of water and FC-72 in a microgap channel

5.3 Two-phase

5.3.1 Pool Boiling

Figure 5.11 shows the pool boiling curve of the heater surface in our current experimental set-up. The heater attached copper base block was immersed into the fluid of FC-72 and the heat flux increased. The saturation temperature was set as 56°C which was the boiling temperature of FC-72 at 1 atm. The boiling curve can be separated into two-regimes, one is natural convection, which occurred until slightly above the saturation temperature, and the other regime which occurred after the natural convection regime. The critical heat flux of this experiment was 37.5 W/cm^2.

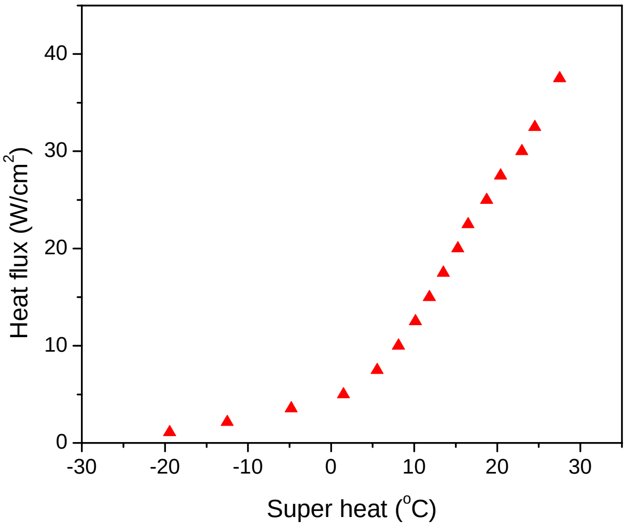

Figure 5.11 Boiling curve of our experimental set-up

5.3.2 Flow Boiling

The two-phase flow boiling experiment was performed with mass flux varying from 56 kg/m^2-s to 1270 kg/m^2-s and at an input power of up to 25W. The subcooled liquid was supplied, as previously described, from the pump to the microgap, parallel plate channel.

Due to the interaction between conduction in the copper heater plate and the heat transfer coefficient in the channel, the actual heat flux into the fluid can vary with the gap dimension and internal flow structure. In addition, the dimension of the copper base block is bigger than the heater due to the flow port and O-ring space for the purpose of sealing. Figure 5.12 shows the schematic diagram of the heater attached copper base block.

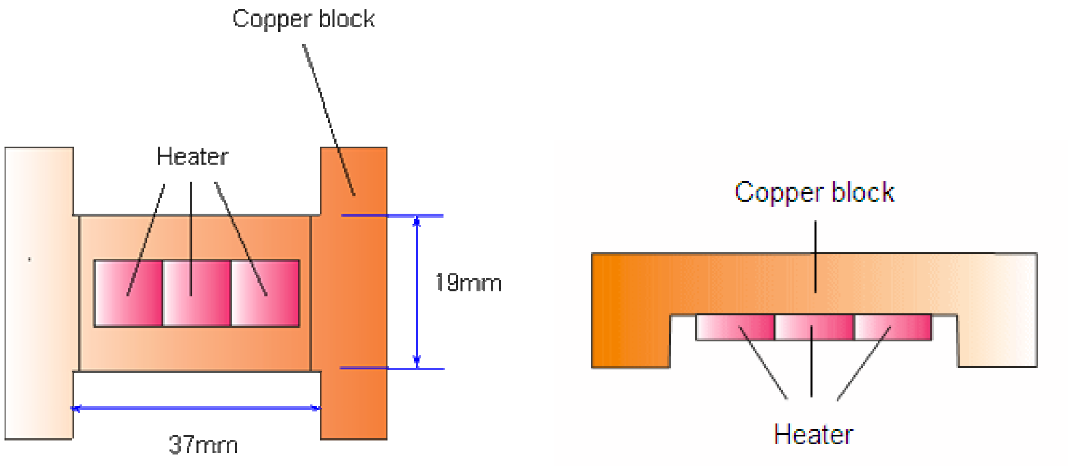

(a) (b)

Figure 5.12 Schematic diagram of heater attached copper base block (a) rear view and (b) side view

Thus, it was found earlier through the use of the CFD software, Icepak ver. 4.1, that the conversion efficiency, i.e. the fraction of heater power transferred to the fluid, in the single-phase experiments was 60% for 500 μm, 68% for 210 μm and 84% for the 110 μm gap channel. Therefore, even though the same power is applied to the heaters, the real heat flux into the channel varied according to the channel gap, yielding very good agreement with the measured and analytically determined heat transfer coefficients. Consequently, an "inverse" computational technique was used to determine the two-phase heat transfer coefficient in the microgap channel. Figure 5.13 (a) shows the axial temperature profile found from the experimental measurements and the CFD inverse computation and (b) shows the inverse CFD heat flux calculation profile for a 210 μm gap.

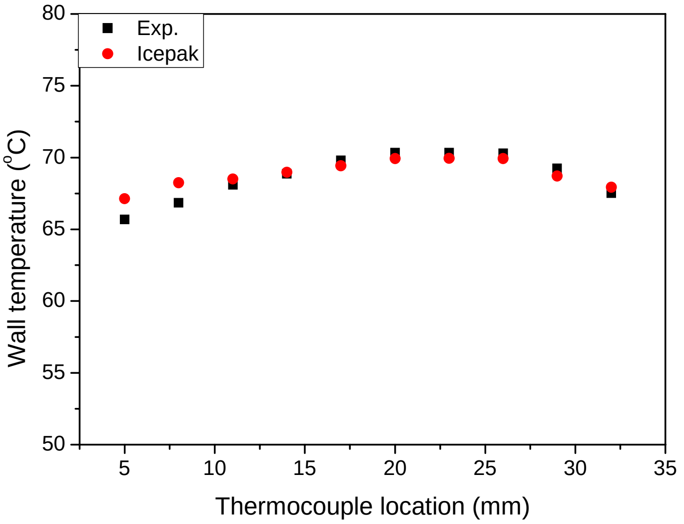

(a)

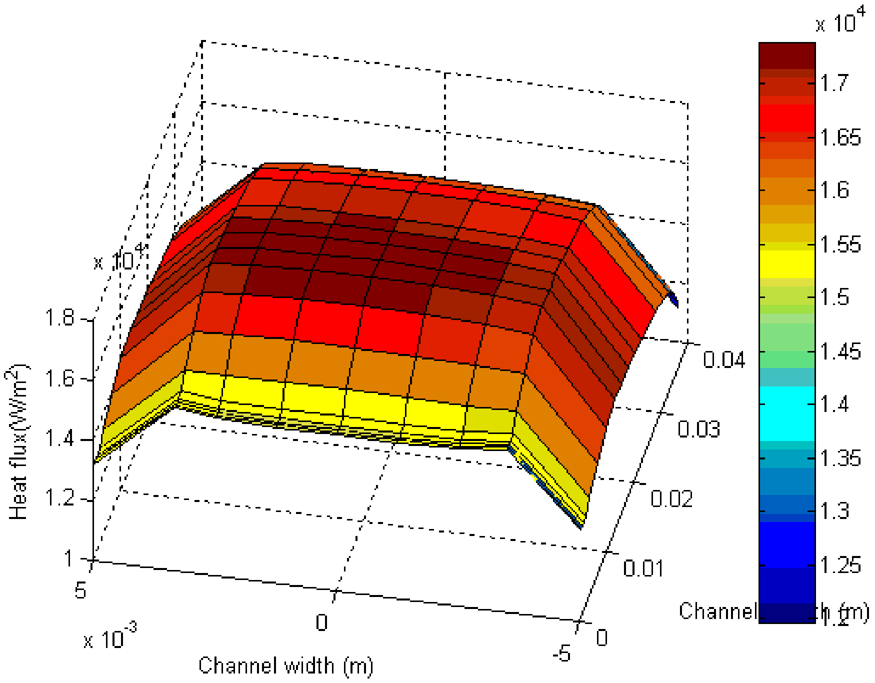

(b)

Figure 5.13 Inversely calculated result (a) wall temperature comparison between experiment and CFD inverse calculation and (b) heat flux 3D profile of 210 μm channel

As shown in Figure 5.13 (a) the experimental axial temperature profile and the inversely calculated CFD profile are very close. The wall temperature deviation between the experiment and CFD is only 0.5°C or less. The inversely calculated average heat flux was 15.5 kW/m^2, which was 14% greater than the heat flux (13.5 kW/m^2) from the single-phase energy balance calculation. The heat flux of side edges, front and ending edges are lower than the center of the channel due to the fact that the dimension of the copper base block is bigger than the heater array. As a result, some heat can be lost to the edges by conduction. Therefore, lengthwise, the heat flux of the channel beginning and endpoint is lower and is 91% of the maximum heat flux. In addition, the side of the channel has a lower heat flux, reached at 80% of the maximum heat flux.

5.32.1 500 μm Gap Channel

The test results of 500 μm gap two-phase heat transfer experiment are shown in Figure 5.14. The test conditions involved changing the mass flux from 55 kg/m^2-s to 280 kg/m^2-s by steps of 55 kg/m^2-s and the corresponding inlet fluid velocities were 0.033, 0.067, 0.1, 0.133, 0.167 m/s. As may be seen in Figure 5.14 (a), for each mass flux, the average heat transfer coefficient increases with heat flux, peaking at values as high as 7500 W/m^2-K, until a value is reached at which the heat transfer coefficient decreases. This variation is thought to reflect the change from subcooled to saturated flow boiling, followed by the onset of local dry out.

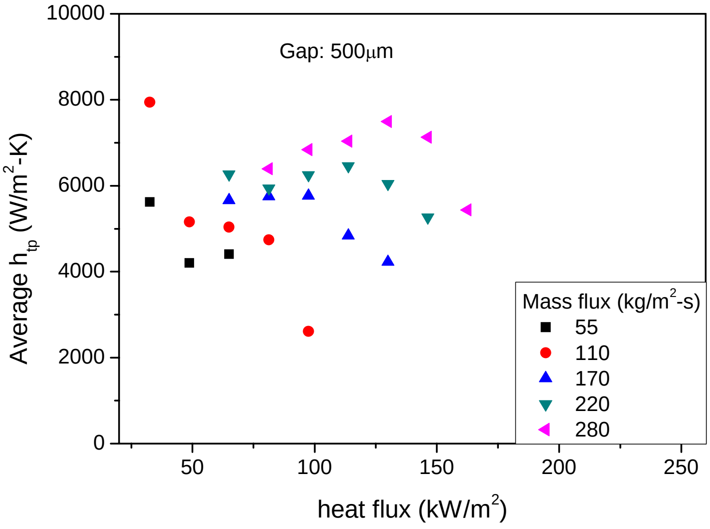

(a)

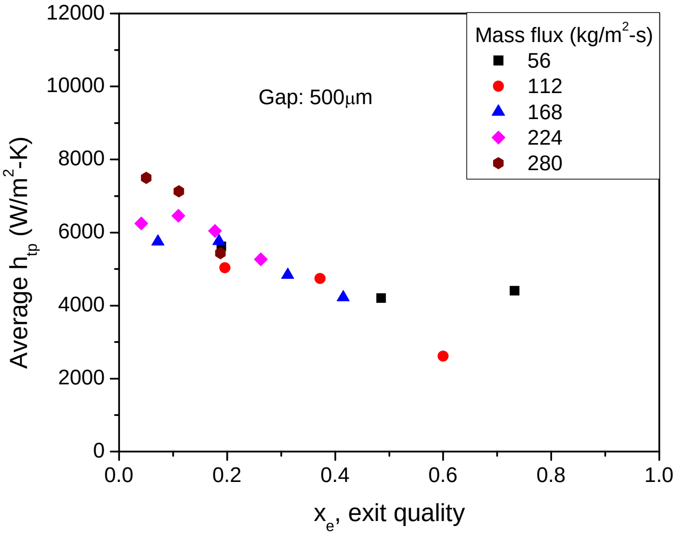

(b)

Figure 5.14 (a) Average heat transfer coefficient vs. heat flux and (b) Average heat transfer coefficient vs. exit quality

The variation of the average heat transfer coefficient with the exit quality in the microgap channel is shown in Figure 5.14 (b). Although to the first approximation the heat transfer coefficient appears to vary nearly linearly with exit quality from 0.1 to 0.6, on closer look some subtle changes in slope may be seen to appear at a distinct quality for each mass flux. To help interpret this functional dependence, it is convenient to project the axial variation of the heat transfer coefficient onto a flow regime map. Under a constant heat flux boundary condition, the quality increases in the flow direction and, as shown in Figure 5.15 using the Taitel-Dukler mapping methodology [31] for a channel with a 0.95 mm hydraulic diameter, subjected to a heat flux of 48.75 kW/m^2 and a mass flux of 55 kg/m^2-s, the liquid-vapor mixture is found to progress from the intermittent-slug flow regime to the annular flow regime. In this figure, the experimental heat transfer coefficient values are shown as a function of superficial vapor velocity (easily translatable to quality) together with the previously discussed two-phase heat transfer correlations developed by Chen and Shah, respectively.

As shown in the Figure 5.15, the experimental data in the Intermittent flow regime is relatively close to the Shah correlation. However, as the quality increases, the data shifts into the Annular regime and the heat transfer coefficients move closer to the Chen correlation.

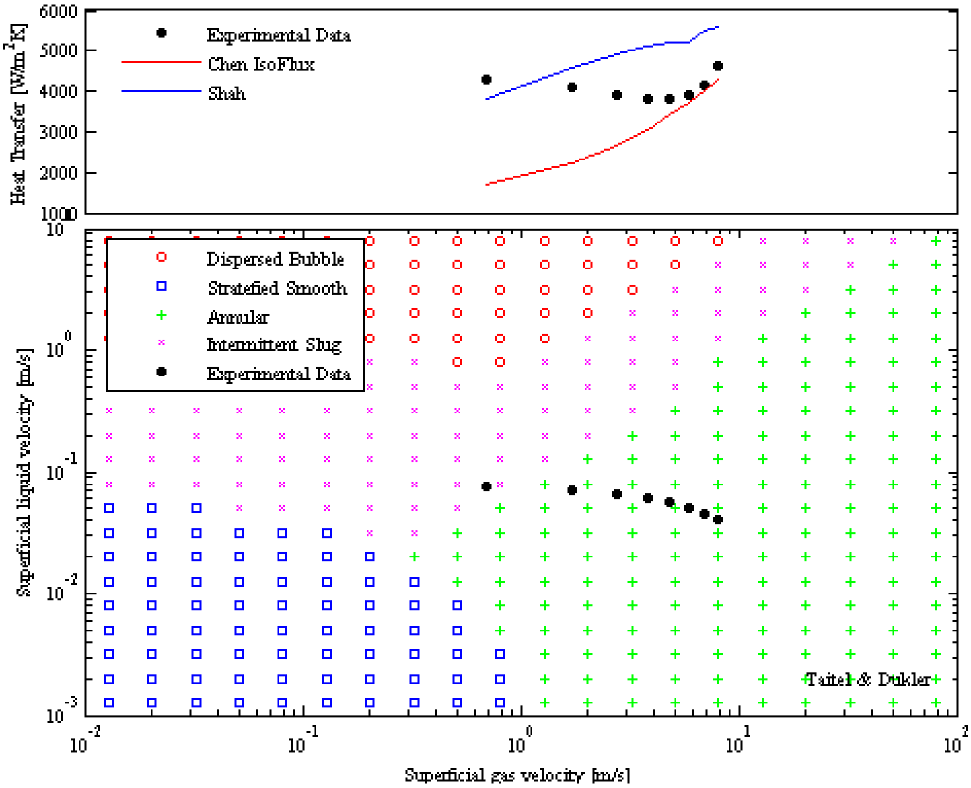

Figure 5.15 Projected experimental result to the flow regime map, $q'' = 48.75 kW / m^2$, $G = 55 kg/m^2 - s$, $D_h = 0.952 mm$

Figure 5.16, displaying flow regime maps and heat transfer coefficients for progressively higher heat fluxes in a fixed diameter and mass flux microgap channel, shows this movement of data with more clarity. As the heat flux increases, the quality increased and the experimental data moved away from the Intermittent regime towards the Annular regime and away from the values predicted by the Shah correlation to those predicted by the Chen correlation.

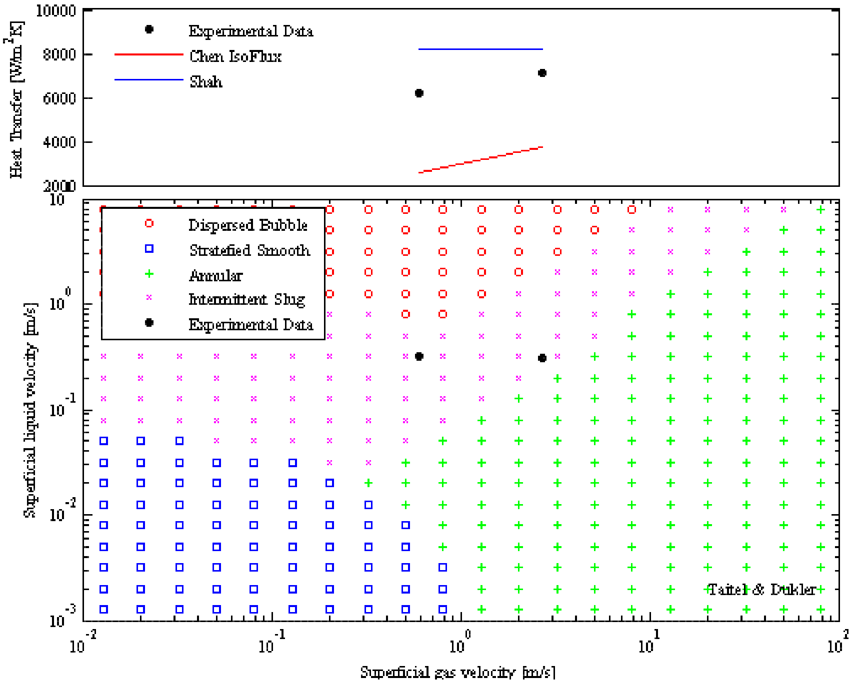
10000
8000
6000
4000
2000
Heat Transfer [W/m^{2}K]
Experimental Data
Chen IsoFlux
Shah
10
10^0
10^{-1}
10^{-2}
10^{-3}
Superficial liquid velocity [m/s]
Dispersed Bubble
Stratefied Smooth
Annular
Intermittent Slug
Experimental Data
Taitel & Dukler
10^{-2}
10^{-1}
10^0
10^1
10^2
Superficial gas velocity [m/s]

(a)

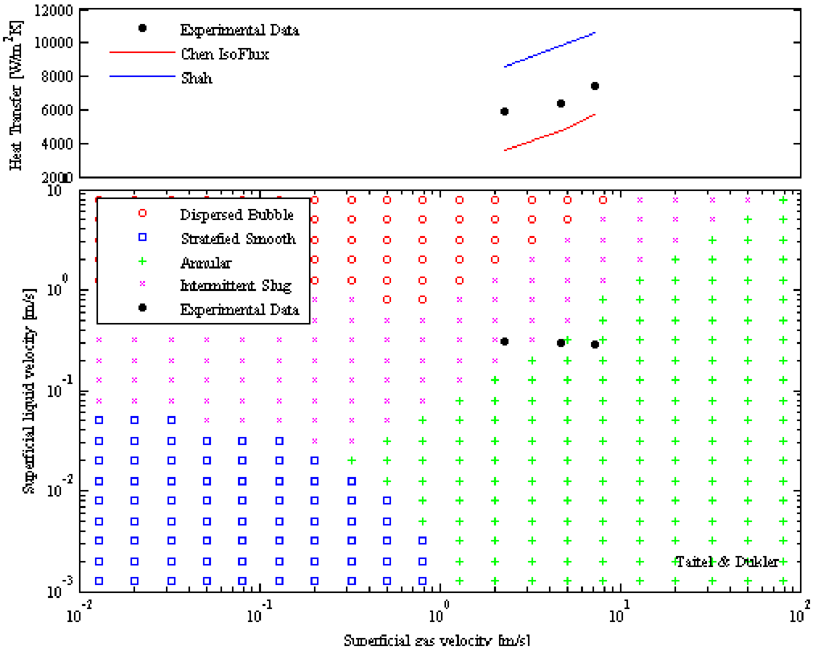
12000
10000
8000
6000
4000
2000
Heat Transfer [W/m^{2}K]
Experimental Data
Chen IsoFlux
Shah
10
10^0
10^{-1}
10^{-2}
10^{-3}
Superficial liquid velocity [m/s]
Dispersed Bubble
Stratefied Smooth
Annular
Intermittent Slug
Experimental Data
Taitel & Dukler
10^{-2}
10^{-1}
10^0
10^1
10^2
Superficial gas velocity [m/s]

(b)

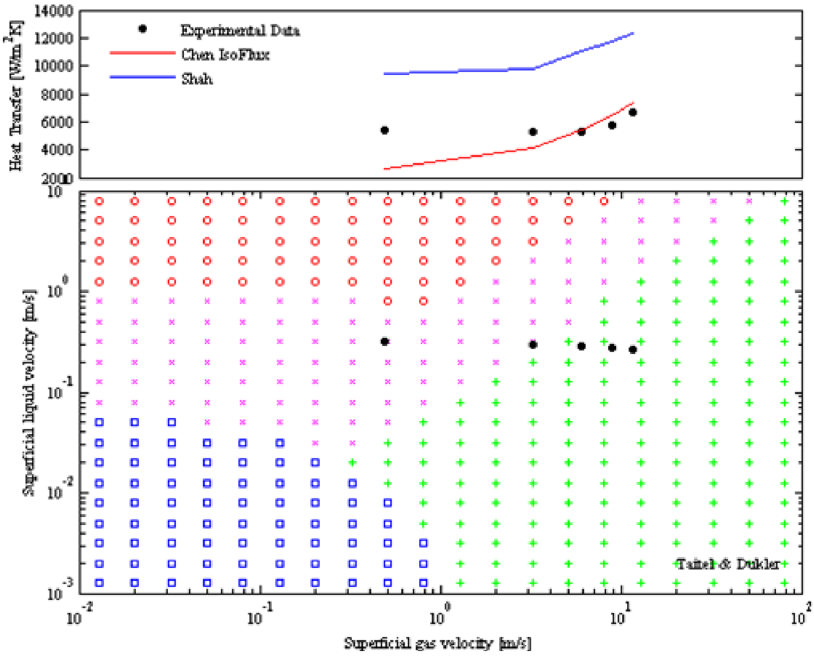

(c)

Figure 5.16 The projected test result. The test condition of G=280kg/m^2-s, D$_h$ = 0.952mm (a) heat flux $q'' = 97.5kW/m^2$ (b) heat flux $q'' = 113.8kW/m^2$ and (c) heat flux $q'' = 130.0kW/m^2$

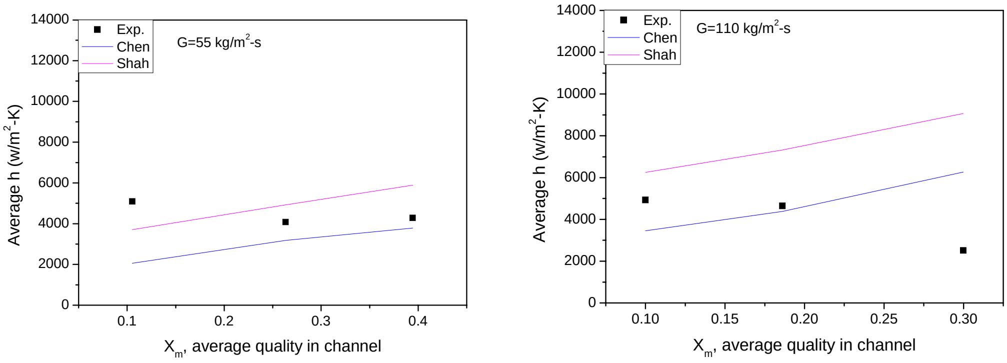

(a) (b)

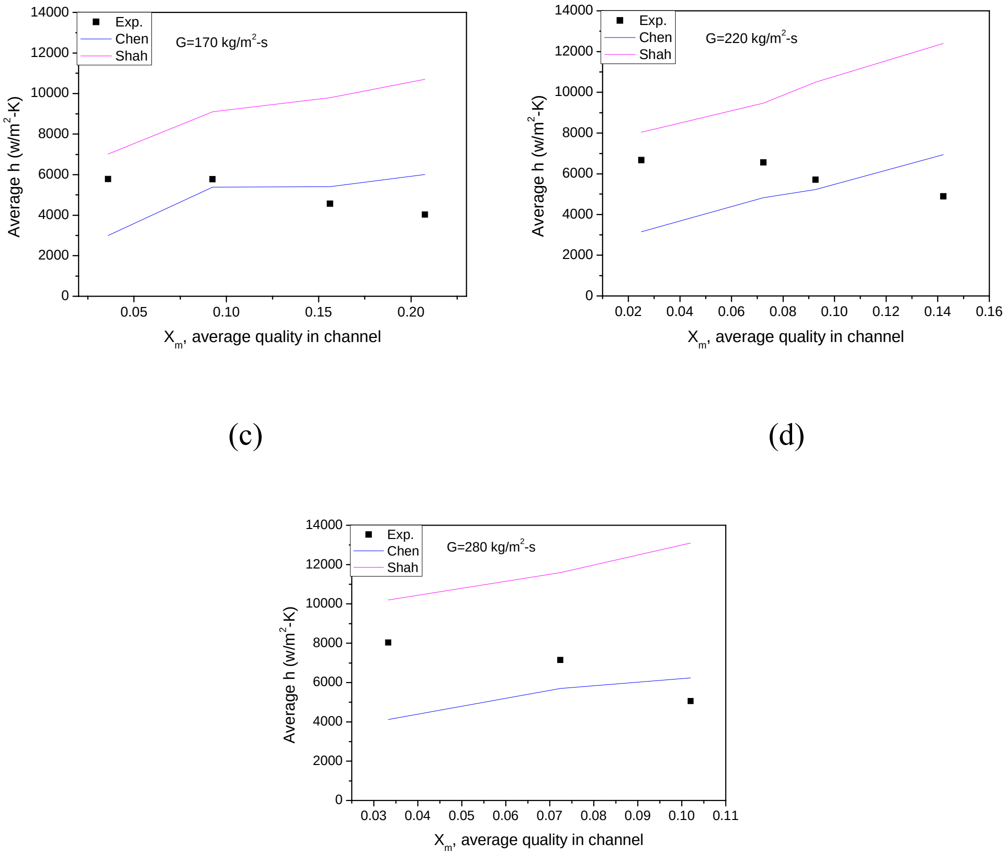

(c) (d)

(e)

Figure 5.17 Comparison of the experimental result with Chen's and Shah's correlation which was calculated using average quality

Figure 5.17 is the result of comparison of the experimental heat transfer coefficients with the Chen and Shah correlations, respectively, calculated based on the average quality of the channel. The comparison is done at the same mass flux with increasing heat flux. At low quality the experimental result is close to Shah's correlation. However, as quality increases the experiment result moves away from the values given by Shah's correlation and toward the predictions of the Chen correlation. The closest error of the experimental result is with 10% of the correlations. Figure 5.17 (a) shows this comparison for a mass flux 56 kg/m^2-s. At low quality, the test result is close to Shah's correlation, with a discrepancy of 25%. The next data point is exactly in the middle of the Shah correlation and Chen correlation with an error margin of 20%. The last data point is close to Chen's correlation with an error margin of 10%. Figure 5.17 (b) is result of the mass flux 110 kg/m^2-s. The first data point is in the middle of Shah's and Chen's correlations. As the quality increases, the data moves closer to Chen's correlation, with an error of 5%. At mass flux 170 kg/m^2-s, which is shown in Figure 5.17 (c), the first data point is close to Shah's correlation with an error of 17%. The next two points are close to Chen's correlation with an error of 3% and 15%. For the conditions of Figure 5.17 (d), the first heat transfer coefficient value is close to that predicted by Shah's correlation and the error is 15%. The second point is in the middle of Shah's correlation and Chen's correlation. The error is 34% of Shah's correlation and 30% of Chen's correlation. The third data point is close to Chen's correlation and the error is 8%. Figure 5.17 (e) shows the experimental results for a mass flux of 280 kg/m^2-K. The first data point is close to Shah's correlation and the error of Shah's correlation is 20% and Chen's correlation is 50%. The next two data is close to Chen's correlation and the error is 20%. From this detailed comparison, it is noteworthy that the reported experimental values of microgap heat transfer coefficients are well bounded by the Shah correlation, reflecting the character of the Intermittent flow regime and the Chen correlation representing the thermal transport behavior of the Annular flow regime.

5.3.2.2 210 μm Gap Channel

The test results for the 210 μm gap two-phase heat transfer experiment are shown in Figure 5.18. In these experiments the mass flux was changed from 130 kg/m^2-s to 660 kg/m^2-s in steps of 130 kg/m^2-s and the corresponding inlet fluid velocity was 0.0794, 0.159, 0.238, 0.317, 0.397 m/s. The average heat transfer coefficient was found to generally display a parabolic variation with the heat flux, increasing towards a peak value as the channel condition changed from subcooled to saturated flow boiling and then decreasing with further increases of heat flux.

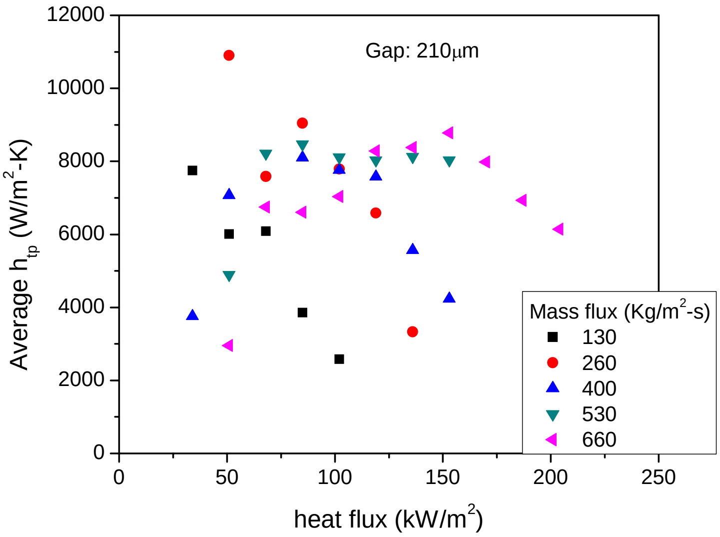

Figure 5.18 Average heat transfer coefficient vs. heat flux

As previously used in the analysis of the 500 μm channel, Figure 5.19 shows the flow regime map with projected experimental result and correlations. Similarly to the 500 μm gap channel, the experimental data in the Intermittent regime is matched with the Shah's correlation. The experimental data moves away from the Intermittent regime toward the Annular regime as the heat flux increases. Then the experimental data moves away from the Shah's correlation and moves toward Chen's correlation.

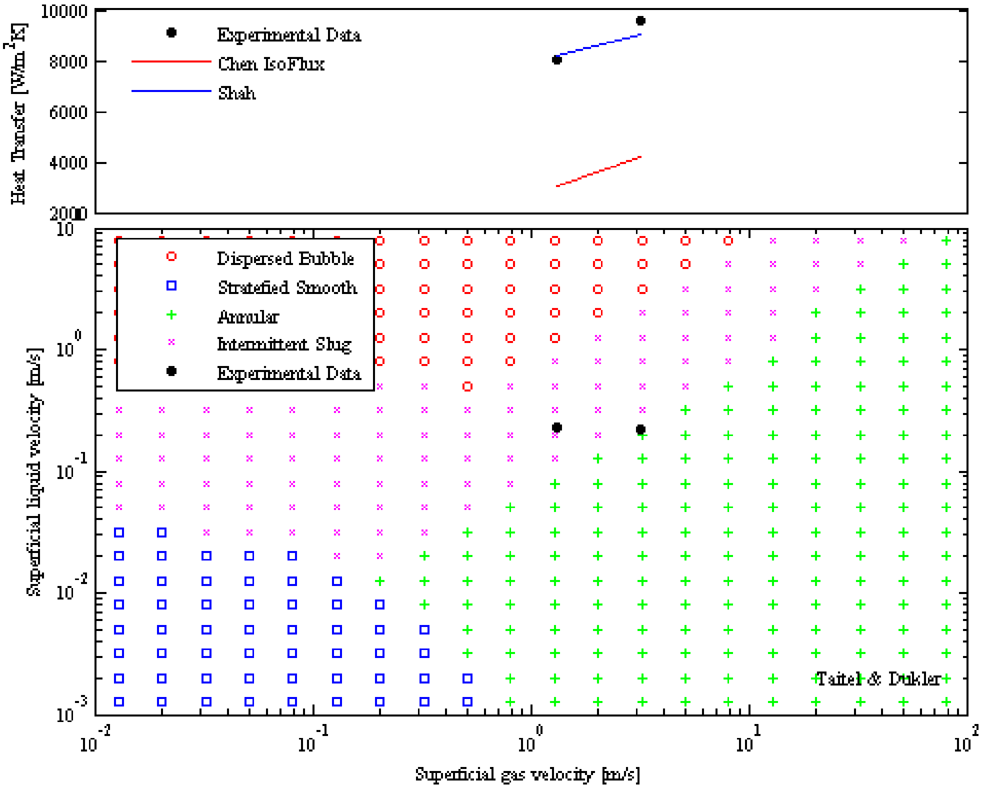

(a)

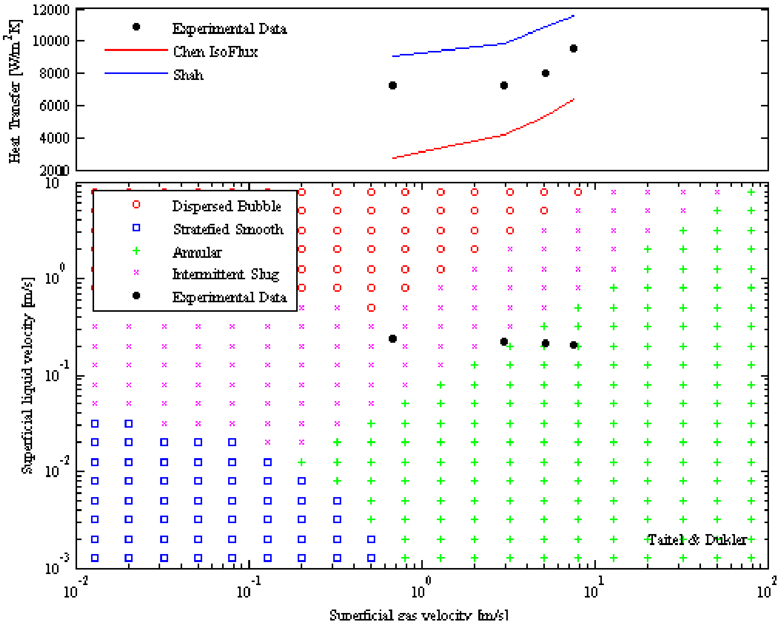

(b)

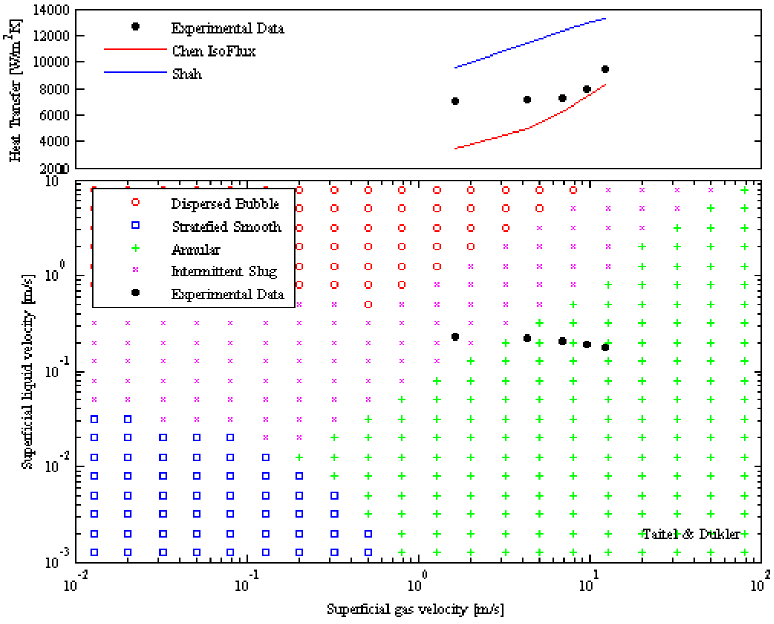

(c)

Figure 5.19 The projected test result of 210 μm gap channel. The test condition of G=300.0 kg/m^2-s, D$_h$ = 0.411 mm (a) heat flux $q''=85kW/m^2$ (b) heat flux $q''=102kW/m^2$ and (c) heat flux $q''=119kW/m^2$

Figure 5.20 is the result of comparison of the experimental result with Chen's and Shah's correlation which was calculated based on the average quality in the channel. The comparison is done at the same mass flux with increasing heat flux. In the same manner as the 500 μm gap channel, the experimental result of low quality is close to Shah's correlation. However, as quality increases the experimental results approach the Chen's correlation and away from Shah's correlation. From this comparison, it is noteworthy that channel averaged experimental results for the 210 μm gap channel are also generally bounded by Shah's and Chen's correlation. The values of the heat transfer coefficient that fall below the Chen correlation, especially at the higher qualities, may signify the occurrence of local dry out.

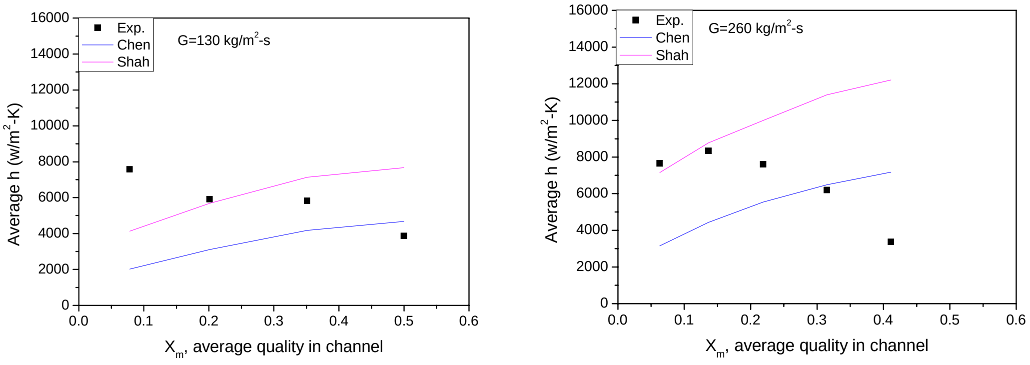

(a) (b)

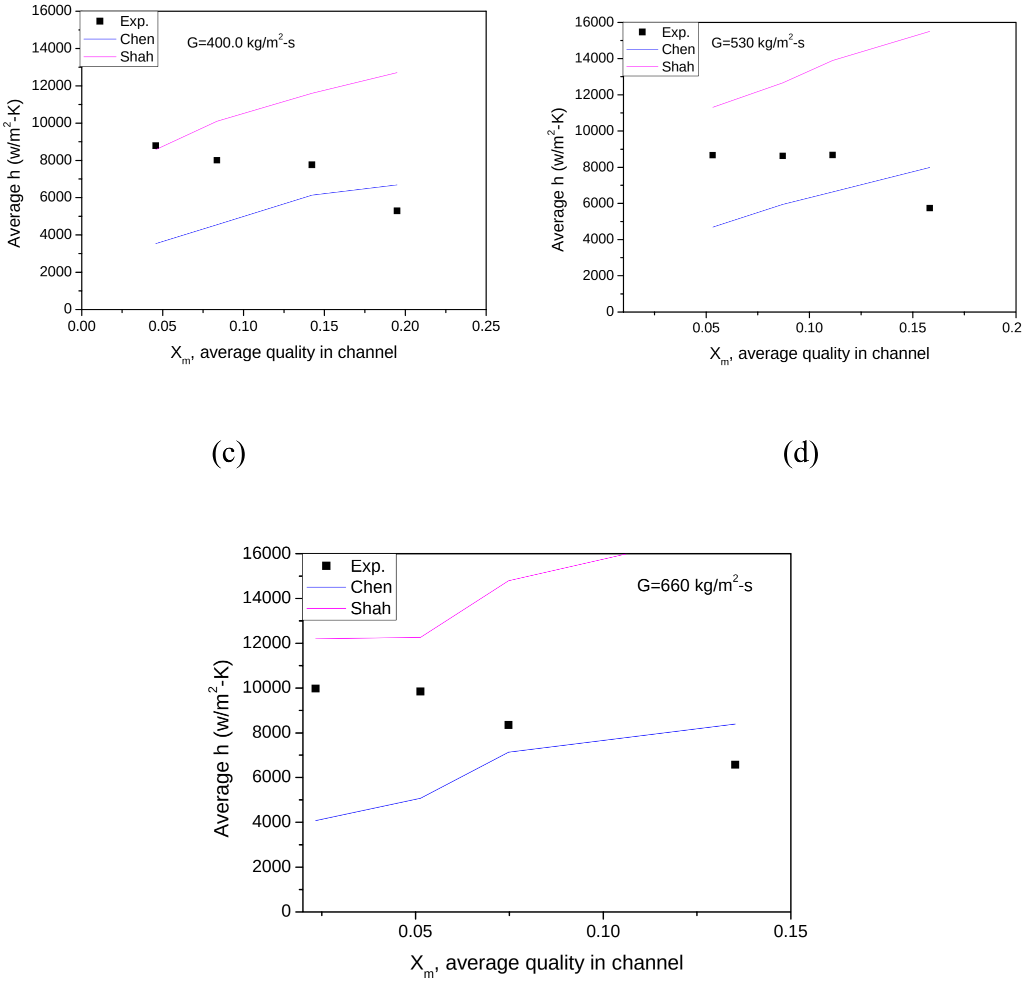

(c) (d)

(e)

Figure 5.20 Comparison of the experimental result with Chen's and Shah's correlation which was calculated using channel medium quality

In order to confirm the repeatability of the two-phase experiments, two different mass fluxes with several heat fluxes were repeated under the same condition. Figure 5.21 shows the experimental result of repeatability. Figure 5.21 (a) is for the mass flux of 530 kg/m^2-s with two different heat fluxes of 11.9 W/cm^2 and 13.6 W/cm^2. Figure 5.21 (b) is for the mass flux of 660 kg/m^2-s with three different heat fluxes of 11.9 W/cm^2, 13.6 W/cm^2 and 18.7 W/cm^2. The temperature of the wall, liquid inlet and outlet, pressure drop, and absolute pressure at the outlet were measured to determine the quality of the channel, saturation temperature, and two-phase heat transfer coefficient. The deviation of the experimental result along the full channel length was less than 10%, thus falling within the experimental error range.

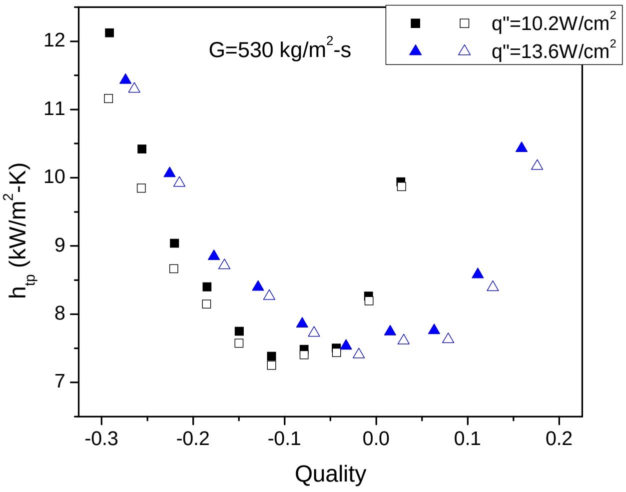

(a)

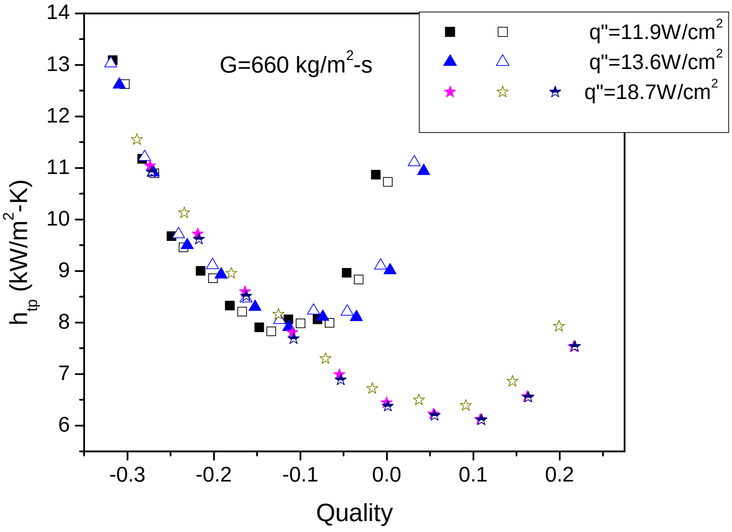

(b)

Figure 5.21 Repeatability of the two-phase experiment of 210 μm gap channel with various heat flux (a) mass flux of 530 kg/m^2-s (b) mass flux of 660 kg/m^2-s

5.3.2.3 110 μm Gap Channel

There is nearly no existing data in the literature for channels that have less than a 210 μm gap. It is thus most rewarding to note that the 110 μm gap channel shows some similarities to the heat transfer coefficient variation observed in the 210 μm gap and 500 μm gap channels, but - as shown in Figure 5.22 –, it appears to possess only the down-sloping branch of the previously observed parabolic trend. The heat transfer coefficient decreases with the increase of the heat flux. The heat transfer coefficient of 110 μm gap channel is higher than the 210 μm gap or the 500 μm gap channels. The heat transfer coefficient of two-phase is much higher than single-phase FC-72 and close to the single-phase of water at the same flow rate.

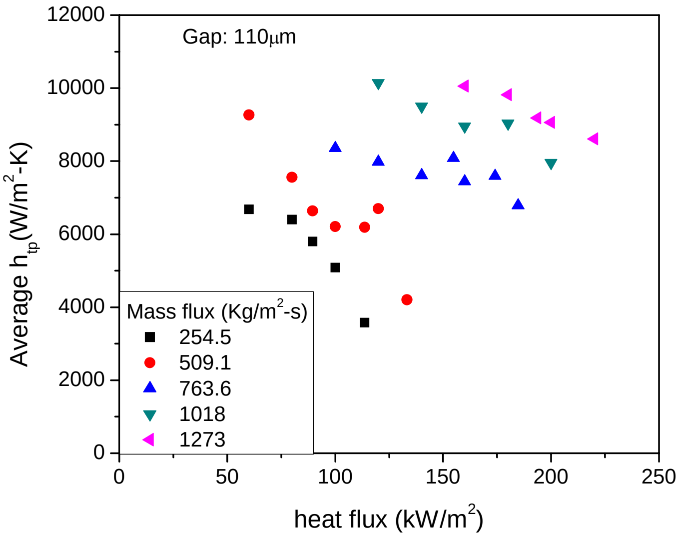

Figure 5.22 Average heat transfer coefficient vs. heat flux

It should be noted that for the 110 μm gap channel, when the boiling starts, local dry out was seen to occur at the exit of the channel, occupying around 20~25% of the area and decreasing when a flow boiling become established. Figure 5.23 shows the changing of dry out area at the beginning of the boiling and sometime later after the boiling started.

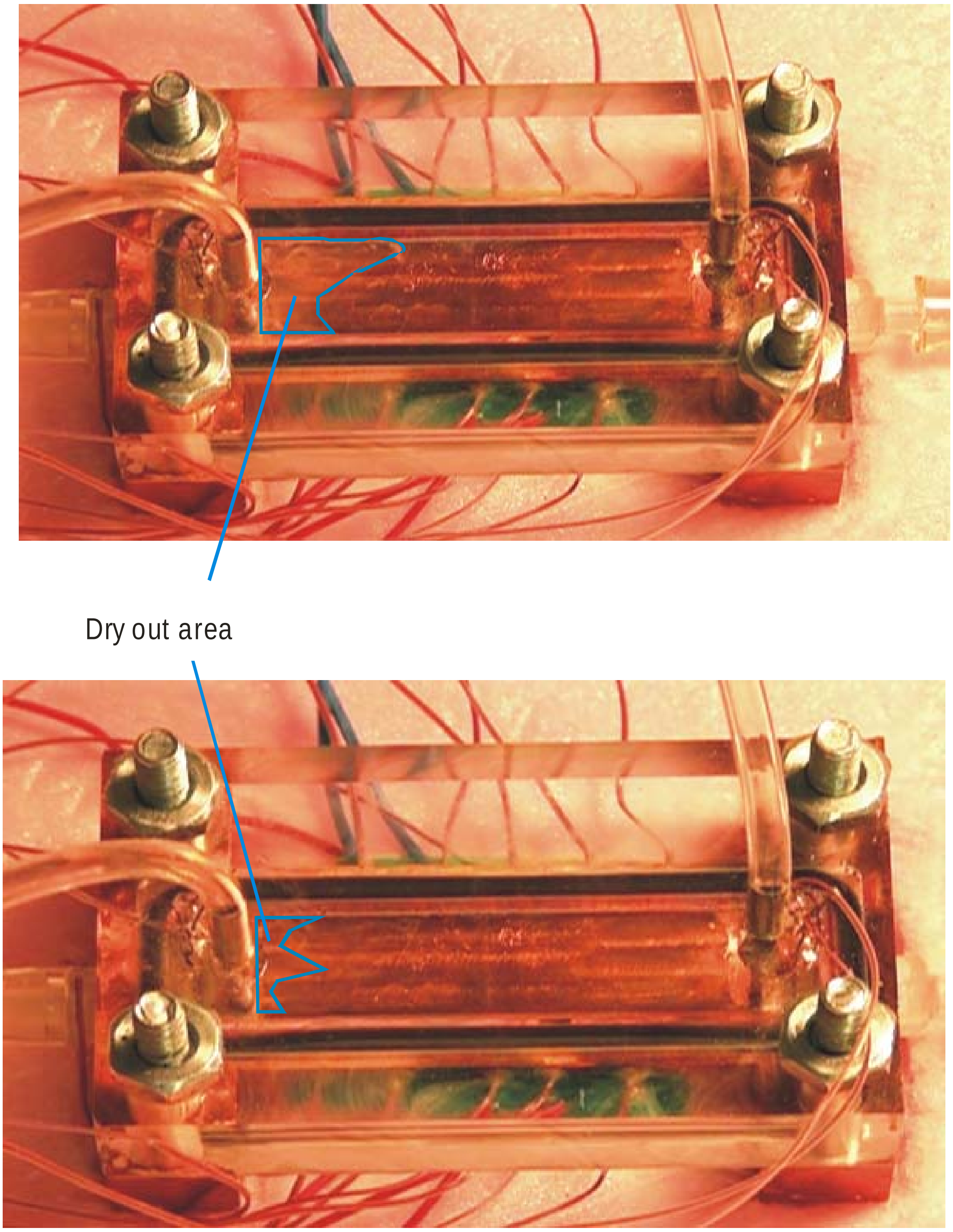

Figure 5.23 Dry out area during the boiling process

Even though the initial dry out appears to be observable visually, the effect of such possible local dry out was not detected in the measured temperature obtained from the sub-surface thermocouples. This could be due to the high "thermal mass" or long time constant of the copper heater block. Therefore, in order to figure out the effect of dry out and the phenomena of the channel, IR thermography is needed.

Figure 5.24 shows the repeatability of two-phase experiment of 110 μm gap channel. The experiments were done under the same condition with mass flux of 250 kg/m^2-s and 760 kg/m^2-s. Figure 5.24 (a) is the result of mass flux of 250 kg/m^2-s with several different heat fluxes. The experimental results at low quality are very close between different experiments, the deviation of the experimental results are less than 3%. The deviation between experiments becomes larger as the quality increases which can reach up to 7%. The experimental result of repeatability with mass flux of 760 kg/m^2-K with various heat fluxes is shown in Figure 5.24 (b). For the result of this experiment, it is hard to see the effect of different heat fluxes on the local heat transfer coefficient and all of different experiment data fall into the range of 4%. The repeatability of our experiment is confirmed by these experiments.

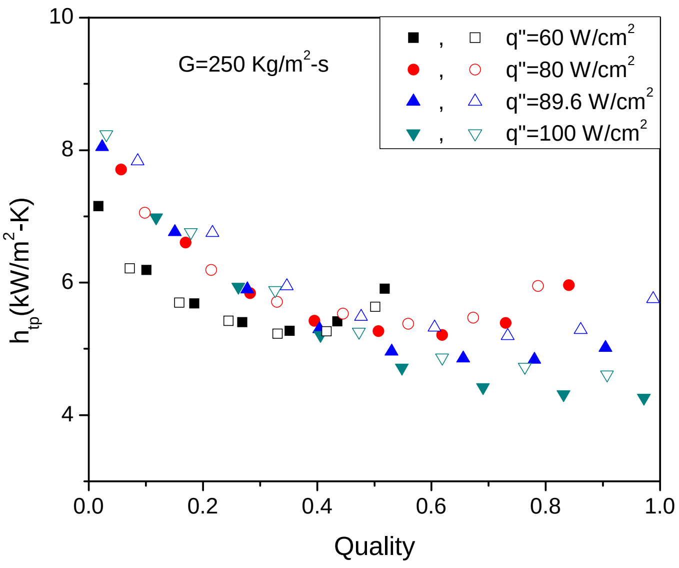

(a)

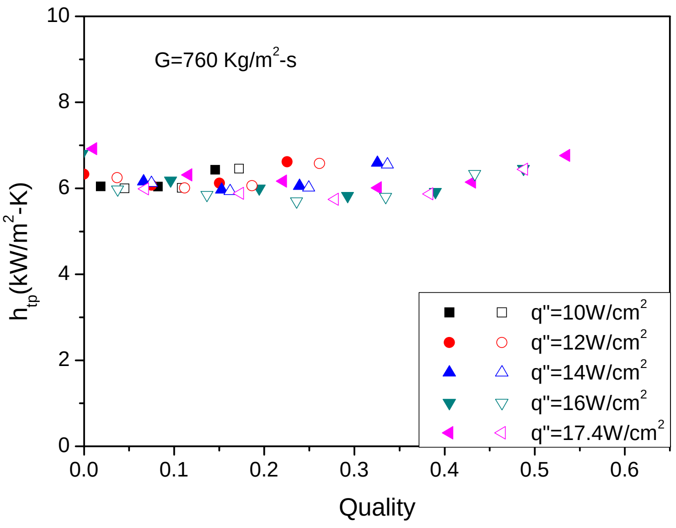

(b)

Figure 5.24 Repeatability test result of 110 µm gap channel

In order to confirm that our result of 110 µm gap channel is still within the boundary of Shah's and Chen's correlations, the data was projected in the flow regime map with Shah's and Chen's correlation. Figure 5.25 shows the flow regime map. As same as 500 µm and 210 µm gap channel, the data in the Intermittent regime are close to the Shah's correlation and the data in the Annular regime are close to the Chen's correlation.

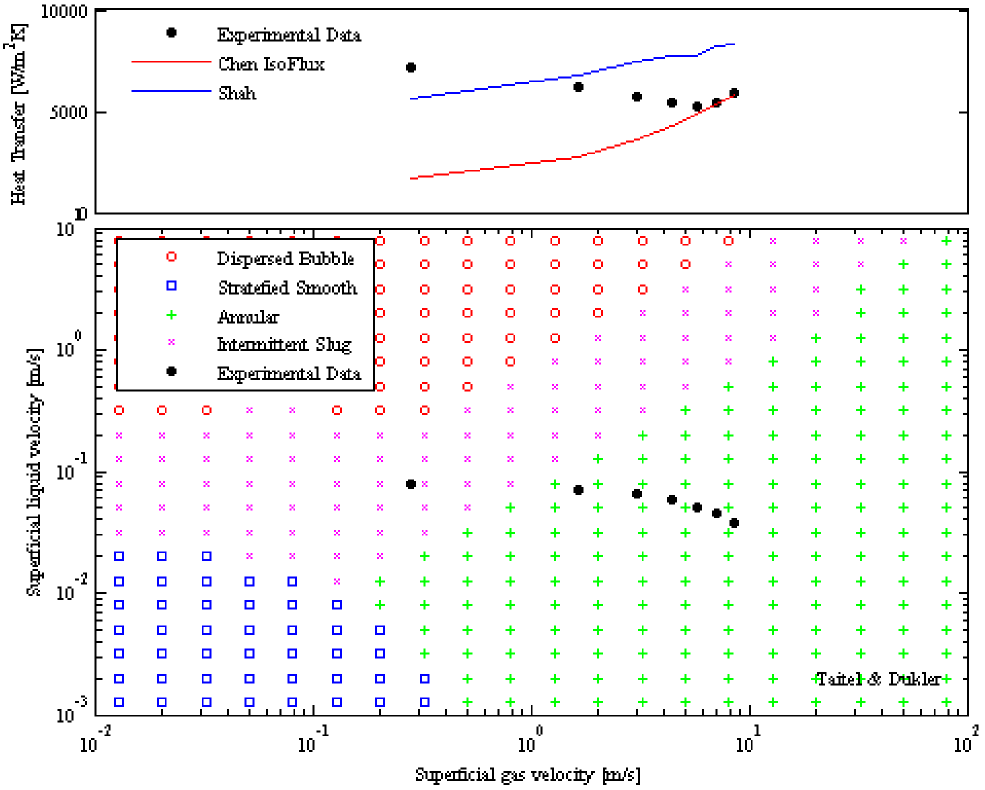

Figure 5.25 Projected to the flow regime map data of 110 μm gap channel

Figure 5.26 is the result of comparison of the experimental result with the Shah's correlation and Chen's correlation which was calculated based on the average quality in the channel. For the 110 μm channel gap case, most of the average heat transfer coefficient are close to Chen's correlation. This would be due to the small gap, when the boiling starts the flow regime changes suddenly to the Annular regime.

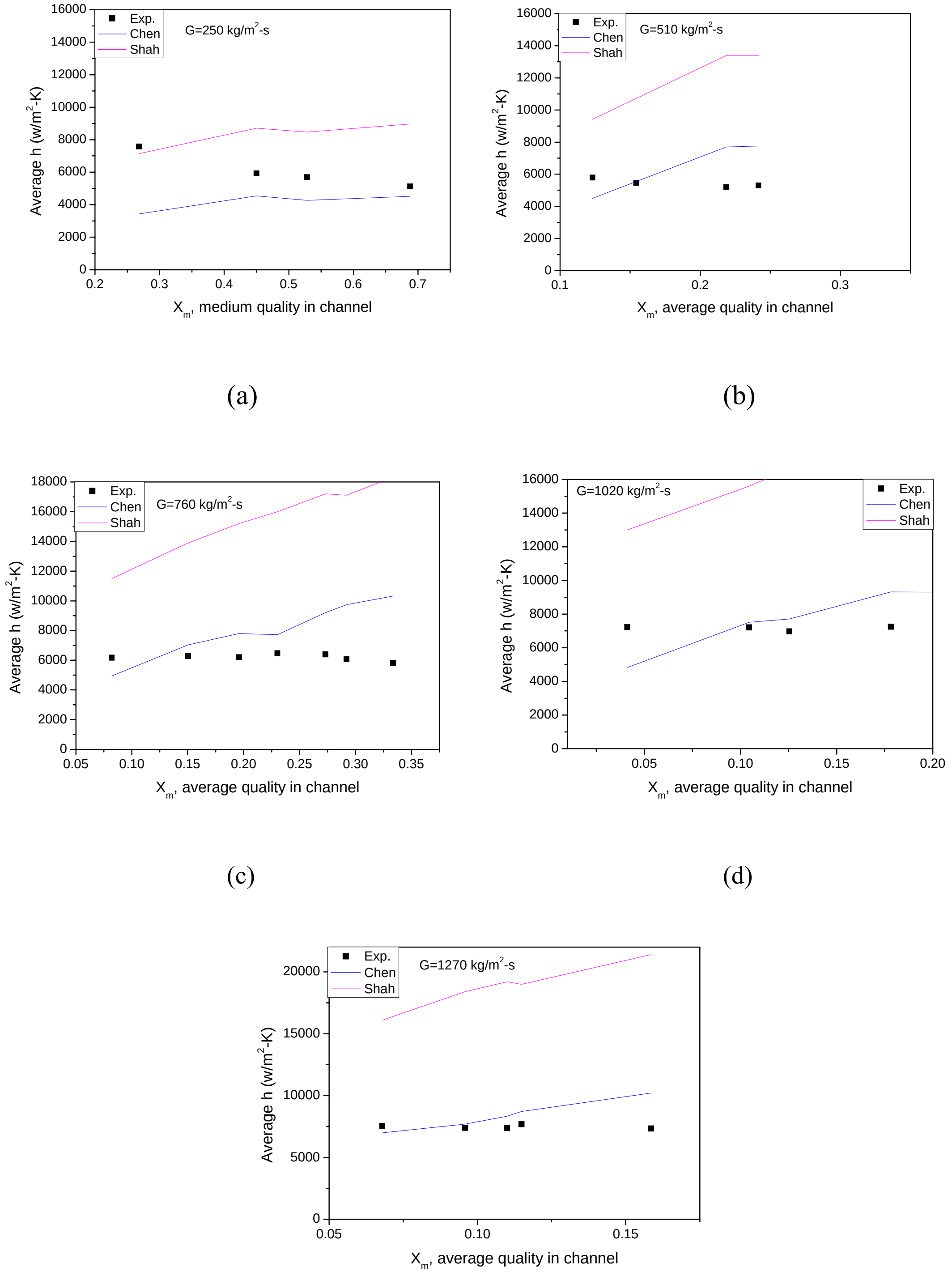

(a) (b)

(c) (d)

(e)

Figure 5.26 Average heat transfer coefficient comparison with Chen's and Shah's correlation.

5.4 Conclusion

In the analysis of the characteristic of the micro single gap channel in the single phase, a heat transfer coefficient of 23 kW/m^2-K was achieved with a 210 μm gap channel with water and a heat transfer coefficient of 5 kW/m^2-K was achieved at 110 μm gap channel with FC-72 for the single phase. As expected, the smaller gap demonstrates better heat transfer capability; FC-72's heat transfer capability was 25% that of water.

The result of the two-phase heat transfer capability of the single gap channel was compared with both Chen's correlation and Shah's correlation by utilizing the flow regime map. Data in the Intermittent regime is close to Shah's correlation while data in the Annular regime is close to Chen's correlation, though local dry may explain some of the values that fell below the Chen predictions.

As to the 110 μm gap, most of the data fall in the Annular regime as the small gap of the channel creates Annular flow almost from the channel inlet. As in the single-phase experiment, a smaller gap proves to have a better heat transfer capability.

Chapter 6

Porous Foam Channel

Porous foams are an attractive way to enhance convective heat transfer in tubes and channels due to the foam's high ratio of surface area/ volume. Moreover, the dispersion conductivity which is caused by the recirculation, mixing, and "disturbance" of the flow by the porous matrix further enhances the heat transfer rate. The consequent relative insensitivity of channel heat transfer to the thermal conductivity of the fluid makes porous foams an attractive candidate for heat exchange with low conductivity fluids such as the dielectric fluids. However most of the available experimental results are limited to water and air. Therefore, in this chapter, the pressure drop, single-phase and two-phase heat transfer characteristic of porous foam is studied and compared with the experimental result of water and FC-72.

6.1 Introduction

Flow through porous media has been studied in detail beginning with Darcy's work which was published in 1856. With the emergence of the open cell metal foam, it has been recognized that porous media could be used in creating compact heat exchangers due to their superior characteristics of:

- Light weight
- Low mechanical modulus
- Low cost
- High contact area with the fluid (much higher than micro-channel)

- Thermal conductivity that is only weakly dependent on the conductivity of the fluid
- Lower thermal resistance than plate fin microchannels [40]

The reduced sensitivity of the effective thermal conductivity of a porous medium to the thermal conductivity of the fluid is a vital consideration in heat exchanger design. In view of this characteristic, the combined effect of metal foam with a low conductivity fluid would be much better than that of an empty channel. However, even though the metal foam is an excellent material for heat transfer to a low conductivity fluid, such as dielectric liquids used in electronic and photonic cooling applications, most of the existing data is with water and air and it is nearly impossible to obtain useful information related to the behavior of porous foams with other fluids.

In this chapter the heat transfer characteristics of single-phase and two-phase parallel plate channel, which is filled with metal foam, is studied and compared to the empty parallel plate channel.

Figure 6.1 is a schematic diagram of a design which uses porous foam as a microchannel cold plate to create a high performance compact heat exchanger at the submount level in an LED package. In this design the LEDs array is soldered to the submount and the porous foam is soldered to the substrate. As shown in Figure 6.1, the foam material “sandwich” is soldered to the heat source. Wire bonds electrically connect the metal core PCB and Silicon submount, which serves to provide electrical connections and thermal spreading from the individual LED’s.

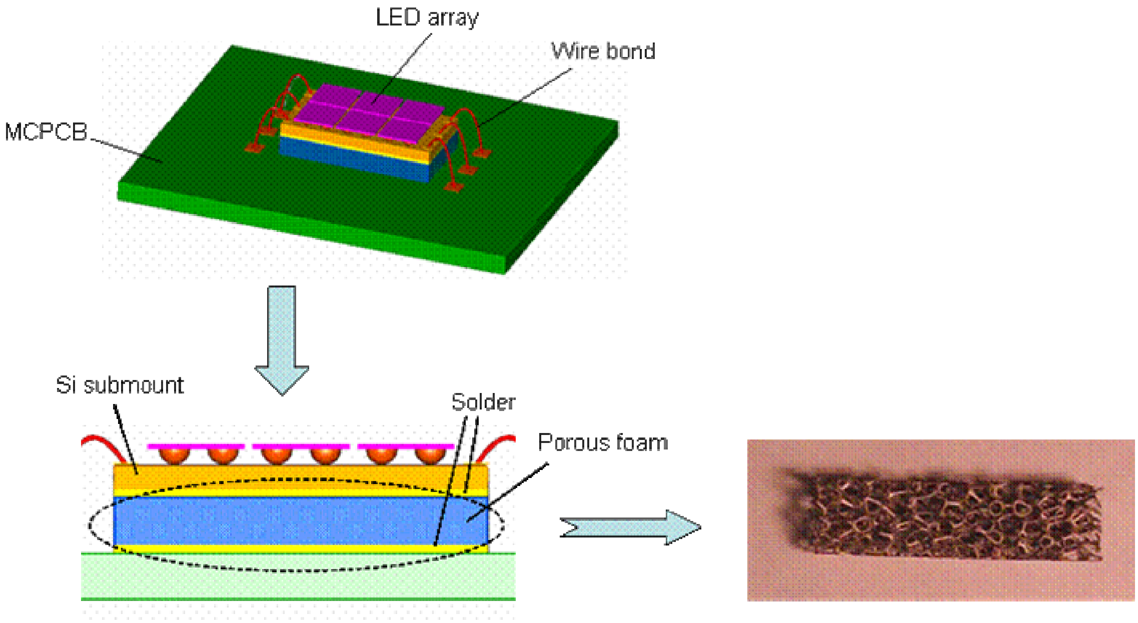

Figure6.1 Schematic diagram of porous foam cold plate

The effective thermal conductivity of porous foam, with heat conducting through the solid and fluid phases in parallel, can be written as:

$$k_e = \varepsilon k_f + (1-\varepsilon)k_s \tag{6.1}$$

Based on the Eq. (6.1), the empirical correlation of effective thermal conductivity of foam material can be expressed by [41]

$$k_e = \varepsilon k_f + A(1-\varepsilon)^n k_s \tag{6.2}$$

where, k_f is the thermal conductivity of the fluid, k_s is the thermal conductivity of the solid, ε is porosity, n is set equal to 0.763 and A is 0.195 for water and 0.181 for air [41].

As shown in Eq. (6.2), the effective conductivity of porous metal foam is not sensitive to the thermal conductivity of the fluid. Convective transport in porous media has been studied extensively. A majority of the studies in the literature deal with low porosity media, such as packed beds having porosity from 30% to 60%. For the high porosity metal foams ($\varepsilon > 80\%$), data in the literature can serve only for feasibility studies and not for detailed design, since the existing models must be calibrated with experimental results [42]. Very little data, if any, exists for two-phase cooling with porous foams.

6.2 Single-phase Flow Analysis

6.2.1 Pressure Drop Analysis

Transport in porous media involves complex flow patterns around solid particles or fibers and due to the random orientation of the solid phase, exact solutions to the detailed local flow field are impossible. Tenable solutions are found by volume averaging the governing equations. The steady, volume-averaged continuity and momentum equations for forced convection in a porous medium are [42] - [45] $\nabla \overline{u} = 0$ (6.3)

$$\frac{\rho}{\varepsilon^2}\left(\overline{u}\nabla\overline{u}\right) = -\frac{\mu}{K}\overline{u} - \nabla p + \rho g - \rho\frac{f}{\sqrt{K}}\left|\overline{u}\right|\overline{u} + \frac{\mu}{\varepsilon}\nabla^2\overline{u} \qquad (6.4)$$

For 2-dimesional flow, Eq. (6.4) can be reduced to

$$0 = -\frac{dp}{dx} - \frac{\mu}{K}u - \rho\frac{f}{\sqrt{K}}u^2 + \frac{\mu}{\varepsilon}\frac{d^2u}{dy^2} \qquad (6.5)$$

Using the non dimensional terms, $u_D = -\frac{K}{\mu}\frac{dP}{dx}$, $U = \frac{u}{u_D}$, $\mathrm{Re}_k = \frac{\rho u_D \sqrt{K}}{\mu}$,

$Y = y\left(\frac{\varepsilon}{K}\right)^{1/2}$ and $X = x\frac{\varepsilon}{\sqrt{K\,\mathrm{Re}_k\,\mathrm{Pr}}}$

Eq.6.5 it can be expressed as

$$0 = 1 - U - f\,\mathrm{Re}_k\,U^2 + \frac{d^2U}{dY^2} \tag{6.6}$$

Since the velocity boundary layer growth in porous media takes place over a very short distance, in most practical cases the hydrodynamic entrance length is negligible [46]. Since the entering flow is thus fully developed, the "y" component of equation (6.5) is identically zero.

Then the average velocity becomes

$$U_a = \frac{-1 + (1 + 4f\,\mathrm{Re}_k)^{1/2}}{2f\,\mathrm{Re}_k} \tag{6.7}$$

The momentum equation in the x-direction can be written as

$$-\frac{dp}{dx} = \frac{\mu}{K}u + \rho\frac{f}{\sqrt{K}}u^2 \tag{6.8}$$

where K is permeability and f is the inertial coefficient or the so-called Ergun coefficient.

Eq. (6.8) is called the extended Darcy's equation and is widely accepted for steady-state, unidirectional pressure drop in a homogeneous, uniform and isotropic porous medium, traversed by a fully saturated incompressible fluid.

Both the permeability, K, and the inertial coefficient, f, are strongly related to the structure of the medium. In Darcy's regime (at low velocity), the permeability term is dominant but in the non-Darcy regime, viscous shear stresses become insignificant compared to the form drag.

There are several researchers who developed analytical equations for the prediction of pressure drop in porous foam material. Among them, only Calmidi and Mahajan [41] and Du Plessis [47] compared their analytical equation to the existing experimental results. Therefore, in this study, we use their correlation to figure out the parameters which affect the pressure drop.

In order to develop an approximate pressure drop prediction for the metal foam structure, Du Plessis [47], Calmidi and Mahajan [41] assume that it has an open cell structure (Figure 6.2) composed of dodecahedron-like cells, having 12 ~ 14 pentagonal or hexagonal faces, and that the face area of the pore structure is the same as the pentagonal face.

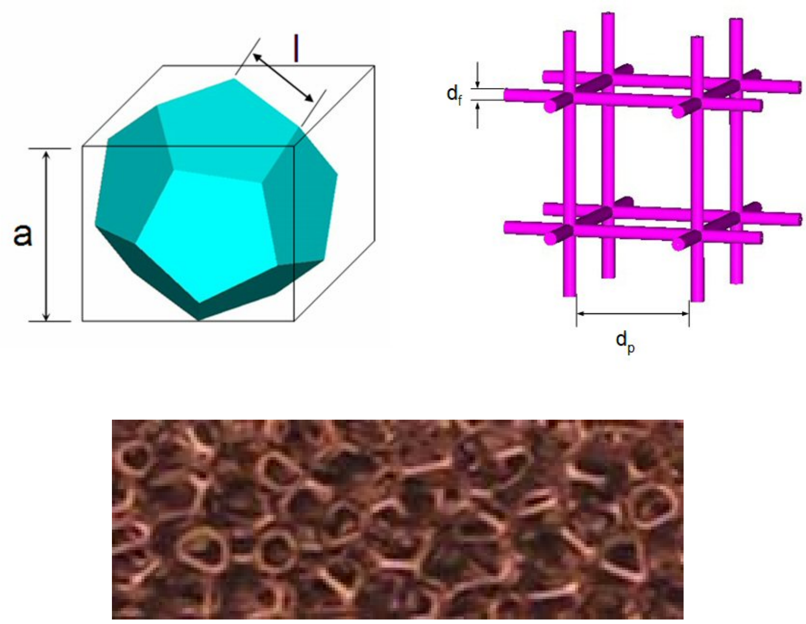

Figure 6.2 Open cell representation of metal foam

$$A = d_p^{\ 2} = 1.72l^2 = 0.35a^2 \tag{6.9}$$

where, $a = 2.23l$.

The permeability is given by

$$K = \frac{\varepsilon^2 d^2}{36\chi(\chi - 1)}. \tag{6.10}$$

where $d = \sqrt{\chi/(3\varepsilon)}d_p$, with ε being the porosity of the foam and χ the tortuosity of the porous matrix. The tortuosity can, in turn, be expressed by

$$\chi = \frac{\varepsilon d_p^2}{A_p} \tag{6.11}$$

where $A_p = (\pi/4)(d_p - d_f)^2$.

The solid volume fraction can be given by

$$\frac{d_f}{d_p} = 1.18\sqrt{\frac{1-\varepsilon}{3\pi}\frac{1}{G}} \tag{6.12}$$

where G is a shape function which accounts for the variation of fiber cross section with porosity and is given by $G = 1 - \exp(-(1-\varepsilon)/0.04)$ [41].

From eq. (6.11) and (6.12), we get

$$\frac{1}{\chi} = \frac{\pi}{4\varepsilon}\left\{1 - \left(1.18\sqrt{\frac{1-\varepsilon}{3\pi}\frac{1}{\boldsymbol{G}}}\right)^2\right\} \tag{6.13}$$

With Eq. (6.13), the tortuisity is removed from Eq. (6.10), it becomes only function of pore size and porosity.

Figure 6.3 shows a comparison of predicted and measured permeability for metal foams with various porosity with 5, 10, 20 and 40 PPI and variation of porosity from 0.899 to 0972 which was done by Calmidi et al. [41], and Bhattacharya et al. [43], showing considerable experimental scatter. For a broad range of experimental data, it has been found that the average standard deviation between predicted and measured permeability for metal foams is approximately 15% [43].

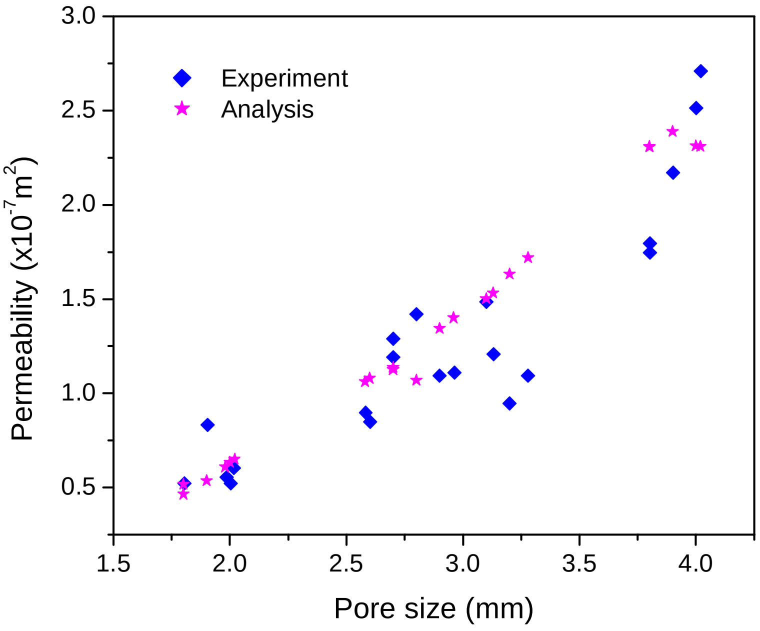

(a)

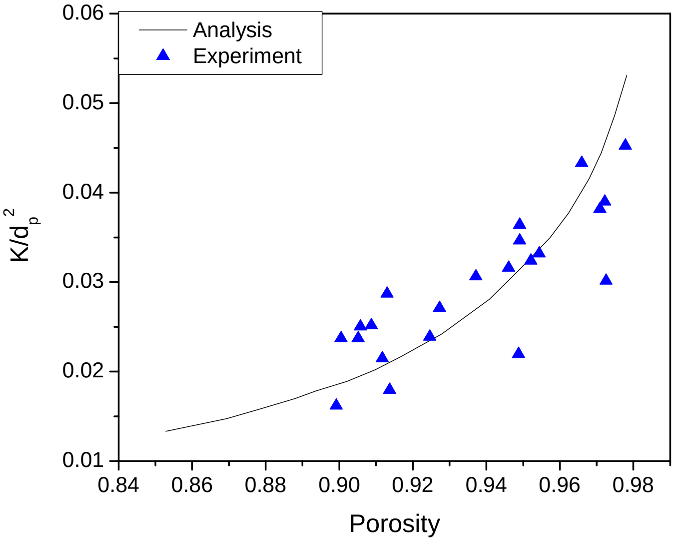

(b)

Figure 6.3. Comparison of experiment and analysis result of permeability (a) pore size effect and (b) porosity effect [43]

Use of the well-known Ergun's equation for the inertial coefficient of a packed bed can be expressed in the form of [44]

$$f = 1.8/(180\varepsilon^5)^{1/2}\ . \tag{6.14}$$

Du Plessis and Calmidi developed a relation for f using an asymptotic matching approach and found that the inertial coefficient for a porous foam can be expressed by [43]

$$f = 0.095\frac{C_D(\varepsilon)}{12}\sqrt{\frac{\varepsilon}{3(\chi-1)}}\left(1.18\sqrt{\frac{1-\varepsilon}{3\pi}}\frac{1}{G}\right)^{-1} \tag{6.15}$$

where, $\boldsymbol{C_D}(\varepsilon)$ is function of porosity but equal to 1.2 when the porosity is greater than 85%, i.e. $\varepsilon > 0.85$. Figure 6.4 shows a comparison of the predicted and measured values of the inertial coefficient, applying this asymptotic equation to the experimental results for Calmidi and Mahajan [41]. In Fig 6.5 it may be seen that the standard deviation between the predicted and measured inertial coefficient is around 8 % [43].

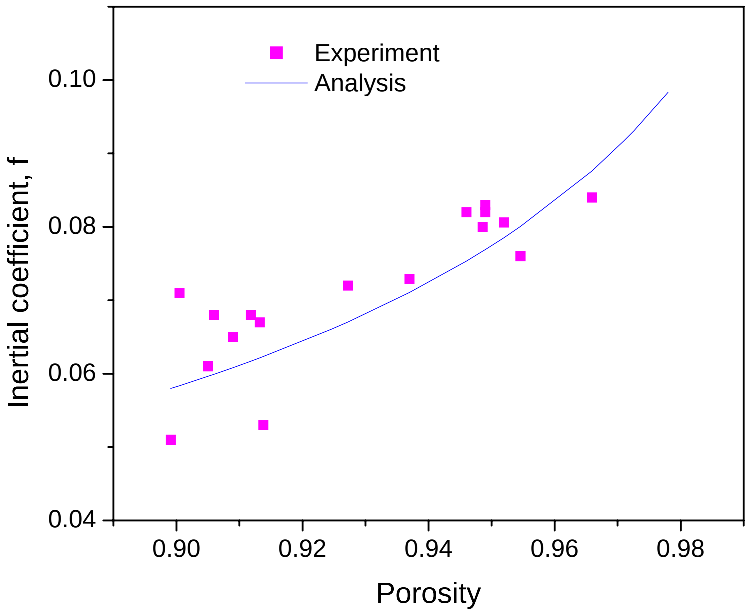

Figure 6.4 Comparison of inertial coefficient (friction factor)

From Eq. (6.8) to Eq. (6.14), it is evident that every parameter related to pressure drop can be determined from the porosity and pore size.

6.2.2 Open Cell Metal Foam Channel

In the present study of the thermal performance of an open cell, metal foam filled channel, the 3 different copper foams shown in Figure 6.5 were tested. These 3 samples were selected to provide a contrast in pore size, using samples with 10 and 20 pores-per inch (PPI) nickel-plated copper, respectively, at a porosity of 95% and a contrast in porosity, by adding a copper foam sample with 92% porosity and 20 PPI.

The channel previously used to determine the thermofluid characteristics of an unfilled microgap was modified to accommodate a 10 mm wide by 37 mm long foam layer. The foam thickness and, consequently, channel height was selected to assure that at least two full pores would be present in the foam layer. With the largest pore of the 10 PPI specimen measured at approximately 3 mm, the channel height was fixed at 7 mm for these experiments. The specimens were soldered to the copper base block using hot plate. The soldering was done very carefully in order not to block the pores of the foam by solder.

It should be noted that even when the stated porosity and PPI of metal foam samples is the same, the properties of the foam could be different depending on the manufacturer. This is because each manufacturer employs a different method of making metal foam such as metallic sintering, metal deposition through evaporation, electrodeposition or chemical vapor decomposition [48]. The nickel plated copper foam which was made by Dalian Thrive Metallurgy Import and Export is manufactured by directional solidification of metal from a super-heated liquid state in an environment of overpressures and high vacuum. The resulting material has a reticulated structure of open, decahedronal-shaped cells connected by continuous, solid metal ligaments. The solid-metal ligaments routinely test to 99% purity of the parent alloy (to AMS specifications), are not porous, and approximate single strand drawn wire. The matrix of cells and ligaments is completely repeatable, regular, and uniform throughout the entirety of the material [49].

The copper foam of 92% porosity and 20 PPI was made by Porvair Fuel Cell Technology and this company used metal sintering. In order to create metal foam, metallic particles are suspended in slurry and coated over a polymeric foam substrate. The foam skeleton is vaporized during the heat treatment and the metallic particles sinter together to create the product. As the result of a manufacturing technique, the metal foam has hollow ligaments [50].

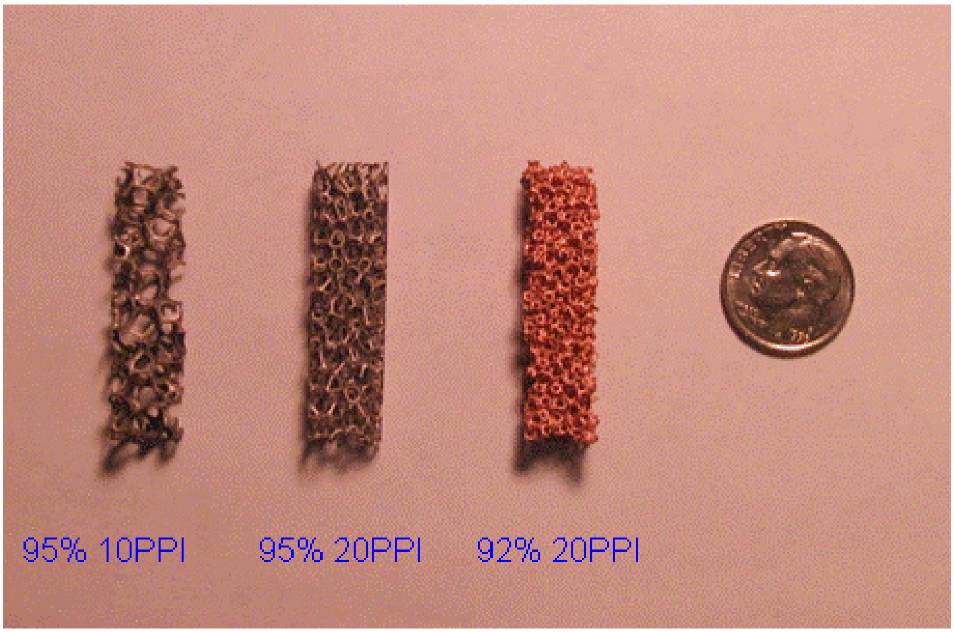

Figure 6.5 Photograph of open cell metal foam

6.2.3 Pressure Drop Experiment

This section presents and discusses the measured values of the pressure drop of water and FC-72 flowing up to 10.5 ml/s. It also examines the predictability of the pressure drops with the relations presented in the previous section, Eqs. (6.10) ~ (6.14). Due to the high surface tension and viscosity of water, only FC-72 is used as the working fluid in the less porous, smaller pore (92%, 20 PPI) foam sample. Figure 6.7 shows the fluid effect on the pressure drop of porous media, revealing that the pressure drop of water in 95% porosity foam to be 3 ~ 4 times greater than FC-72 with 10 PPI. Figure 6.7 (a) shows the pressure drop of an empty channel for the flow of water and FC-72, which is calculated by Eq. (4.2). Due to the large gap of the channel, the pressure is nearly negligible. The pressure drop for 95% porosity and 10PPI foam is 50 times greater than open channel with water and 10 times greater than open channel with FC-72. As the pore size becomes smaller (higher PPI), the deviation of pressure drop between water and FC-72 becomes greater. In the foam configuration of 95% porosity and 20 PPI, the pressure drop of water is 4-4.5 times greater than FC-72. As expected, the higher pressure drop is for water at the same volumetric flow rate as FC-72 due to the high viscosity of water. An error bar of 15% is drawn in Figure 6.6 (a) and Figure 6.6 (b).

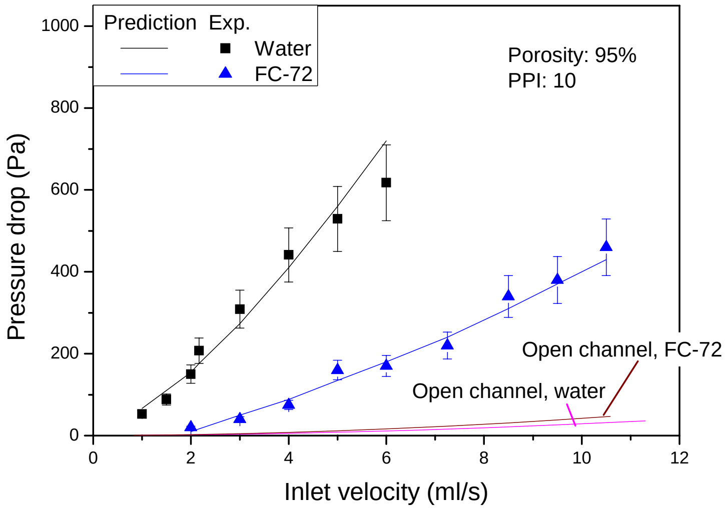

(a)

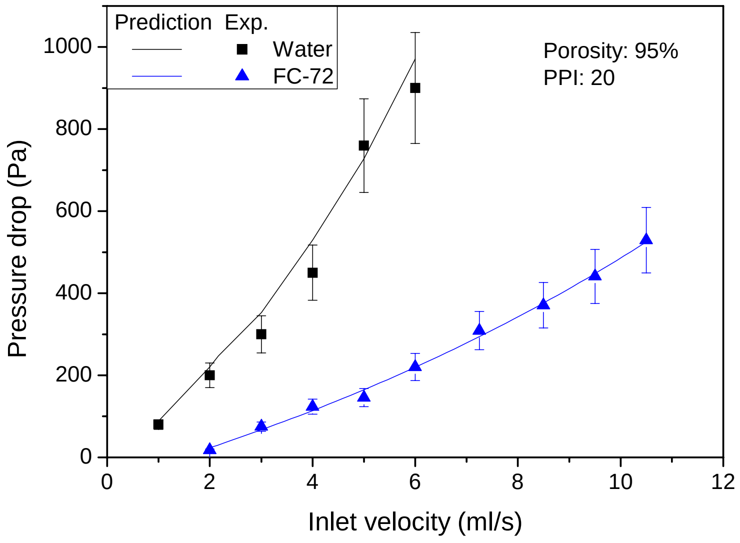

(b)

Figure 6.6 Experimental result of pressure drop (a) 95% porosity and 10 PPI (b) 95% porosity and 20PPI

Figure 6.7 displays the experimental result of pressure drop for different foam configurations with the same working fluid in the range of 1 ~ 6 ml/s flow rate. It shows clearly the PPI and porosity effect on the pressure drop. With the 95% porosity foam, while the pressure drop for the two pore sizes is relatively similar at the low flow rates, the pressure drop for the 20 PPI foam increases more steeply as the flow rate increases, becoming 35% greater for the smaller pore size at 6 ml/s. With FC-72 as the working fluid, the pressure drop is less sensitive to the change of the pore size. The pressure drop increases 20% for the change from 10 PPI to 20 PPI. However, the pressure drop for 92% porosity and 20 PPI foam is 42% greater than for the 95% porosity with the same pore size of 20 PPI. In Fig 6.7(a), the experimental uncertainty of 15% for water and 10% for FC-72 is indicated in the experimental results.

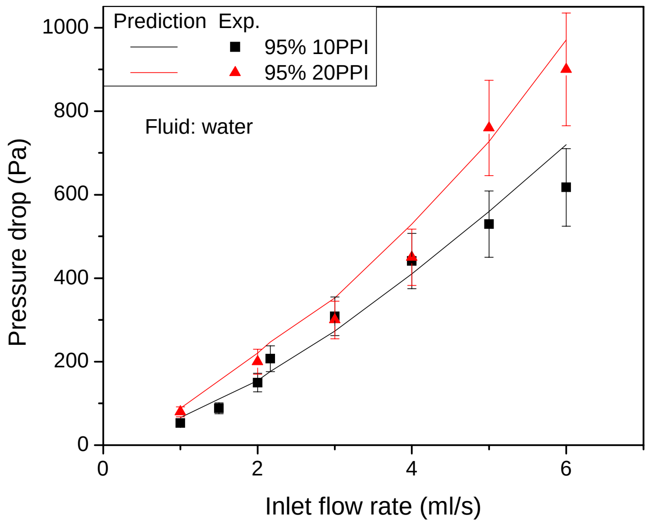

(a)

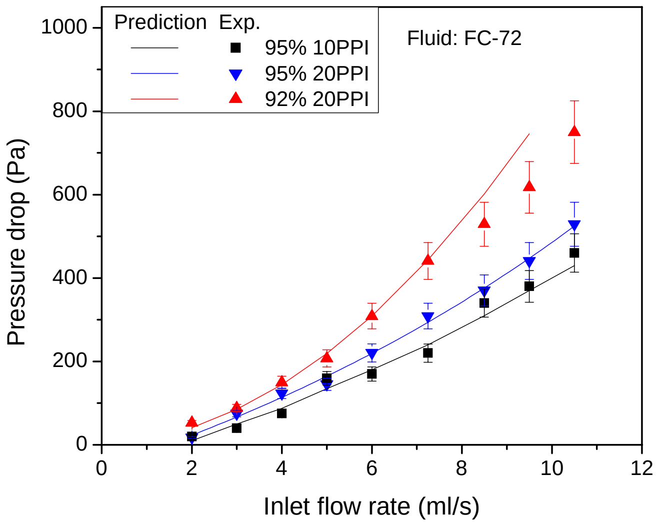

(b)

Figure 6.7 Experimental result of pressure drop (a) 95% porosity and 10 PPI (b) 95% porosity and 20 PPI

Overall experimental results of high PPI foam are closer to the prediction. The larger discrepancy for the low PPI foam may well be due to the low pressure drop which is nearly at the low limit of the pressure transducer, leading to a relatively larger measurement error.

6.2.4 Heat Transfer Performance

The volume averaged homogeneous energy equation for porous media is given by

$$\rho C_p \bar{u} \cdot \nabla \bar{T} = \nabla \cdot \left(k_e \nabla \bar{T}\right) - \rho C_p \nabla \cdot \tilde{u}\tilde{T} \qquad (6.15)$$

where k_e is the effective conductivity [41].

In Eq. (6.15) the convective term is divided into average and spatially varying components. The last term is due to thermal dispersion resulting from flow disturbance, mixing, and recirculation of local fluid streams as the fluid passes through the porous media [51]. This can be viewed as a diffusive process related to the overall temperature gradient and the enhanced "dispersion" conductivity, representing the combined thermal transport effects of conduction and microconvection. Therefore the spatially varying term in Eq. (6.15) can be expressed as

$$\rho C_p \nabla \cdot \tilde{u}\tilde{T} = -k_d \nabla T \qquad (6.16)$$

The dispersion conductivity k_d is given by

$$k_d = \rho C_p \gamma \sqrt{K} u \qquad (6.17)$$

where γ is dispersion coefficient and K is the above defined permeability.

Different researchers have suggested different values for the dispersion coefficient. Calmidi and Mahajan [41] suggested that the dispersion coefficient for water be taken as 0.06 and 0.1 for air, based on numerical simulation and comparison with the experimentally determined dispersion coefficient of 0.025, suggested by Tien and Hunt [51]. However, still the best way to find the dispersion coefficient is from the data fitting of the experimental results [52].

For a two-dimensional flow in uniform porosity media, the energy equation is express by

$$\bar{u}\frac{\partial \bar{T}}{\partial x} = \alpha \frac{\partial}{\partial y}\left[\left(1+\frac{k_d}{k_e}\right)\frac{\partial \bar{T}}{\partial y}\right] \tag{6.18}$$

or, substituting the previously defined non dimensional velocity and Reynolds Number, i.e.

With the following non-dimensional term,

$$U = \frac{u}{u_D},\ \mathrm{Re}_k = \frac{\rho u_D \sqrt{K}}{\mu},\ X = x\frac{\varepsilon}{\sqrt{K\,\mathrm{Re}_{D\,\mathrm{Pr}}}},\ Y = y\left(\frac{\varepsilon}{K}\right)^{1/2} \text{ and } \theta = \frac{T-T_i}{T_w - T_i}$$

Eq. (6.18) can be express as

$$U\frac{\partial \theta}{\partial X} = \frac{\partial}{\partial Y}\left[\left(1+\gamma\,\mathrm{Re}_k\,\mathrm{Pr}_e\,U\right)\frac{\partial \theta}{\partial Y}\right] \tag{6.19}$$

With the boundary condition of slug flow approximation $\theta = 0$ at $X = 0$ and $Y = \infty$, $\theta = 1$ at $Y = 0$ and integrating the non-dimensional energy equation Eq. (6.19), yields

$$\theta = 1 - erf\left\{\frac{Y}{2}\left[\left(1+\gamma\,\mathrm{Re}_k\,\mathrm{Pr}_e\right)\frac{X}{U_a}\right]^{-1/2}\right\} \tag{6.20}$$

Assume that the velocity at the wall is zero, i.e. $V|_{Y=0} = 0$, and exclude mass flow through the plate surface, then the local Nusselt number can be calculated from differentiating of the Eq. (6.20) and can be expressed by

$$Nu_x = \left(\frac{\partial \theta}{\partial Y} \right)_{Y=0} \tag{6.21}$$

Consequently, the length averaged Nusselt number can be calculated from the integration of Eq. (6.21) and expressed by

$$\overline{Nu} = \frac{1}{L} \int_0^L Nu_x dx = 2\left[\frac{1}{\pi} \mathrm{Re}_k \, \mathrm{Pr}_e \, Da_L (1 + \gamma \mathrm{Re}_k \, \mathrm{Pr}_e) \right]^{1/2} \tag{6.22}$$

where Da_L is the inverse Darcy number, $Da_L = L / \sqrt{K}$, the effective Prandtl number is defined as $\mathrm{Pr}_e = (\mu C p)_f / k_e$, the Reynolds Number is as before, $\mathrm{Re}_k = \rho u_a \sqrt{K} / \mu$.

The predicted values by Eq. (6.22) is compared to the existing experimental data which was used by Tien and Hunt [51] and Calmidi and Mahajan [41].

The permeability of 94% 10 PPI, 97% 5 PPI and 10 PPI which was determined by experiment are 1.2 x 10^{-7}, 2.52 x 10^{-7} and 1.64 x 10^{-7} m^2 and the dispersion coefficient of 0.06 is used. The results have been found to be consistent with the experimental results for the flow of water through an aluminum foam with porosity of 94% and 97% and pore counts of 5 PPI and 10 PPI, respectively [51] (Figure 6.8).

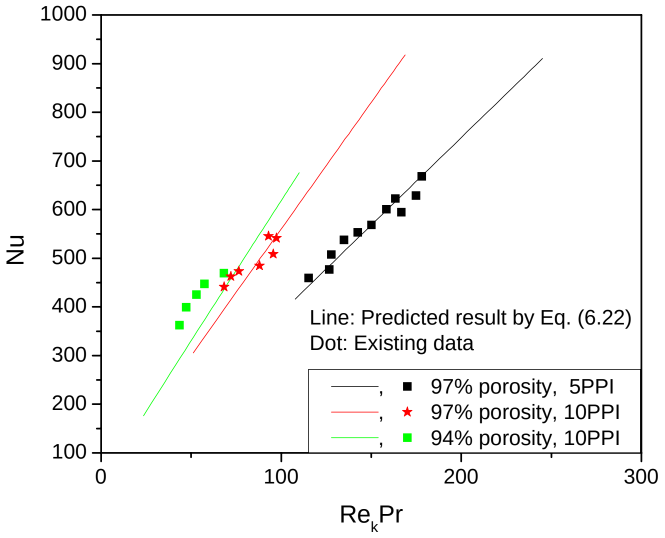

Figure 6.8 Nusselt number calculation of metal foam [51]

6.2.4.1 Experimental Results

Figure 6.9 (a) shows the result of the present single-phase heat transfer experiment using copper foam with 95% porosity and 10 PPI. The experiment was done with water and FC-72. The heat transfer coefficient was found to increase with increasing flow rate. The error bar of 10% error and 20% error is drawn to the experimental results with values calculated via the Nu correlation given by Eq. 6.22. The predicted permeability of 95% porosity and 10 PPI is 1.3 x 10^{-7} m^2 and 0.06 of dispersion coefficient is used for both fluids. The deviation of the different experiments is less than 10% as seen in Figure 6.10, the repeatability of this experiment is confirmed. The heat transfer coefficients for FC-72 were found to lie substantially below that of water, averaging about 35% of the water values. The heat transfer capability of an empty channel which has the same dimension as the foam filled channel is shown in Figure 6.9 (a). These predicted values are calculated by

Eq. (4.9) which is used for the prediction of single gap channel. The improvement of heat transfer capability achieved by the foam insert is 2 times greater for water and 3 times greater for FC-72.

Figure 6.9 (b) shows the result of single-phase heat transfer experiment with the 95% porosity and 20 PPI foam. The predicted permeability of 95% porosity and 20 PPI is 1.0 x 10^{-7} m^2 and 0.06 of dispersion coefficient is used for both fluids. 10% error bar and 20% error bar are drawn to the experimental results of water and FC-72, respectively. As for the lower PPI, larger pore foam, the heat transfer capability of FC-72 was 35% of water, at the same volumetric flow rate.

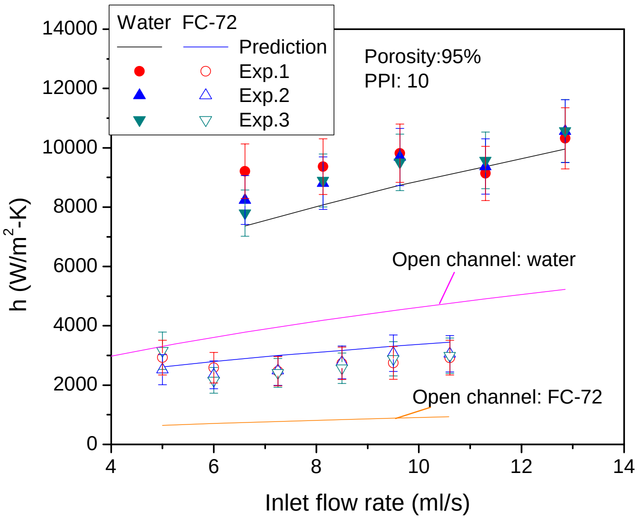

(a)

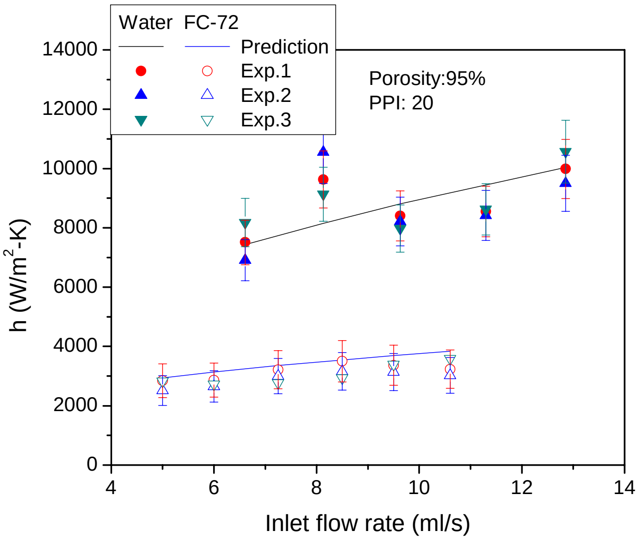

(b)

Figure 6.9 Heat transfer rate comparison of different coolant in same foam configuration (a) 95% porosity and 10 PPI (b) 95% porosity and 20 PPI

Figure 6.10 shows more explicitly the effect of the pore count (PPI) and porosity on the metal foam heat transfer coefficient. As shown in Figure 6.10 (a), the change from 10 PPI to 20 PPI is theoretically expected to result in a 5% increase in the heat transfer coefficient to water. This is due to the enhancement of the dispersion conductivity, k_d, due to the smaller pore size. However, it is hard to notice this effect in the experimental data because this relatively small effect is in the range of experimental error.

Figure 6.10 (b) shows the experimental results for heat transfer to FC-72 flowing through a metal foam with 95% porosity and 10 and 20 PPI pore counts, as well as through a 92% porosity foam and 20 PPI pore counts. If the porosity is held constant, changing the pore size (PPI) by a factor of two does not significantly affect the heat transfer rate. Because the change of pore size only changes the dispersion conductivity, the effect is limited. However, if the porosity is lowered - which means that the solid portion of the foam is increased - the effective thermal conductivity becomes higher and the heat transfer coefficient should be expected to increase by approximately 30% for the 3% change in porosity.

This heat transfer enhancement with lower porosity is embedded in the Nusselt number correlation used to predict the metal foam heat transfer coefficients. However, due to the differences in the manufacturing processes used by different vendors, the material properties of the purchased foam could vary from one manufacturer to the next, masking the anticipated porosity effect. The 92% porosity foam was manufactured with organic polymer foam which, according to the manufacturer, would be burned out during the manufacturing process, although sometimes it remains in the foam and lowers the thermal conductivity of the foam. Such an organic residue was observed in the foam which was used for our experiment. It would thus appear that this could be the reason for the low heat transfer rate observed in the experiment with the 92% porosity foam.

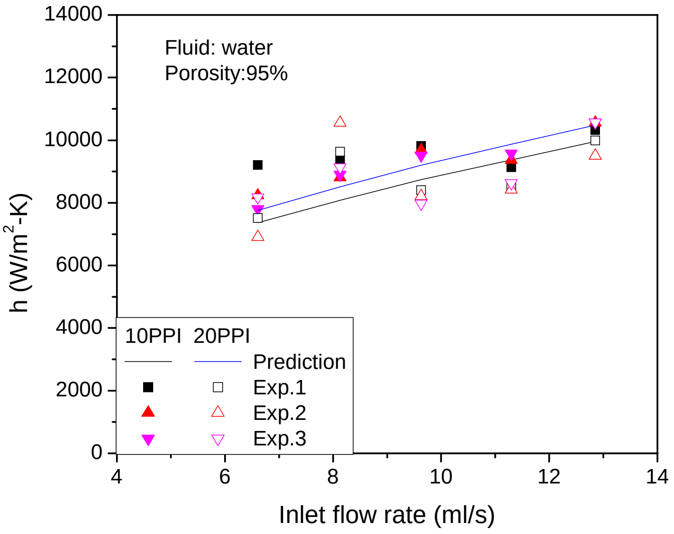

(a)

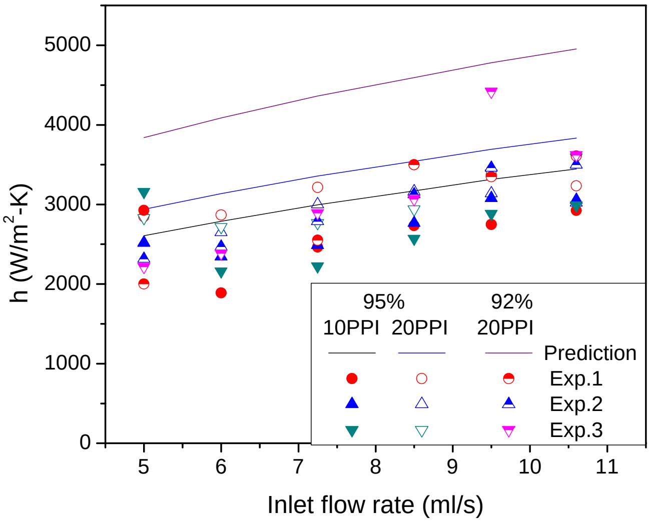

(b)

Figure 6.10 Heat transfer rate comparison of different foam configuration with same coolant (a) water (b) FC-72 as coolant

The dispersion coefficient of 0.06 is used for the prediction of heat transfer capability for water and agrees with the experimental result to within 10%, thus confirming the suggested dispersion coefficient for water. In order to figure out the proper dispersion coefficient for FC-72, the predicted correlation values with different dispersion coefficients are compared with experimental results. The comparison is shown in Figure 6.11. The line shows the result of different dispersion coefficient and the dot shows the experiment and 10% error bar is drawn in the Figure 6.11 (a) and (b). The change of dispersion coefficient from 0.06 to 0.03 decreases the predicted heat transfer coefficients 10% and further decreasing of dispersion coefficient from 0.03 to 0.01 decreases the heat transfer coefficient an additional 8%. As shown in Figure 6.11, the correlation result of 0.06 for dispersion coefficient is at the edge of 10% error of experimental result. A dispersion coefficient of 0.03 appears to provide the best agreement with the experimental results.

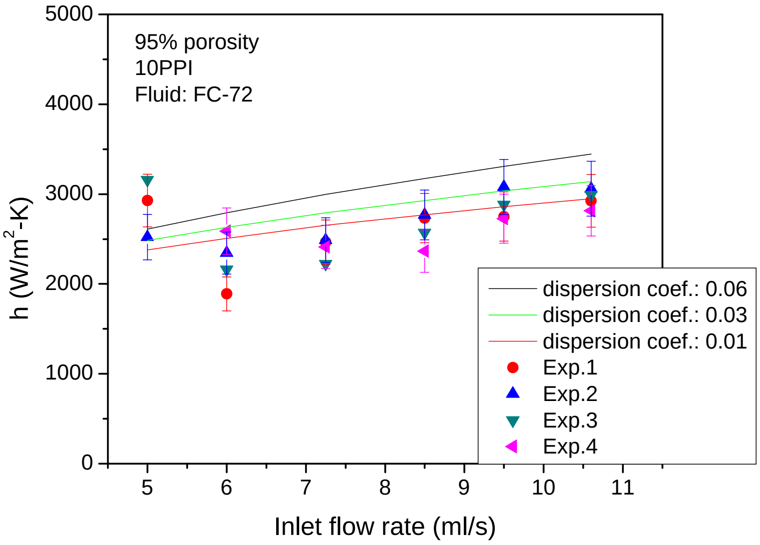

(a)

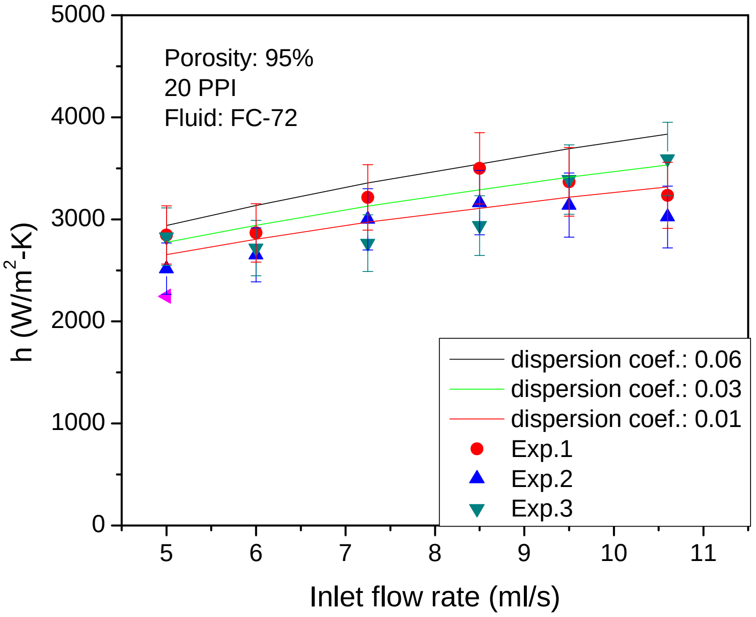

(b)

Figure 6.11 Heat transfer rate comparison of different dispersion coefficient for FC-72 (a) 95% porosity and 10 PPI (b) 95% porosity and 20 PPI

It is interesting to observe that while in the micro single gap channel, discussed in Chapter 5, the heat transfer rate of FC-72 was 25% of water for the same geometry, with the porous foam the FC-72 heat transfer coefficients rise to approximately 35% of water, at same configuration. Therefore, as previously discussed, with metal foam, the channel cooling capability is less sensitive to the conductivity of the fluid. However, even though the metal foam could increase the heat transfer rate above that of an empty channel, the achievable heat transfer coefficient is still lower than that of micro single-gap which was 24 kW/m^2-K for water and 5 kW/ m^2-K for FC-72.

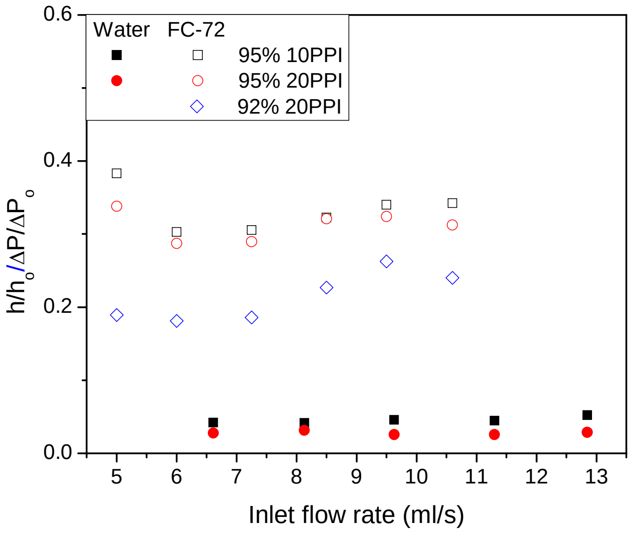

Figure 6.12 Heat transfer rate vs. pressure drop comparison of different foam configurations

As shown in Figure 6.9 (a), the porous foam enhances the heat transfer rate compared to the open channel. However, the pressure drop is also higher than the open channel. Therefore, in order to compare the heat transfer coefficient and pressure drop of foam filled channel with open channel, the ratio of heat transfer coefficient of foam filled channel to open channel is divided by the ratio of pressure drop of foam filled channel to open channel. Figure 6.12 shows the comparison of heat transfer rate vs. pressure drop of the foam filled channel and open channel. It is to be noted that across the parametric range studied, the thermal enhancement provided by the foam is between 20% and 40% for FC-72 but only a few percent for water. As the flow rate increases, the heat transfer to pressure drop ratio appears to drop slightly and then increase before reaching a peak or plateau, with the low porosity foam displaying this trend more distinctly than the high porosity foam. It is noteworthy that due to a higher pressure drop than the open channel, even though the porous foam enhances the heat transfer capability, due to the low value of the relative improvement, less than 40% for FC-72 and less than 10% for water, it appears that the higher porosity and lower PPI foam constitutes the better choice.

6.3 Two-phase flow analysis

6.3.1 Pressure drop analysis

Two-phase flow in porous media is often encountered in geothermal systems, oil reservoir engineering, multiphase packed bed reactors and nuclear reactors. However, these porous media typically possess porosities of 30% to 60% which are far below the values of interest in the use of high porosity metal foams for cooling high heat flux devices.

Following the work of Kaviany [53], to predict the pressure drop of two-phase flow in porous media, it is necessary to understand the forces which affect the pressure drop in a pipe, such as capillary, gravity, interfacial viscous shear (on A_{ls}, A_{gs}, A_{lg}), interfacial surface tension gradient on A_{lg} and inertial forces. Where, A_{ls}, A_{gs}, A_{lg} are liquid-solid contact area, gas-solid contact area, liquid-gas contact area, respectively, the momentum equations for each of the phases, including the inertial terms, become [53]

$$\begin{aligned}&\frac{\rho_l}{\varepsilon s}\left(\frac{\partial\langle u_l\rangle}{\partial t}+u_l\nabla u_l\right)=-\frac{\mu_l}{K_l}u_l-\nabla p_l+\rho_l g-\frac{\rho_l}{K_{li}}|u_l|u_l\\&+\left[K_{\mathrm{lg}}\left|u_l-u_g\right|+K_{\mathrm{lg}}\left(u_l-u_g\right)^2\right]+\mu_l\frac{K_{l\Delta\sigma}}{K_l}\nabla\sigma\end{aligned}\tag{6.23}$$

$$\begin{aligned}\frac{\rho_g}{\varepsilon(1-s)}\left(\frac{\partial\langle u_g\rangle}{\partial t}+u_g\nabla u_g\right)&=-\frac{\mu_g}{K_g}u_g-\nabla p_g+\rho_g g-\frac{\rho_g}{K_{gi}}\left|u_g\right|u_g\\&+\left[K_{gl}\left|u_g-u_l\right|+K_{gl}\left(u_g-u_l\right)^2\right]+\mu_g\frac{K_{g\Delta\sigma}}{K_g}\nabla\sigma\end{aligned}\tag{6.24}$$

The first term in Equation (6.23) is the interfacial shear stress on A_{ls} , the second term is the liquid pore pressure gradient, the third term is the body force, the fourth term is the interfacial shear stress on A_{lg} , and the last term is interfacial surface tension gradient force. Excluding the interfacial drag effects on A_{lg}, and the surface tension gradient, for simplicity, these equations can be simplified to the form [53]

$$\frac{\partial\langle p\rangle^l}{\partial x_j}=-\frac{\mu_l}{K_l}\langle u_{lj}\rangle+\rho_l g_l-\frac{\rho_l}{K_{li}}\left|\langle u_{lj}\rangle\right|\langle u_{lj}\rangle\tag{6.25}$$

$$\frac{\partial\langle p\rangle^g}{\partial x_j}=-\frac{\mu_g}{K_g}\langle u_{gj}\rangle+\rho_g g_g-\frac{\rho_g}{K_{gi}}\left|\langle u_{gj}\rangle\right|\langle u_{gj}\rangle\tag{6.26}$$

where, K_l and K_g are phase permeability of the liquid and gas which should be determined in the Darcian regime and can be expressed by

$$K_l=K\cdot K_{rl}\tag{6.27}$$

$$K_g=K\cdot K_{rg}\tag{6.28}$$

where K_{rl} and K_{rg} are the relative permeability of the liquid phase and gas phase, respectively, and these values are function of liquid hold up. The correlations of relative permeability exist in literature for a variety of situations, such as sandstone-oil-water, soil-water-gas, glass spheres-water-water vapor, trickling flow in packed bed, etc. For glass spheres-water-water vapor case, i.e. the flow of water and steam over glass beads, the relative permeability is given by Verma et al. [54], as

$K_{rl} = s^3$

$$K_{rg} = 1.2984 - 1.9832s + 0.7432s^2 \tag{6.29}$$

For coarsely packed sandstone, limestone, and rocks, the relative permeability is given by Wyllie [55] as,

$K_{rl} = s^4$

$$K_{rg} = (1-s)^2(1-s^2) \tag{6.30}$$

and the permeability for trickling flow in packed bed is given by Levec et al.[56],

$K_{rl} = s^2$

$$K_{rg} = (1-s)^n,\ n = 4.8. \tag{6.31}$$

Where, s is the state of saturation, or liquid “hold uwhich is the fraction of the average pore volume occupied by the wet phase and is expressed by

$$s = \frac{\varepsilon_l}{\varepsilon} \tag{6.32}$$

K_{li} and K_{gi} are inertial coefficient to be determined in the inertial regime. According to existing models, these inertial coefficients are defined as

$$\frac{\rho_l}{K_{li}}\left|\langle u_{lj}\rangle\right|\langle u_{lj}\rangle = \rho_l \frac{f}{\sqrt{K}}\frac{1}{K_{rli}}\left|\langle u_{lj}\rangle\right|\langle u_{lj}\rangle \tag{6.33}$$

$$\frac{\rho_g}{K_{gi}}\left|\langle u_{gj}\rangle\right|\langle u_{gj}\rangle = \rho_g \frac{f}{\sqrt{K}}\frac{1}{K_{rgi}}\left|\langle u_{gj}\rangle\right|\langle u_{gj}\rangle \tag{6.34}$$

where K_{rli} and K_{rgi} are the relative inertial permeabilities. The inertial regime is not encountered for large pore sizes; this effect is important only in relatively coarse packed beds and high porosity matrices. And the empirically obtained permeabilities are generally assumed to be a function of saturation. Further simplification is possible by assuming $K_{rli} = K_{rl}$ and $K_{rgi} = K_{rg}$ for Darcian flow regime, but this is not expected for the coarse porous beds. The currently available correlations in the literature for relative inertial permeability are for co-current trickle flow in packed beds and given by Saez and Carbonell [57], as

$$K_{rgi} = K_{rg}\,,\ K_{rli} = K_{rl} \tag{6.35}$$

For packed beds made of large particles, the permeabilities are given by Schulenberg and Muller [58], as

$$K_{rli} = s^5\,,\ 0 \le s \le 0.7$$

$$K_{rgi} = (1-s)^6\,,\ 0 \le s \le 0.7$$

$$K_{rgi} = 0.1(1-s)^4\,,\ 0.7 \le s \le 1 \tag{6.36}$$

In case of large pore size, the capillary effect will be confined to a very small fraction of the pore volume and can be neglected.

Currently, no direct simulation of two-phase flow in porous foam is available [53]. The empirical correlations for prediction of pressure drop have been developed by several researchers. One of those equations is

$$\log\left(\frac{\Delta p_t / L}{\Delta p_l / L + \Delta p_g / L}\right) = \frac{0.416}{(\log\chi)^2 + 0.666}\,,\ \text{where, } \chi = \left(\frac{\Delta p_l}{L} \Big/ \frac{\Delta p_g}{L}\right)^{0.5} \tag{6.37}$$

by Larkins and White [59]. This correlation is for the flow of air and water over 9.5 mm spheres, natural gas-Kerosene flow over 3 mm spheres within a 10.16 cm pipe and CO_2-Lube oil flowing over 3 mm spheres within a 5.8 cm pipe. In this study the porosity was from 0.362 to 0.52 and the Reynolds number, based on gas superficial velocity and particle diameter, varied from 5 ~ 5,000.

Another pressure drop correlation, Equation (6.38), was developed by Saada [60].

$$\frac{\Delta p_t}{L} = 0.027 g \rho_l \operatorname{Re}_l^{0.35} \operatorname{Re}_g^{0.51} \left(\frac{d_c}{d_s} \right)^{1.15} \tag{6.38}$$

where, d_s is pipe diameter and d_s is particle diameter. His experiment was performed with air-water flowing over glass spheres 0.5 ~ 2 mm in dimater with a porosity of around 0.346. The range of Reynolds number based on the liquid superficial velocity and particle diameter was 5 to 1000.

Jamialahmadi and Izadpanah [61] performed their experiment with air-water and 0.3 ~ 3 mm glass spheres with a porosity of 36% ~ 38%. They compared their experimental results for 1mm diameter spheres with the above correlation. They applied a modified Reynolds number $\left(\operatorname{Re}_{m,l} = \rho u d_p / \mu(1-\varepsilon)\right)$ in order to compensate for different levels of porosity. The error between the experimental result of Jamialahmadi and Izadnanah and predicted result by those correlations is more than 30% and the difference between results predicted by Eq. (6.37) and Eq. (6.38) is more than 100%. Consequently, Jamialahmadi and Izadnanah [61] suggested their own correlation,Eq. (6.39), based on their experimental results [61]. The result is shown in Figure 6.13. The 20% error bar is drawn and it confirmed that most of the data is within the 20% error.

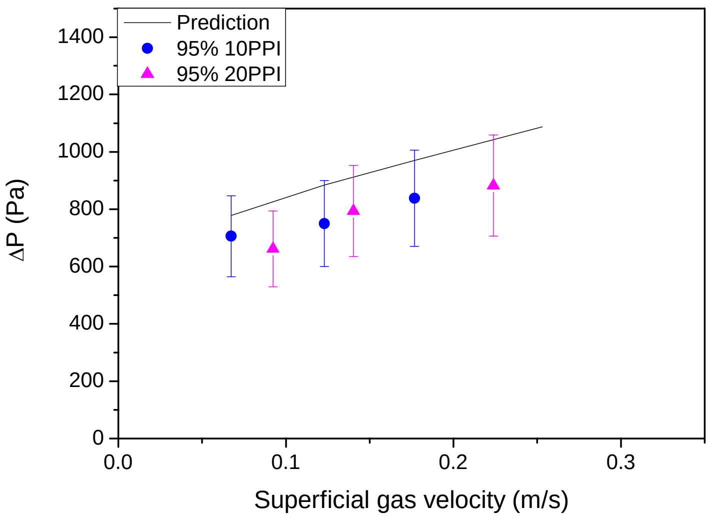

(a)

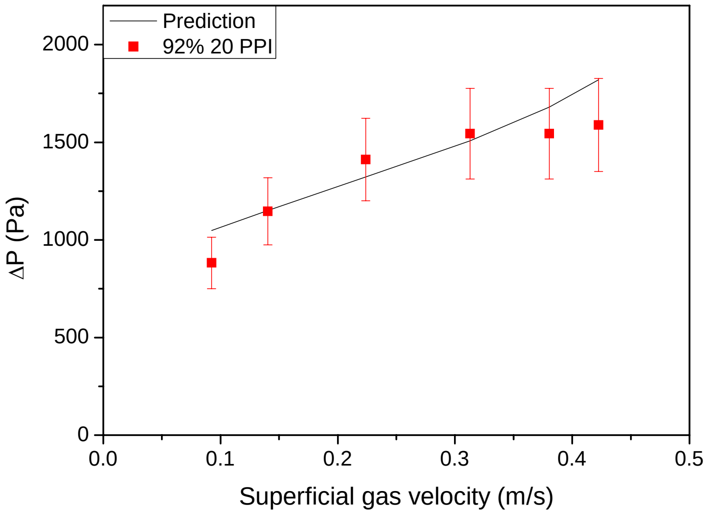

(b)

Figure 6.13 Two-phase pressure drop measurement result (a) comparison of 95% porosity with Eq. (6.40) and (b) comparison of 92% porosity with Eq. (6.40)

$$\frac{\Delta p_t}{L} = \frac{f_t}{2} \cdot \frac{4}{\varepsilon^2 d_p} \rho_g u_{sg}^2 \text{, where } \frac{f_t}{2} = 94 \frac{\mathrm{Re}_l^{1.11}}{\mathrm{Re}_g^{1.8}} + 4.4 \qquad (6.39)$$

The comparison of Eq. (6.39) and our experimental results displays a discrepancy of more than 30%. The reason for the discrepancy may be that Eq. (6.39) was developed from low porosity experiments. Therefore, we did a parametric study and found that the best fit between this relation and our experimental data was achieved with an exponent of liquid Reynolds number at 1.0, yielding a revised expression for the friction factor, as

$$\frac{f_t}{2} = 94 \frac{\mathrm{Re}_l^{1.0}}{\mathrm{Re}_g^{1.8}} + 3 \qquad (6.40)$$

6.3.2 Flow Regime Maps

Much of the two-phase flow analysis which is shown in this study is based on the low porosity packed beds. Many attempts have been made to identify the flow regimes when gas and liquid flow concurrently through such porous media, e.g. porosity of 40 to 60% and spheres of various diameters from 0.5 mm to 2 mm. Due to the difference in the hydrodynamic characteristics of different regimes, the respective heat and mass transfer rate, pressure drop, liquid “hold up” also differ in a significant way. For the down flow of air-water mixtures in a porous media, NG’s flow regime map [62] has gained general acceptance, but for upflow in such media, different flow regime maps have been obtainded by different researchers. There is also no reported flow regime map for horizontal flow.

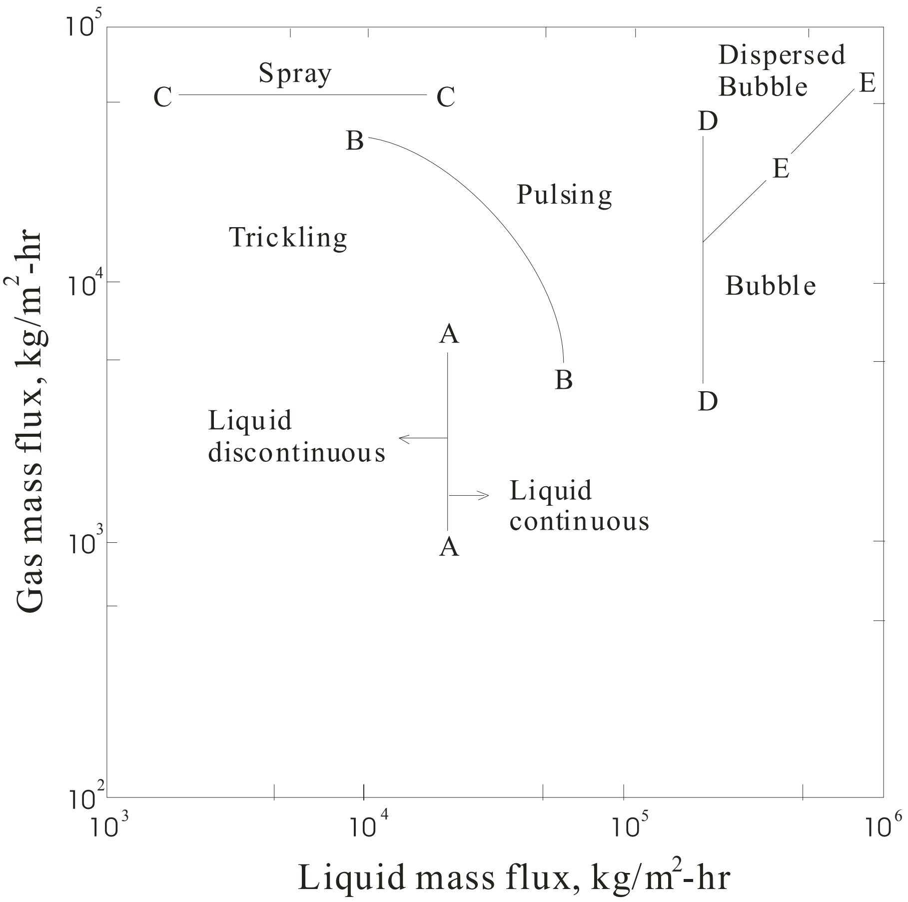

Figure 6.14 Flow regime map of the down flow of air-water mixtures in a porous media [62]

6.3.3 Experimental Results

Figure 6.15 shows the two-phase experimental results of metal foam of 95% porosity and 10 PPI which was solder to the copper base block at various mass flux. The experiment was done twice under the same conditions and the average deviation between the experiments is less than 7%. The increase of mass flux from 20 kg/m^2-s to 48 kg/m^2-s enhanced the heat transfer rate. The enhancement of highest heat transfer coefficient was 15%. Further increasing the mass flux, up to 72 kg/m^2-s, did not enhance the cooling capability due to the subcooled condition.

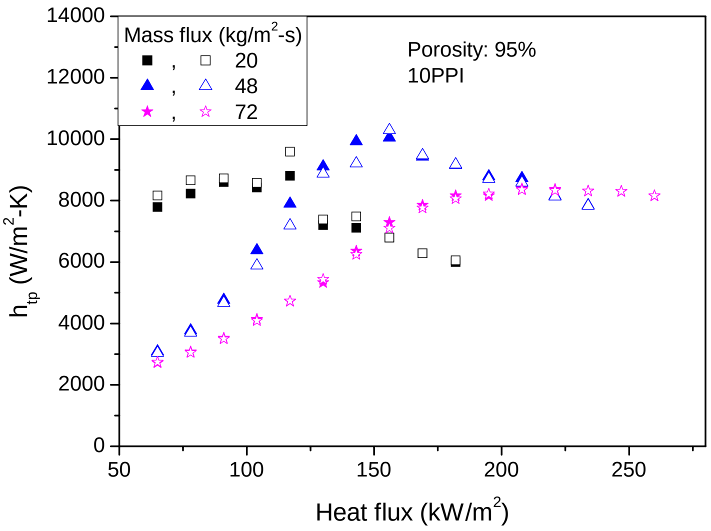

Figure 6.15 Mass flux effect on the two-phase heat transfer coefficient of 95% porosity and 10PPI foam

Figure 6.16 shows the two-phase experimental results for heat transfer to metal foam of 95% porosity and 20 PPI. Increasing of mass flux from 20 kg/m^2-s to 48 kg/m^2-s enhanced the heat transfer rate. The highest heat transfer coefficient was enhanced 10% by the increasing of mass flux. The repeatability which could be defined as the deviation of two different experiments is less than 5%. The heat transfer coefficient increased as the heat flux increased, due to the flow condition transitioning from subcooled to saturated flow boiling. Further increasing of the mass flux from 48 kg/m^2-s to 72 kg/m^2-s could not increase the cooling capability due to the subcooled condition.

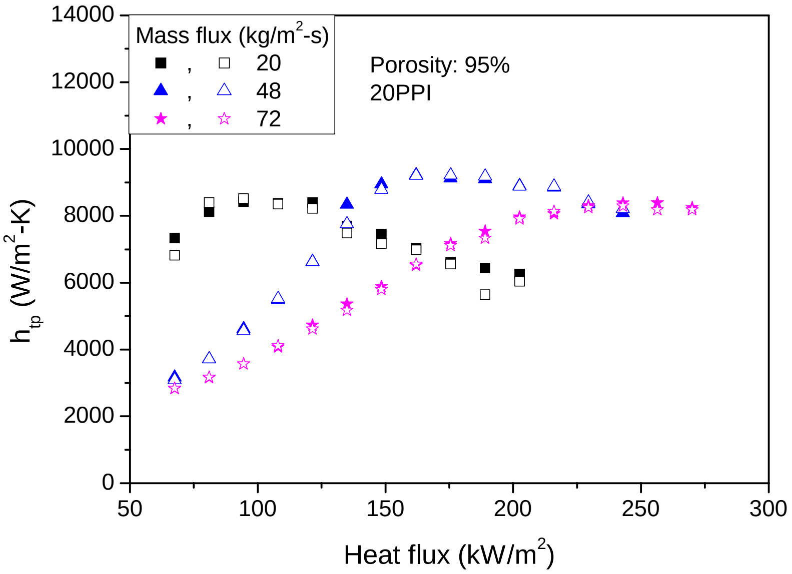

Figure 6.16 Mass flux effect on the two-phase heat transfer rate of 95% porosity and 20 PPI foam

Figure 6.17 shows the two-phase experimental results for the metal foam of 92% porosity and 20 PPI. The two-phase heat transfer coefficient variation of this foam configuration is as the same form as for 95% porosity, 20 PPI foam. Increasing the mass flux from 20 kg/m^2-s to 48 kg/m^2-s shifted the highest heat transfer coefficient to the high heat flux and the decreasing of heat transfer coefficient is slow. The enhancement was not distinct compare to 95% porosity foams. A further increase of mass flux up to 72 kg/m^2-s dose not enhanced the heat transfer rate.

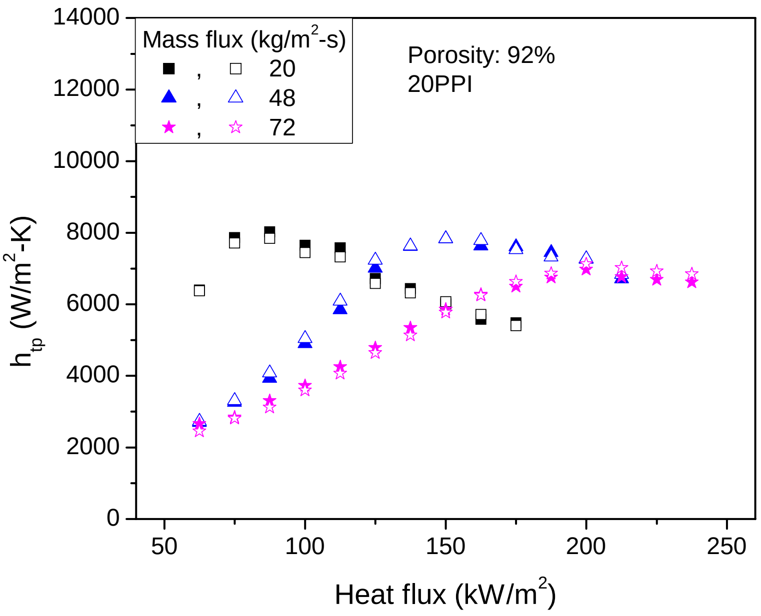

Figure 6.17 Mass flux effect on the two-phase heat transfer rate of 92% porosity and 20PPI foam

Figure 6.18 shows the effect of porosity and pore size (PPI) on the wall heat transfer rate at three distinct flow rates. As shown in Figure 6.18 (a), at mass flux of 20 kg/m^2-s, it is hard to see the difference between foams of different pore size (PPI) and porosity. It is noticed that from the subcooled to the early boiling region, low pore count (large pore size) is slightly better than the high PPI (smaller pore size). However, as the heat flux increases, the high pore count (smaller pore size) shows higher heat transfer coefficient. The difference of heat transfer coefficient between 10 PPI and 20 PPI at 95% porosity is less than 10% which is within the experimental error. The foam of 92% porosity and 20 PPI shows a lower heat transfer rate, 20% lower than that of 95% porosity foam.

Figure 6.18 (b) shows the experimental results for of a mass flux of 48 kg/m^2-s. The thermal performance of the 95% porosity, 10 PPI foam is 10% higher than 95% porosity, 20 PPI foam. The lower porosity foam, 92% porosity and 20 PPI foam, is 20% lower than 95% porosity foam. This could be due to the low thermal conductivity of the sintered-metal foam, due to the presence of hollow ligaments.

A similar result is seen in Figure 6.18 (c), where there is nearly no distinction between the thermal performance of the 92% and 95% foams at low heat flux, but up to a 23% lower thermal transport capability for the 92% porosity and 20 PPI material at the highest heat fluxes tested. Interestingly, Figure 6.18 (c) reveals 95% porosity and 10 PPI foam, shows highest thermal transport capability at same test condition.

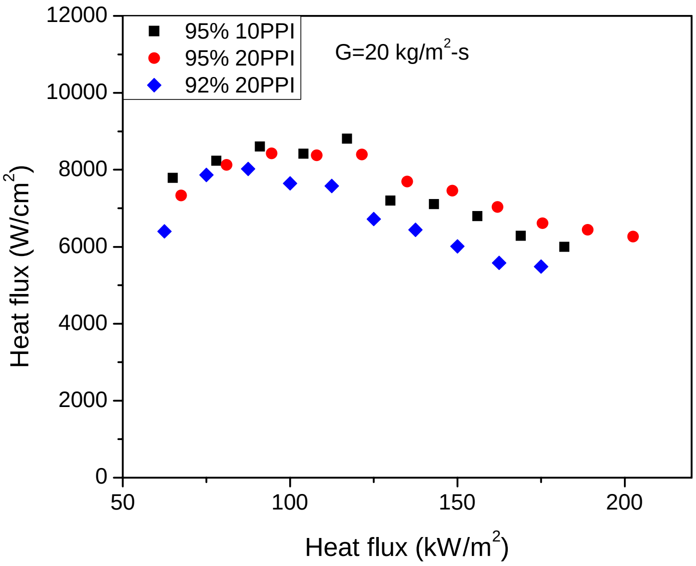

(a)

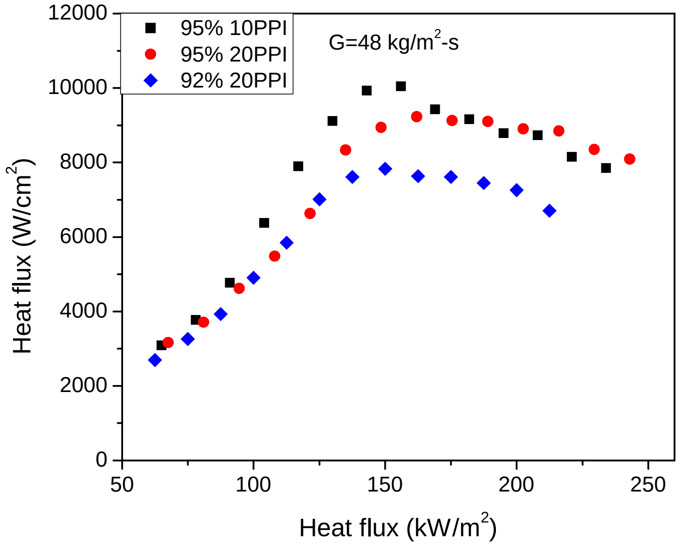

(b)

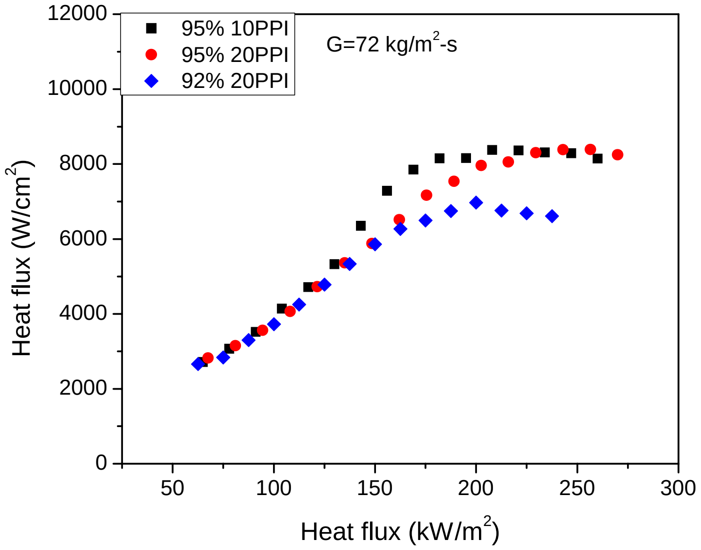

(c)

Figure 6.18 Porosity and pore size effect on the two-phase heat transfer rate at same mass flux (a) Experimental result of 20 kg/m^2-s of mass flux, (b) Experimental result of 48 kg/m^2-s of mass flux and (c) Experimental result of 72 kg/m^2-s of mass flux

From the results, it can be concluded that – for horizontal two-phase flow and within the parametric range studied – the foam porosity can have a modest effect, up to 23%, on the heat transfer coefficient at high heat fluxes. Alternatively, if the porosity is the same, the large pore size has better capability on heat transfer. It might be argued that the reason the high porosity foams do better at high fluxes is that there is more vapor that needs to flow through the foam (i.e. higher quality) and that it is the porosity and large pore size – that determines how easy it is for the vapor to escape from the wall area.

6.4 Conclusion

In the analysis of the characteristic of the porous foam channel in the single phase and two phase heat transfer, a heat transfer coefficient of 10 kW/m^2-K was achieved with 95% porosity and 20 PPI with water and a heat transfer coefficient of 2.85 kW/m^2-K was achieved at the same configuration of foam with FC-72 for the single phase. As expected, the porous foam provides higher heat transfer rate than the open channel and FC-72's heat transfer capability was 35% of water, which was 10% greater than the single gap channel. Due to the enhancement of dispersion effect, smaller pore size (high PPI) at the same porosity foam could provide higher heat transfer rate, it was hard to observe because the enhancement is in the range of experimental error. The dispersion coefficient of FC-72 was suggested between 0.03 and 0.06 based on the data fitting of the experimental results. Even though the porous foam channel provides high heat transfer rate, the pressure drop was also greater than open channel. The result of the two-phase heat transfer capability of the different configuration of foam was compared. The large pore size has better capability on two-phase heat transfer rate.

Chapter 7

Conclusion and Future Work

7.1 Conclusion

This study addresses the thermal and fluid characteristic of a liquid cooled single gap channel and a metal foam-filled channel for the cooling of high heat flux electronic and photonic devices. In anticipation that such cooling channels will provide direct liquid cooling of electronic and photonic devices, such as arrays of LED's, much of the effort is focused on the characteristics of a dielectric liquid, FC-72. To verify the capability and the accuracy of the experimental apparatus, water is used as a working fluid, because of the well known physical properties and available data for comparison. The conclusions of each chapter are provided as follows.

Conclusions of each chapter:

In chapter 1 and chapter 2:

- The motivation of this study and thermally-related problems of LEDs, such as life time and degradation of optical output due to temperature, were presented.
- The thermal resistance network was analyzed and the controlling thermal resistance was identified.
- Use of a single, liquid-cooled micro gap channel, which can eliminate the need for a thermal interface material (TIM) between heat source and the coolant, was proposed and shown to offer dramatic improvement in cooling capability.

Chapter 3 describes the experimental apparatus and operating procedure used in obtaining the thermo-fluid characteristics of the single micro gap channel.

Chapter 4 provides the:

- Theoretical background for the pressure drop and heat transfer characteristic of a single micro gap channel and preliminary experiment results using a 31 mm wide by 34 mm long channel with gaps of 600 µm, 260 µm and 120 µm, respectively.
- Experimental pressure drop data for three different micro e gaps: 600 µm, 260 µm and 120 µm and comparison with the best available correlation. The deviation of the measured results from the correlation was found to be less than 7%.
- Use of the measured single phase pressure drop to precisely determine the microgap dimension.
- Validation of the experiment results and the experimental apparatus based on comparison of the experiment results of water with the correlation.
- Observation of the dissolved gas effect, creating pseudo-boiling in single-phase convective heat transfer of FC-72, which can explain the discrepancy between the correlation and FC-72 experimental data. Use of an inverse numerical computation to determine the local wall heat flux variation along the microgap channel
- Application of flow regime mapping to determine the prevailing two-phase flow regimes and relevant correlations for flow boiling in microgap channels

- Novel use of IR Thermography to capture the temperature distribution and investigate the heal transfer characteristic of the wetted microgap channel wall

Chapter 5 provides:

- Single-phase data for water and FC-72 and two-phase thermo-fluid data for FC-72 flowing in three different single micro gap channels, 10 mm wide by 37 mm long, with gap heights of 210 μm, 23 kW/m^2-K of heat transfer coefficient for water and with gap heights of 110 μm, 5 kW/m^2-K of heat transfer coefficient for water were obtained.
- Confirmation that smaller gap channels provide better heat transfer capability in single phase flow, yielding 85% enhancement of heat transfer coefficients from 500 μm to 210 μm for water and 70% enhancement from 500 μm to 210 μm for FC-72. Further decreasing of gap from 210 μm to 110 μm enhances 25% more for FC-72.
- Observation that in the parametric range tested, the smaller gap channels provide better heat transfer capability in two-phase flow, yielding heat transfer coefficients as high as 10 kW/m2-K for FC-72 flowing in a 110 μm channel.
- Verification that, in the parametric range tested, Shah's correlation is appropriate for predicting heat transfer coefficients in the Intermittent flow regime and Chen's correlation is appropriate for the prediction of heat transfer coefficients in Annular flow regime.

Chapter 6 provides:

- Experimental thermo-fluid data for pressure drop and heat transfer of 92% porosity and 20 PPI copper foam and 95% porosity with 10 and 20 PPI Nickel plated copper foam were explored in the dimension of 10 mm x 37 mm long and 7 mm height channel.

- Observation that porous foam-filled channels can provide single phase heat transfer coefficients as high as 10 kW/m^2-K and 2.85 kW/m^2-K for water an FC-72 respectively at the 95% porosity and 20 PPI configuration foam.
- Confirmation that the use of the porous foam can enhance the single-phase thermal performance of low conductivity FC-72, with the dielectric liquid reaching 35% of the water heat transfer coefficients 10% higher than achieved in the open microgap channel tests.
- Observation that porous foam-filled channels can provide two-phase heat transfer coefficients as high as 10 kW/m^2-K for FC-72 flowing in 10 mm x 37 mm long and 7 mm height at mass flux of 48 kg/m^2-s and 95% porosity and 10 PPI foam configuration.
- Observation that when the porous foam is not manufactured by a common process, it is difficult to detect a consistent dependence of the heat transfer coefficients on the pore size and porosity. Comparison between foam-filled and open microgap heat transfer coefficients that reveals the micro gap single channel to provide better heat transfer capability, especially when considering the volume of the channel gap.

7.2 Future Work

In this dissertation extensive effort was devoted to the determination of the single phase and two phase thermofluid characteristics of single micro gap channels and porous metal foam-filled channels, with water and FC-72 as the working fluids. To complete the understanding of these phenomena future investigations related this study are suggested as follows.

7.2.1 Single micro gap channel

- The single-phase heat transfer coefficient results of FC-72 did not agree with theory as well as water. It was suggested that the discrepancy could be due to the dissolved gas in FC-72. It is necessary to perform single-phase convection experiments with degassed FC-72 to verify this contention.
- Due to the limitations of the experimental apparatus, nearly all of the two-phase flow experiments were performed with subcooled inlet condition. To better establish the interpretation and evaluation of the data, saturated inlet conditions should be maintained through re-design of the apparatus for more deliberate control of the inlet temperature.
- A wider range of heat flux and flow rates should be imposed on the test microgap channel to substantiate and more broadly establish the conclusions drawn on the two-phase behavior along the wetted surface.
- The IR images captured along the channel wall served to establish that significant temperature variations – in time and in space – accompany two-phase flow in the microgap channel. Inverse analysis, combining - transient heat conduction computations with IR thermography, could be used to determine the locally varying (with time and position) the flow boiling heat transfer coefficients in the microgap channel.

7.2.2 Porous foam channel

- To more firmly establish the preliminary trends observed in this study requires a broader range of parametric variations in the geometry of the porous metal foam.
- Moreover, to increase the credibility of the suggested conclusions, use should be made of an identical manufacturing process and pore geometry in the formation of the various foam configurations selected for experimentations.
- As well in the single microgap channel, foam-filled experiments with the flow of degassed FC-72 would be helpful in figuring out the dissolved gas effect of FC-72.
- To complete the two-phase flow heat transfer characterization of foam-filled channels, more extensive numerical and analytical modeling work is needed.

Reference

[1] Steranka, F. M. et al., "High Power LEDs – Technology Status and Market Applications", Phys. Stat. sol. (a), V. 194 No. 2, 2002, pp. 380-388

[2] Schubert, Fred E., "Light Emitting Diode", Cambridge University Press, 2003

[3] Keuper, M., Harbers, G., Paolini, S., "RGB LED Illuminator for Pocket-Sized Projectors", SID Digest, 2004

[4] Harbers, G., Keuper, M., Paolini, S., "Performance of High Power LED Illuminators in Color Sequential Projection displays", IDW 2003

[5] Wall, F., "High Power LED Package Requirements", Proceedings of SPIE, V.5187, 2003, pp. 85-92.

[6] Treurniet, T., Lammens, V., "Thermal Management in Color Variable Multi-Chip LED Modules", 22nd IEEE SEMI-THERM Symposium, 2006

[7] http://www.lumileds.com/pdfs/RD25.PDF

[8] Jacob, S., "Maximizing Useful SSL Lifetime", Proceedings of SPIE, V.5187, 2003, pp. 76-84.

[9] Lumileds Application Brief AB05, 2007, Luxeon Reliability

[10] Park, J. S., Bok, K. S., Lee, S. G., "Numerical Analysis of Heat Transfer from an LED Die in Duty Operation", 13th International Heat Transfer Conference, 2006, CND-10.

[11] Lee, P., Garimella, S., Liu, D., "Investigation of heat transfer in rectangular microchannel", International Journal of Heat and Mass Transfer, v.48 2005, pp. 1688-1704

[12] Kang, S., Yang, L., Yu, C., Chen, J., "The performance test and Analysis of Silicon based Microchannel Heat Sink". SPIE v.3795, 1999, pp. 259-270

[13] Lee, J., Mudawar, I., "Two-phase Flow in High Heat Flux Microchannel Heat sink for Refrigeration Cooling Applications: part II-Heat Transfer Characteristics", IJHMT, V.48, 2005, pp. 941-955

[14] Steinke, M.E., Kandlikar, Satish G., "An Experimental Investigation of Flow Boiling Characteristics of Water in Parallel Microchannels", Transactions of the ASME, v.126, 2004

[15] http://www.lumileds.com/pdfs/AB29.pdf

[16] Li, K. and Inatsugu, S., "Etendue Efficient Coupling of an Array of LEDs for Projection Display", Proceedings of SPIE, V.5740, 2005, pp. 36-40.

[17] Wilcoxon, R. and Cornelius, D., "Thermal Management of an LED Light Engine for Airborne Applications", 22nd IEEE SEMI-THERM Symposium, 2006, pp. 178-185.

[18] Haque, S. et al., "Packaging Challenges of High-Power LEDs for Solid State Lighting", International Symposium on Microelectronics, 2003, pp. 881-886.

[19] Mirmira, S. R. and Fletcher, L. S., "Effective Thermal Conductivity of Epoxy Adhesives for Microelectronics Application", American Institute of Aeronautics & Astronautics", 1999

[20] Figliola, R., Beasley, D., "Theory and Design for Mechanical Measurements", John Wiley & Sons, Inc., 1995.

[21] Kays, W. M., and London, A. L., "Compact Heat Exchangers", McGraw-Hill, New York, 1984

[22] Shah, R. K. and London, A.L., 1978, “Laminar Flow Forced Convection in Ducts”, Supplement 1 to Advances in Heat Transfer, Academics, New York

[23] Kays, W. M. and Crawford, C., 1966, “Convective Heat and Mass Transfer”, Mcgraw-Hill, New York

[24] Mercer, W., Pearce, W. M., Hitchcock, J.E., 1967, “Laminar Forced Convection in the Entrance Region Between Parallel Flat Plates”, J. Of Heat Transfer, pp. 251-257

[25] Xie, Y. Q., Yu, J. Z. And Zhao, Z. H., 2005, “Experimental Investigation of Flow and Heat Transfre for the Ethanol-Water Solution and FC-72 in Rectangular Microchannel”, Heat Mass Transfer, 41, pp. 695-702

[26] http://multimedia.mmm.com/mws/mediawebserver.dyn

[27] Chen, T., Garimella, S., 2006, “Effects of Dissolved Air on Subcooled Flow Boiling of a Dielectric Coolant in a Microchannel Heat Sink”, Transactions of the ASME, V.128, pp.398-404

[28] Lee, H. J., Lee, S. Y., 2001, “Heat Transfer Correlation for Boiling Flow in Small Rectangular Horizontal Channels with Low Aspect Ratio”, Int. J. Multiphase Flow, V.27, pp. 2043-2062

[29] Yang, Y., Fujita, Y., 2004, “Flow Boiling Heat Transfer and Flow Pattern in Rectangular Channel of Mini-gap”, Second International Conference on Microchannels and Minichannels (ICMM2004-2383), New York, USA

[30] Kuznetsov, V. V., Shamirzaev, A.S., 2006, “Boiling Heat Transfer for Freon R21 in Rectangular Minichannel”, Fourth International Conference on Microchannels and Minichannels (ICNMM2006-96096), Limerick, Ireland

[31] Taitel, Y. and Dukler, A. E., 1976, “A Model for Prediction of Flow Regime Transitions in Horizontal and Near Horizontal Gas-liquid Flow”, AIChE J., V.22, pp.47-55.

[32] Kim, D. W., Rahim, E. and Bar-Cohen, A, “Thermofluid Characteristics of Two-Phase Microgap Coolers” The ASME 2007 InterPACK Conference

[33] Chen, J. C., 1967, “Correlation for Boiling Heat Transfer to Saturated Fluids in Convective Flow”, Industrial and Engineering Chemistry, Process Design and Development, V.5, No.3, pp.322-329

[34] Collier, J. G., “Forced Convective Boiling in Two-Phase Flow and Heat Transfer in the Power and Process Industries”, Hemisphere, New York, 1981.

[35] Shah, M. M., 1976, “A New Correlation for Heat Transfer during Boiling Flow through Pipes”, ASHRAE Transactions, Vol. 82 part 2, pp.66-86

[36] Shah, M. M., 1982, “Chart Correlation for Saturated Boiling Heat Transfer: Equations and Further Study.”, *ASHRAE Transactions*, v 88, n pt 1, 1982, p 185-196

[37] Bar-Cohen, A., Sher, I., Rahim, E., “On the Application of Macro-pipe Two-phase Heat Transfer Correlations and Flow Regime Maps to Mini-channels,” Proceedings of ASME Fourth International Conference on Nanochannels, Microchannels and Minichannels, Ireland, 2006.

[38] Hetsroni, G., Mosyak A., Segal, Z. and Ziskind,G., 2002, “A uniform Temperature Heat sink for Cooling of Electronic Devices”, International J. of Heat and Mass Transfer, 45, pp.3275-3286

[39] Diaz, M. Cortina, Schmidt, J., 2006, “Flow Boiling Heat Transfer of n-Hexane and n-Octane in a Minichannel” Thirteenth International Heat Transfer Conference, Sydney, Australia

[40] Boomsma, K., Poulikakos, D., Zwick, F., “Metal foams as compact high performance heat exchangers”, Mechanics of Materials V.35, 2003, pp. 1161–1176

[41] Calmidi, V. V., Mahajan, R. L., “Forced Convection in High porosity Metal Foams”, J of Heat Transfer, V.122, 2000, pp. 557-565

[42] Calmidi, V. V., “Transport Phenomena in High Porosity Metal Foams”, Ph. D. thesis, U of Colorado, 1998

[43] Bhattacharya, A., Calmidi, V. V., Mahajan, R. L., “Thermophysical Properties of High Porosity Metal Foams”, IJ of Heat and Mass Transfer, V.45, 2002, pp. 1017-1031

[44] Fouriea, J. G., DuPlessis, J. P., “Pressure Drop Modeling in Cellular Metallic Foams”, Chemical Eng. Science V. 57, 2002 pp. 2781 – 2789

[45] Alazmi, B., Vafai, K., “Analysis of Variable Porosity, Thermal Dispersion, and Local Thermal Nonequilibrium on Free Surface Flows Through Porous Media”, Journal of Heat Transfer**,** 2004, V.126, pp. 389-399.

[46] Poulikakos, D., Renken, K., “Forced Convection in a Channel Filled with Porous Medium, Including the Effects of Flow Inertia, Variable Porosity and Brinkman Friction”, Trans. of the ASME, V. 109, 1987, pp. 880-888

[47] Prieur Du Plessis, “Pressure Drop Prediction for Flow through High Porosity Metallic Foams”, Vhem. Eng. Sci. V.49, 1994, pp. 3545-3553

[48] Ashby, M. F., et al., “Metal Foams: A Design Guide”, J.W. Hutchinson and H.N.G. Wadley, 2000.

[49] www.thrive-metal.com

[50] www.porvair.com

[51] Hunt, M. L., Tien, C.L., “Effects of Thermal Dispersion on Forced Convection in Fibrous Media”, Int. J. of Heat Mass Transfer, V.31, n.2, 1988, pp. 301-309

[52] D. Poulikakos, K. Renken, “Forced Convection in a channel Filled with Porous Medium, Including the Effects of Flow Inertia, Variable Porosity and Brinkman Friction”, Trans. Of the ASME, V. 109, 1987, pp. 880-888

[53] Kaviany, “Principles of Heat Transfer in Porous Media”, Springer, 1995

[54] Verma., A. K., Pruess, K., Tsang, C. F., and Withespoon, P. A., “A Study of Two-Phase Concurrent Flow of Steam and Water in an Unconsolidated Porous Medium”, Heat Transfer in Porous Media and Particulate Flows, ASME HTD, v. 46, 1984, pp.135-143

[55] Wyllie, M. R. J., “Relative Permeabilities”, in Petroleum Production Handbook, McGraw-Hill, 1962, v. 2, Chapter 25, pp. 1-14

[56] Levec, J., Saez, A. E., and Carbonell, R. G., “The Hydrodynamics of Trickling Flow in Packed Beds, Part II: Experimental Observations”, AIChE J, 1986, v. 32, pp. 369-380

[57] Saez, A. E., and Carbonell, R. G., “Hydrodynamics Parameters for Gas-Liquid Co-current Flows in Packed Beds”, AIChE J., 1985, v. 31, pp. 52-62

[58] Schulenburg, T., Muller, U., “An Improved Model for Two-Phase Flow through Beds of Coarse Particles”, Int. J. Multiphase Flow, 1987, v. 13, pp. 87-97

[59] Larkins. R., White, R., "Two-Phase Co-Current Flow in Packed Beds", AIChE. J. V.7, 1961, pp. 231-239

[60] M. Saada, "Fluid Mechanics of Co-Current Two-Phase Flow in Packed Beds: Pressure Drop and Liquid Hold-up Studies" Chem. Ind. Genie Chem. V.105, 1972, pp. 1415-1421

[61] M. Jamialahmadi, H. Muller-Steinhagen, M.R. Izadpanah, "Pressure Drop, Gas Hold-up and Heat Transfer during Single and Two-phase Flow through Porous Media", Int. J of Heat and Fluid Flow, V. 26, 2005, pp. 156–172

[62] K.M NG, "A Model for Flow Regime Transitions in Cocurrent Down-flow Trickel-bed Reactors", AlChE J. V. 32, n.1, 1986, pp. 115-122